STATISTICAL ESTIMATION OF TWO-BODY HYDRODYNAMIC PROPERTIES USING SYSTEM IDENTIFICATION

A Dissertation

by

CHEN XIE

Submitted to the Office of Graduate Studies of
Texas A&M University
in partial fulfillment of the requirements for the degree of

DOCTOR OF PHILOSOPHY

August 2009

Major Subject: Ocean Engineering

STATISTICAL ESTIMATION OF TWO-BODY HYDRODYNAMIC PROPERTIES USING SYSTEM IDENTIFICATION

A Dissertation

by

CHEN XIE

Submitted to the Office of Graduate Studies of
Texas A&M University
in partial fulfillment of the requirements for the degree of

DOCTOR OF PHILOSOPHY

Approved by:

Chair of Committee,	John M. Niedzwecki
Committee Members,	Billy Edge
	H. Joseph Newton
	Ken Reinschmidt
Head of Department,	David V. Rosowsky

August 2009

Major Subject: Ocean Engineering

ABSTRACT

Statistical Estimation of Two-Body Hydrodynamic Properties Using System Identification. (August 2009)

Chen Xie, B.S., Ecole Spéciale des Travaux Publics;

M.S., Ecole Spéciale des Travaux Publics;

M.S., Texas A&M University

Chair of Advisory Committee: Dr. John M. Niedzwecki

A basic understanding of the hydrodynamic response behavior of the two-body system is important for a wide variety of offshore operations. This is a complex problem and model tests can provide data that in turn can be used to retrieve key information concerning the response characteristics of such systems. The current study demonstrates that the analysis of these data using a combination of statistical tools and system identification techniques can efficiently recover the main hydrodynamic parameters useful in design.

The computation of the statistical parameters, spectral densities and coherence functions provides an overview of the general response behavior of the system. The statistical analysis also guides the selection of the nonlinear terms that will be used in the reverse multi-input / single-output (R-MI/SO) system identification method in this study. With appropriate linear and nonlinear terms included in the equation of motion, the R-MISO technique is able to estimate the main hydrodynamic parameters that characterize the offshore system. In the past, the R-MISO method was primarily applied to single body systems, while in the current study a ship moored to a fixed barge was investigated. The

formulation included frequency-dependant hydrodynamic parameters which were evaluated from the experimental measurements. Several issues specific to this extension were addressed including the computation load, the interpretation of the results and the validation of the model. Only the most important cross-coupling terms were chosen to be kept based on the estimation of their energy. It is shown that both the heading and the loading condition can influence system motion behavior and that the impact of the wave in the gap between the two vessels is important. The coherence was computed to verify goodness-of-fit of the model, the results were overall satisfying.

DEDICATION

For my family.

For my beloved grandmother.

ACKNOWLEDGMENTS

I would like to acknowledge the financial support from the Texas Advanced Technology Program (ATP-000512-0286-2003), the Texas Engineering Experiment Station and the R.P Gregory ’32 Chair endowment. The effort and time provided by the professors, the technicians as well as the students who have worked on the model testing at the OTRC for this project is gratefully acknowledged. A special thanks to Dr. Richard Mercier, director of the OTRC, for the information he provided on the model test setting and data. I would also like to thank Dr. Per Teigen from StatoilHydro and Dr. Arun Duggal from SOFEC Inc. for their technical support. And the discussion between my academic advisor, Dr. John. M. Niedzwecki, and Drs. J. Nicolas Newman and Chang Ho Lee from MIT on the WAMIT program has been insightful.

I would like to express my gratitude and thanks to my advisor, Dr. John M. Niedzwecki, for his guidance and advice during all these years, for both my M.S. and PhD programs. I would also like to thank my advisory committee members: Dr. Billy Edge, Dr. Joseph H. Newton and Dr. Ken Reinschmidt, for their input and guidance throughout this research project.

I wish also to thank my parents, all the members of my family, as well as my friends for their support and help.

TABLE OF CONTENTS

Page

ABSTRACT iii

DEDICATION v

ACKNOWLEDGMENTS vi

TABLE OF CONTENTS vii

LIST OF FIGURES ix

LIST OF TABLES xiii

1. INTRODUCTION 1

1.1. Two-body system hydrodynamic problems 2
1.2. Reverse Multi-Input/Single-Output (R-MISO) system identification method 5
1.3. Research objective 10

2. STATISTICAL ANALYSIS OF THE TWO BODY HYDRODYNAMICS 13

2.1. Presentation of the ship / barge system 13
2.2. Overall motion behavior 17
2.2. Mooring line and fender forces 20
2.3. Influence of the tank waves 29

3. IDENTIFICATION OF THE SYSTEM PARAMETERS OF THE SINGLE BARGE 33

3.1. Reverse Multi-Input / Single-Output (R-MISO) method 33
3.2. Equation of motion 35
3.3. System identification analysis and results 39
3.3.1 Methodology applied to the barge pitch 39
3.3.2 Results and discussion 43
3.3.3. Validation of the results 55

4. IDENTIFICATION OF THE SYSTEM PARAMETERS OF A COUPLED BARGE AND SHIP SYSTEM 58

Page

4.1 Equation of motion 58
4.1.1 General form of the equation of motion of a two body system 58
4.1.2 Cross-coupling terms 63
4.2 System identification analysis and results 70
4.2.1 Barge pitch in head seas 72
4.2.2 Ship roll in head seas 89
4.2.3 Ship heave in head and quartering seas 101

5. SUMMARY AND CONCLUSION 117

REFERENCES 121

APPENDIX A. CALCULATION OF THE ROTATIONS BASED ON THE DISPLACEMENT DATA 125

APPENDIX B. VALIDATION OF MATLAB PROGRAM 130

APPENDIX C. COMPUTATION OF LINEAR STIFFNESS COEFFICIENTS 136

APPENDIX D. FORCE DECOMPOSITION 145

VITA 160

LIST OF FIGURES

Page

Figure 2.1 Configuration of the side-by-side moored ship / barge system..... 15

Figure 2.2 Model ship / barge system in head seas configuration..... 16

Figure 2.3 Spectral densities of the in-line forces of the mooring lines connecting the ship and the barge for (a) 80% filled tanks in head seas; (b) 80% filled tanks in quartering seas; (c) 10% filled tanks in head seas; and (d) 10% filled tanks in quartering seas..... 23

Figure 2.4 Relative surge near maximum force of a mooring line in head seas, with 10% filled tanks..... 24

Figure 2.5 Cross-spectrum and coherence function between the surge motion and the mooring line forces in head seas, with 10% filled tanks..... 26

Figure 2.6 Cross-spectrum and coherence function between the surge motion and the fender forces in head seas, with 10% filled tanks 27

Figure 2.7 Cross-spectrum and coherence function between the roll motion and the fender forces in head seas, with 10% filled tanks 28

Figure 2.8 Distribution of the wave gages inside the aft tank of the model ship. 30

Figure 2.9 Motion response amplitude operators (RAO) of the (a) ship roll motion in 0° heading, (b) ship roll motion in -45° heading, and (c) ship pitch motion in -45° heading; in the case of 10% filled tanks..... 32

Figure 3.1 Spectral density of (a) the input pitch, (b) the output pitch moment. 44

Figure 3.2 Comparison between the actual probability density function and the ideal normally distributed function with the same mean and variance for (a) the pitch motion, (b) the pitch moment..... 45

Figure 3.3 Cumulative coherence functions. 46

Figure 3.4 Extraneous noise / output ratio..... 46

Figure 3.5 Partial coherence functions. 47

Page

Figure 3.6 (a) The difference $S_{11}S_{yy} - \left|S_{1y}\right|^2$, and (b) the ratio $\left|S_{1y}\right|^2 / S_{11}S_{yy}$, around 0.23 Hz where the coherence is low. 49

Figure 3.7 Magnitude and phase spectra of the transfer function A1..... 51

Figure 3.8 Fitting of the magnitude of A1 near the zero frequency. 51

Figure 3.9 Virtual mass coefficient $I_{yy} + a_{55}$ 53

Figure 3.10 Linear damping coefficient c_{55} 53

Figure 3.11 Magnitude and phase spectra of the transfer function A2..... 54

Figure 3.12 Nonlinear damping coefficient d_{55} 54

Figure 3.13 Comparison between the reconstituted barge pitch moment and the measured barge pitch moment. 57

Figure 4.1 Cross power density spectrum of the barge pitch / ship pitch pair. 64

Figure 4.2 (a) Cumulative coherence function with all the coefficients; (b) Cumulative coherence function with only the most important coefficients. 69

Figure 4.3 Partial coherence functions between the inputs and the output of the model..... 71

Figure 4.4 Auto-spectral densities of (a) the input barge pitch $\theta_B(t)$, and (b) the output barge pitch moment $M_y(t)$, 0° heading..... 76

Figure 4.5 Goodness-of-fit of the initial model, barge pitch case, 0° heading. 78

Figure 4.6 Goodness-of-fit of the final model, barge pitch case, 0° heading. 78

Figure 4.7 Partial coherence functions of the inputs, barge pitch case, 0° heading. 80

Figure 4.8 Magnitude and phase of the transfer function $A_1(f)$, barge pitch case, 0° heading. 82

Figure 4.9 Virtual mass coefficient $\left(I_{yy_B} + a_{5,5}\right)(f)$, barge pitch case, 0° heading..... 83

Figure 4.10 Linear damping coefficient $c_{5,5}(f)$, barge pitch case, 0° heading. 83

Page

Figure 4.11 Added mass coefficients of the cross coupling terms, barge pitch case, 0˚ heading. 85
Figure 4.12 Linear damping coefficients of the cross coupling terms, barge pitch case, 0˚ heading. 86
Figure 4.13 Nonlinear damping coefficient, barge pitch case, 0˚ heading. 87
Figure 4.14 Quadratic mooring line force coefficients, barge pitch case, 0˚ heading. ... 87
Figure 4.15 Comparison between the reconstituted barge pitch moment and the measured barge pitch moment, two body system. 88
Figure 4.16 Auto-spectral densities of (a) the input ship roll $\phi_S(t)$, and (b) the output ship roll moment $M_x(t)$, 0˚ heading. 91
Figure 4.17 Goodness-of-fit of the initial model, ship roll case, 0˚ heading. 92
Figure 4.18 Goodness-of-fit of the final model, ship roll case, 0˚ heading. 92
Figure 4.19 Partial coherence functions of the inputs, ship roll case, 0˚ heading. 93
Figure 4.20 Virtual mass coefficient $\left(I_{xx_S} + a_{10,10}\right)(f)$, ship roll case, 0˚ heading. 96
Figure 4.21 Linear damping coefficient $c_{10,10}(f)$, ship roll case, 0˚ heading. 96
Figure 4.22 Added mass and virtual mass coefficients of the cross coupling terms, ship roll case, 0˚ heading. 97
Figure 4.23 Linear damping coefficients of the cross coupling terms, ship roll case, 0˚ heading. 98
Figure 4.24 Nonlinear damping coefficient, ship roll case, 0˚ heading. 99
Figure 4.25 Quadratic fender force coefficients, ship roll case, 0˚ heading. 99
Figure 4.26 Quadratic mooring line force coefficients, ship roll case, 0˚ heading. 100
Figure 4.27 Auto-spectral densities of (a) the input ship heave $z_S(t)$, and (b) the output ship heave force $F_z(t)$, in head and quartering seas. 104
Figure 4.28 Goodness-of-fit of the initial model, ship heave case, in (a) 0˚ heading, (b) 45˚ heading, and (c) -45˚ heading. 105

Page

Figure 4.29 Goodness-of-fit of the final model, ship heave case, in (a) 0˚ heading, (b) 45˚ heading, and (c) -45˚ heading. 106
Figure 4.30 Partial coherence functions of the inputs, ship heave case, 0˚ heading. 107
Figure 4.31 Partial coherence functions of the inputs, ship heave case, 45˚ heading. .. 108
Figure 4.32 Partial coherence functions of the inputs, ship heave case, -45˚ heading. . 109
Figure 4.33 Added mass coefficient $a_{9,9}(f)$, ship heave case, head and quartering seas. 112
Figure 4.34 Linear damping coefficient $c_{9,9}(f)$, ship heave case, head and quartering seas. 112
Figure 4.35 Added mass coefficients of the cross coupling terms, ship heave case, head and quartering seas. 113
Figure 4.36 Linear damping coefficients of the cross coupling terms, ship heave case, head and quartering seas. 114
Figure 4.37 Nonlinear damping coefficient, ship heave case, head and quartering seas. 115
Figure 4.38 Nonlinear stiffness coefficient, ship heave case, head and quartering seas. 115
Figure 4.39 Quadratic mooring line force coefficients, ship heave case, head and quartering seas. 116

LIST OF TABLES

Page

Table 1.1 Summary of selected papers on side-by-side moored two-body system problem. 11

Table 1.2 Summary of selected papers on reverse multi-input / single-output system identification method. 12

Table 2.1 Positive polarities of the vessels motions, mooring line and fender forces.... 16

Table 2.2 Comparison between the standard deviations of the barge and ship rotation motions (unit: degree) 19

Table 2.3 Sample means (μ), standard deviations (σ), minima and maxima of the relative motions (units: meters for surge, sway, heave and degrees for roll, pitch and yaw) 19

Table 2.4 Sample means, standard deviations, minima and maxima of the mooring line and fender forces (unit: kN) 22

Table 4.1 Area under the cross power density spectrum (0^{th} moment) of different motion pairs..... 66

1. INTRODUCTION

Interest in two-body hydrodynamic problems is gaining increasing attention due to the frequent use of closely positioned floating platforms in a variety of offshore operations. Tandem offloading is a common and safe practice whereas side-by-side arrangement presents more challenges due to its complex hydrodynamic interaction. However this latter configuration is more desired for certain operations, the best example being the quickly expanding exploration of Liquid Natural Gas (LNG). The offloading operations from the LNG terminal to the LNG carrier are conditioned by the arm-length of LNG off-loading lines and are also somewhat constrained by the fragility of the transportation lines due to extreme low temperature of the transferred flow. The side-by-side configuration is more adapted in this situation for both design and economical purposes. The complexity of the motion behavior of such systems is influenced by interaction effects including diffraction, radiation and in particular the wave field between the platforms. The configuration of the two-body system, which includes the size and the shape of the structures, the separation distance between them, the heading condition, as well as the stiffness of the various mooring and docking connections, will be important factors that influence the response behavior of the vessels.

Like more basic single body systems, two-body systems are characterized by their hydrodynamic parameters. The knowledge of the values of these parameters is important for it allows for one to better design the system behavior thus reducing aspects of the response behavior. System identification is a proven method that can be used to extract information about the system parameters directly from recorded or simulated excitation and corresponding response time series.

This dissertation follows the style of *Journal of Offshore and Polar Engineering.*

In the current study, it is attempted to use system identification method, more precisely one called Reverse Multi-Input / Single-Output (R-MISO) method, to solve for two-body hydrodynamic problems. A review of both topics in open literature is developed in the following sections aiming to provide insight to the basis of this new approach. Tables 1 and 2 present a summary of some selected papers relevant to respectively the two body hydrodynamic problem and the R-MISO method. They illustrate the variety of existing applications and methodologies.

1.1. Two-body system hydrodynamic problems

For research addressing side-by-side moored two-body systems, a fair amount of studies have been dedicated to investigate the complex hydrodynamic behavior of such systems. Some of the most fundamental work in this field includes the study by Ohkusu (1976) who proposed a strip theory based method to evaluate the interaction forces for a multi-body system consisting of slender bodies. Van Oortemerssen (1981) was the first to apply the three dimensional source distribution method, a common form of the Boundary Integral Method (BIM), for motion analysis of two floating bodies with more arbitrary geometries. Subsequently Taylor and Zietsman (1982) introduced the use of Finite Element Method (FEM) in the field with the development of a combined method: FEM for fluid region near the bodies and BIM for the far field region.

Among the most recent reported studies, Huijsmans *et al*. (2001) investigated the hydrodynamic interaction effects in both the first order motions and the mean second order drift forces on a pair of closely positioned FPSO and LNG carrier. It was shown that the simplification of using free floating single body hydrodynamics to study the multi-body hydrodynamics is not feasible in side-by-side arrangement with small gap distance. A linear potential solver was used for the computation and the importance of

having sufficient number of panels and of applying a lid to circumvent the overestimation of the wave velocities was discussed.

Frequency-domain analysis using techniques such as linear potential theory based methods as mentioned above is fast and efficient, it is however impossible to derive cause-reaction chains of a multi-body system. Time domain analysis on the other hand can address this issue and account nonlinear effects although computationally cumbersome. In order to take advantage of both methods, Clauss and Jacobsen (2005) proposed a transformation method where the response amplitude operators from frequency domain were converted to impulse response functions by using Fourier transformation. The example of a crane semi-submersible / transport barge system was used for illustration. Besides the efficiency of the method, it was shown that a wave train containing a wave packet with resonance components can be more dangerous than a single high wave.

For simplicity, researchers may choose to neglect the cross-coupling terms in a two-body problem. However, Koo and Kim (2005) demonstrated the importance of these terms in side-by-side mooring configurations. They used a time-domain coupled dynamics analysis program to study the relative motions of two floating platforms. More precisely an exact method called Combined Matrix Method (CMM) was adopted where all vessel and line dynamics as well as the hydrodynamic coefficients were included in a combined matrix. The results were found to be much more accurate compared with those obtained using two typical approximation methods not taking into account the diagonal terms: the Separate Matrix Method (SMM) and the No-Hydrodynamic Interaction Method (NHI).

The wave field near a two-body system were investigated by Teigen and Niedzwecki (2006). The wave loads and wave interaction effects on a side-by-side moored twin barge system were computed using both first and second order hydrodynamic theories. Extensions to the standard industrial software WAMIT allow one to address the

dominant viscous behavior presented in this configuration (Niedzwecki, 2007). It was observed that large wave amplification can occur in the gap between the two vessels for short periodic waves and that second order wave effects may result in important wave amplification at the trailing end of the vessels. Note that WAMIT, a panel method based code, is used in many studies for the numerical simulation of wave load and offshore structure motions. In experimental studies, it provides a good reference for comparison.

Due to the increasing number of LNG offloading operations, the effects of tank sloshing on the vessel motions became a topic to explore. In a study performed by Lee and Kim (2008), the dynamic coupling between the floating-body motions and the inner-tank sloshing was investigated in time domain. The coupling of the tank sloshing program and the vessel motion program during the time marching ensured the possibility to assess the influence of the tank sloshing on vessel motions. It was found that the vessel motions can be significantly increased if the wave frequency peak is close to the sloshing natural frequency and that the tank liquid motion and the vessel motion can be intensified due to multi-body interaction.

Along with numerical methods, experimental studies have played an important role in validating and refining the numerical scheme. When Buchner *et al.* (2001) was developing a numerical time domain simulation model for the prediction of the hydrodynamic response of a moored LNG FPSO and LNG carrier system, results of dedicated model tests were used to validate and extend the model. The comparison between simulation results and model testing data lead to several additional implementations aimed to improve the existing model. The application of a free surface lid in the diffraction analysis and the inclusion of viscous damping improved respectively the prediction of drift forces and low frequency motion response. And it was demonstrated that the use of the complete matrix of retardation functions in time domain is essential for the correct prediction of the main motions and mooring behavior.

Van der Valk and Watson (2005) studied experimentally the motion behavior of LNG vessels in both side-by-side and tandem mooring configurations. Tests were performed under different directional sea states and the results provide useful insight into the relative motions and the connection line forces. Combined with the operational limits unique to LNG vessels, the analysis result showed the pros and cons of both configurations.

Fournier *et al*. (2006) performed a calibration study by comparing the experimental results with simulation results provided by commercial diffraction packages, namely WAMIT and HYDROSTAR, with special focus on the resonance in the gap between vessels. It was pointed out that accurate linear damping coefficients needed to be obtained experimentally for implementation into the diffraction software because the latter does not account for viscous dissipation.

Teigen and Niedzwecki (1999) and Xie *et al*. (2008a) analyzed a coupled mini-TLP and tender barge system subject to benign sea conditions based on the experimental data obtained during model testing. The former study validated the design of this configuration including that of the soft connection consisted of fender and mooring lines, with particular focus on the coupled motion responses under design ultimate limit state. The latter utilized statistic analysis to further investigate the coupled motions between the mini-TLP and the barge. A similar scheme was used in a more recent study by the same authors to investigate a ship moored to a rigid barge (2008b), the procedures presented provide an important part of the current research study.

1.2. Reverse Multi-Input/Single-Output (R-MISO) system identification method

System identification in general is a procedure that selects a model structure, then computes and evaluates the model's properties. It is repeated until the results deem to be

satisfactory. There is no unique way to describe a system and estimate such descriptions, which results into various versions of system identification methods. They can be classified as parametric and non-parametric in either time domain or frequency domain. Imai *et al.* (1989) reviewed some of the most commonly used methods relevant to the identification of dynamic behavior of structures under various environmental loads. These include techniques based on least squares, instrumental variable and maximum likelihood for linear systems, and a technique utilizing extended Kalman filter for nonlinear systems.

One can further narrow down the application of system identification method to ocean engineering field. Kalman filter, a recursive filter that estimates the state of a dynamic system from a series of noisy measurements, was used by Yun and Shinozuka (1980) to identify hydrodynamic coefficients associated with the Morison's equation. Another technique called neural network approach (Haddara and Xu, 1998) was adapted from aeronautic applications. In this approach, the input feeds into first layer 'neurons', and the outputs of this layer feed into 'neurons' of the second layer and so on. All unknown parameters of a ship are lumped together in one function that can be uniquely determined using the neural network identification technique. Estimation-before-modeling technique was also originated from aeronautic applications and can be used for ship maneuvering problems (Yoon and Rhee, 2003). It is a two-step procedure using first extended Kalman filter and modified Bryson-Frazier smoother to estimate motion variables and hydrodynamic force before estimating the hydrodynamic coefficients by means of regression analysis. In a recent study, Varadarajan and Nagarajaiah (2008) developed a Hilbert transform based algorithm for the identification of the response of offshore systems. Hilbert transform was applied on the input data and the intrinsic mode functions related to the structure response. Frequency response function is then used to represent the result of Hilbert transform identification.

Besides the above mentioned works, a group of studies were dedicated to a method called the Reverse Multi-Input / Single-Output (R-MISO) technique which is a major focus of the present investigation due to its robustness and adequacy for nonlinear system application. The procedure reverses the roles of input and output functions of a given model in order to convert a nonlinear system with feedback to a set of linear systems without feedback. The removal of the feedback term eliminates the otherwise required time-consuming iterative procedures. For this reason the R-MISO method performs better than the conventional direct method when analyzing nonlinear systems. This frequency domain analysis tool can also assess the individual contributions of each parameter in the proposed nonlinear model. One of the advantages of this method is its flexibility for the choice of nonlinear terms whose suitability to the model can be revealed by computing the final coherence functions.

The origin of the R-MISO method can be traced back to Bendat and Piersol's paper (1982) on single input / single output (SI/SO) square law systems. A procedure was proposed where the single input and its squared value were both used as input data; by such manipulation the original SI/SO system becomes a two-input / single output (TI/SO) system.

In 1988, Rice and Fitzpatrick extended this approach to analyze arbitrary nonlinear dynamical systems in the frequency domain using spectral methods. The R-MISO technique procedure was later discussed in a paper on the identification of damping coefficient in a SDOF system (1991a). The same year, the reverse path technique was extended to the application to a MDOF nonlinear system (Rice and Fitzpatrick, 1991b). It was advised to consider different excitation conditions to check the consistency of the identified parameters.

The procedure of the R-MISO method was presented in detail by Bendat (1990) and in his subsequent works (Bendat *et al*., 1992, 1993). The spectral analysis techniques used

for the method were explained and many classes of practical engineering systems featuring nonlinearities in parallel and in series were presented. The description of the relationship between nonlinear system input and output as well as the techniques for conditioning these data laid the foundation for the R-MISO method. Different types of nonlinear systems including Duffing, Van der Pol, Mathieu, and Dead-Band systems were simulated in order to validate the method. It was found that it correctly identified nonlinear system parameters even for nearly-linear systems. Physical parameters described with memory functions of exponential analytical form can also be identified using the same technique as demonstrated by Bendat *et al.* (1995). The application of the R-MISO method was later illustrated by the case studies of a naval frigate and a barge (1998) with special nonlinear models. Applications for more complex MDOF systems in the oceanographic, automotive and biomedical fields were also presented in this publication.

In a study conducted by Narayanan and Yim (2000), the nonlinear damping coefficients were successfully identified using the R-MISO method. Comparison was done for three different models: nonlinear-structure linearly-damped model, nonlinear-structure coupled hydrodynamically-damped model, and nonlinear-structure nonlinearly-damped model. The last one was found to be the most appropriate model and this demonstrates the importance of the quadratic restoring force polynomial term to the nonlinear coherence estimates of the model.

Selvam and Bhattacharyya (2001) developed an iterative scheme for the identification of the hydrodynamic coefficients in the relative velocity model based upon Morison's equation. Four different data combination scenarios were considered. Their findings showed that the R-MISO approach was robust for both weak and strongly nonlinear systems. More recently (2006), they studied the coupled surge-pitch response of a moored floating body in random waves and applied the system identification method to

analyze not only the frequency dependent diagonal terms, but also the off-diagonal terms of the added mass and damping matrices.

Niedzwecki and Liagre (2003) studied a single marine riser with general damping restoring types of nonlinearities in random seas. Mathematical marine partial differential equations were derived and the formulation is verified by using both simulated white noise wave excitation and measured test data. The R-MISO method was used in these cases and it was shown that it can accurately recover frequency dependant hydrodynamic parameters for each mode of vibration. They extended this methodology formulation to investigate the motion behavior of a mini-TLP (Liagre and Niedzwecki, 2003). In their study they illustrated the use of rigid hull data in the analysis of the compliant platform. Bounds were set for frequency range of interest determined by coherence analysis. The predominant surge, pitch and heave motions, as well as their cross-coupling were investigated. The overall results showed that the proposed model was fine and demonstrated a strong consistency for the predominant surge motion.

Rodrigues and Falzarano (2001), Cheng and Falzarano (2003), then Falzarano, Cheng and Rodrigues (2004) studied the transit draft heave motion of a Mobile Offshore Base (MOB) in both head and beam seas. Because of the inherent nonlinearities of the MOB due to minimum freeboard as well as green water over the pontoon tops, the R-MISO method was shown to be a robust tool for the applied case. In head sea configuration, it was found that for large amplitude nonlinear motions of the MOB, the cross-coupling added mass and linear damping coefficients are non-zero due to the asymmetric immersion of the lower hull and would not have been identified with numerical simulation. In beam seas, the R-MISO method identified a significant nonlinear heave damping compared to a nonlinear roll damping expected for conventional ships.

1.3. Research objective

To the author's best knowledge, the application of the R-MISO method was reported in open literature only for single body systems. The current research has the objective to extend the application of this method to two-body systems. Due to the complex motion behavior of multi-body systems the nonlinear terms to be used in the equation of motion may not always be evident. A pre-analysis of the motion and mooring force time series is needed to establish the appropriate mathematical model based on the understanding of the physical properties of the system. Statistical tools can be used to perform this pre-analysis.

A two-body system consisting of a moored ship and a fixed barge will be used as example of illustration throughout the text. In the first part of this study, statistical tools including statistical parameters, spectral densities and coherence functions will be used to provide an overview of the general response behavior of the ship and barge system. The R-MISO method will then be applied to the single barge for the illustration of the method and for comparison purpose. And finally the reverse method will be extended to the ship and barge two-body system. Several issues specific to its application to two-body systems need to be solved including the computation load, the cross-coupling between the vessel motions, as well as the interpretation of the results. Three case studies will be discussed including the barge pitch motion for comparison with the same motion in the single body case, the ship roll motion in head seas to show the effect of interaction and finally the vertical ship heave motion in both head and quartering seas.

Author(s)	Date	Application	Method utilised	Contribution
Buchner *et al.*	2001	Turret-moored LNG FPSO / LNG carrier, with mechanic connections. JONSWAP waves. Various wave headings.	Time domain simulation.	Demonstrated the importance of applying matrix of retardation functions, free surface lid and viscous damping for a more accurate prediction of respectively the main motions, the drift forces and the low frequency motion responses.
Clauss, Jacobsen	2005	Semi-submersible / barge, without mechanic connections. Regular wave trains. Head seas.	Transformation method from frequency- to time-domain.	Retained the computational efficiency of frequency domain method while analysing hydrodynamic coupling and memory effects under time domain. The impact of a wave train containing wave packet with resonance components was shown.
Koo, Kim	2005	Turret-moored FPSO / tanker, with mechanic connection. JONSWAP waves. Head seas at various periods.	Time-domain simulation based on an exact method called Combined Matrix Method (CMM).	All vessel and line dynamics and their interactions were considered. The results showed the importance of cross-coupling terms in side-by-side mooring configurations.
Teigen, Niedzwecki	2006	Rigid twin barges, without mechanic connections. Regular waves. Various wave headings, periods.	Numerical simulation with second order panel code WAMIT.	Both linear and second order wave effects around the twin barges were studied. Second order wave amplifications in the gap and at the trailing end of the vessels were observed.
Lee *et.al*	2008	Floating terminal / LNG carrier, With mechanic connections. Irregular waves. Various wave headings.	Potential-viscous hybrid time domain simulation.	The dynamic coupling between the floating-body motions and the inner-tank sloshing was investigated. Intensification of both tank sloshing and vessel motions were observed in multi-body systems.
Xie *et al.*	2008	Moored Mini-TLP / barge, with mechanic connections. JONSWAP waves. Wind, current. Various wave headings.	Statistical analysis of model test data.	Showed the use of statistical tools in both time and frequency domain for the analysis of a two-body system. The effects of wave heading change on relative motions of the vessels and on fender wave elevation were studied.

Table 1.1 Summary of selected papers on side-by-side moored two-body system problem.

Author(s)	Date	Application	Contribution
Bendat	1990	Generic SDOF systems.	The procedure of the R-MISO method was presented in detail for SDOF system. The spectral analysis techniques used for the method were explained and many classes of practical engineering systems featuring nonlinearities in parallel and in series presented.
Rice	1991	Generic MDOF systems.	The use of R-MISO was extended to MDOF systems. The proposed method is suitable for the analysis of both systems with significant cross-damping and highly coupled nonlinear systems.
Narayanan, Yim	2000	Moored neutrally buoyant sphere. Regular and random waves.	The nonlinear-structure nonlinearly-damped mode was found to be the most appropriate model for the presented system. It demonstrated the importance of the quadratic restoring force polynomial term to the nonlinear coherence estimates of the model.
Niedzwecki, Liagre	2003	Single marine riser. Random waves.	R-MISO method was extended to address distributed-parameter MDOF systems with general damping-restoring types of nonlinearities subject to random excitation. Emphasis was placed on motions in-line with the wave propagation. The value of the system parameters were recovered for each mode of vibration.
Liagre, Niedzwecki	2003	Mini-TLP. Random waves.	The motion behavior of a mini-TLP was analyzed using R-MISO method. The use of rigid hull data in the analysis of the compliant platform and the use of frequency range bounds were underlined. The predominant surge, pitch and heave motions, as well as their cross-coupling were investigated.
Falzarano	2004	Mobile Offshore Base (MOB). Random waves. Head seas.	The transit draft heave and pitch motions of the MOB were studied. Non-zero cross-coupling added mass and linear damping coefficients was found for the symmetrical vessel due to asymmetric immersion of the hull, phenomena that would not have been identified with numerical simulation.
Selvam, Bhattacharyya	2006	Floating half-spheroid. Pierson-Moskowitz spectrum waves.	A nonlinear two DOF system with surge-pitch coupling was studied. The constant linear and nonlinear stiffness coefficients were calculated and the frequency dependent added mass and radiation damping were estimated for both diagonal and off-diagonal terms.

Table 1.2 Summary of selected papers on reverse multi-input / single-output system identification method.

2. STATISTICAL ANALYSIS OF THE TWO BODY HYDRODYNAMICS

In this section, the use of statistical methods for the analysis of the hydrodynamic response behavior of a two-body system will be presented. Tools such as the usual statistical parameters, spectra and coherence functions were used to assess the general behavior of the system as well as the pattern of the mooring line and fender forces in random seas based on the experimental data obtained during the model tests. The causality between them, namely the effect of the relative movement on the connection system, was examined. The effect of tank waves on the general behavior of the system will also be discussed. The steps described here, as well as those on the system identification analysis in the next section, are general and applicable to many different cases. But for clarity the example of a moored ship and barge system will be used for illustration throughout the text.

2.1. Presentation of the ship / barge system

In the current study, a side-by-side moored two-body system consisting of a ship and a deep draft barge was investigated. The specification of this barge and ship system was developed based upon consideration of the loading and offloading operations for liquefied natural gas. The prototype ship had an overall length (LOA) of 187.1m, a beam of 25.6m. Its draft was variable and depended on the ship board cargo with 8.26 being the deep draft value and 4.76m the shallow draft. The ship contains three tanks of dimension 12.70m $\times$15.24m$\times$16.2m (length$\times$width$\times$height). The barge had a length of 160m with a beam of 60m. The draft of the barge relevant to the current investigation was set at 15m. The vessels were side-by-side moored together using two sets of two mooring lines, one set toward the bow and the other one toward the stern. Similarly, one fender system at each half of the vessels was installed. The instrumented fender system

was used to monitor the forces between the vessels. A sketch of the two-body system indicating the approximate location of the mooring lines and fenders, as well as that of the three tanks on the ship is illustrated in Figure 2.1. Complete information on the positive polarities of the vessel motions and those of the mooring line and fender forces is listed in Table 2.1.

The 1:50 model scale tests were performed at Offshore Technology Research Center (OTRC) in College Station, USA. The complete test program included basic single and twin barge configurations in addition to the barge / ship configuration studied in the present research work, subject to white noise, regular, random and directional waves. A total of slightly over 500 test runs were recorded with the number of channels of data per test varying from 12 for the wave calibrations to 66 for the later tests of the ship moored to the barge. Instruments such as wave gages, accelerometers, load cells, optical tracking, etc. were employed to obtain the desired measurements. The selection of the load cells was based upon initial estimates of wave forces and moments obtained using the industry standard code WAMIT (Niedzwecki, 2007). The load cells provided direct measurement of surge, sway and heave (translational motions) forces and the pitch, roll and yaw (rotational motions) moments on the rigid barge and ship. In addition, measurements obtained by accelerometers were used for the derivation of necessary information needed for system identification analysis. For the measurement of wave elevation inside the tanks, only the aft tank was instrumented with six wave gages. The mooring lines were modeled using springs lines whereas the fender was modeled by mean of spring rods fixed on the ship with roller contact on the barge. When the mooring springs were calibrated, the measured spring constants were 0.27448 lbs/inch for bow line #1, 0.27262 lbs/inch for bow line #2, 0.27626 lbs/inch for stern line #1 and 0.27343 lbs/inch for stern line #2. In prototype scale, the density difference between fresh water and salt water was taken, these values were respectively 578 N/m, 575 N/m, 582 N/m, and 576 N/m.

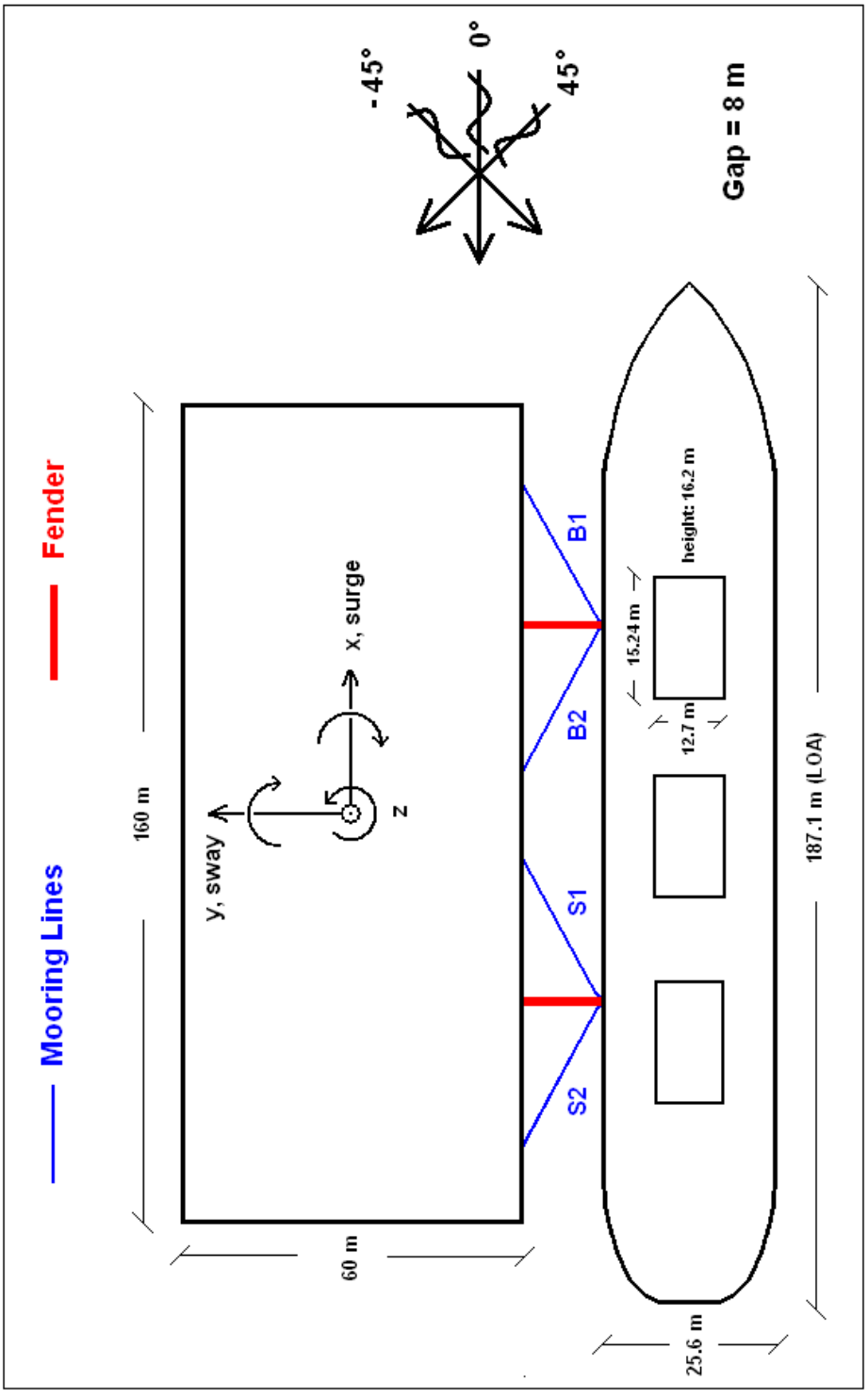

Figure 2.1 Configuration of the side-by-side moored ship / barge system

Surge motion	Sway motion	Heave motion	Roll motion	Pitch motion	Yaw motion	Mooring line force	Fender force
Toward bow	Toward port	Up	Port side up	Bow down	Counter clockwise from above	Tension	Compres-sion

Table 2.1 Positive polarities of the vessels motions, mooring line and fender forces.

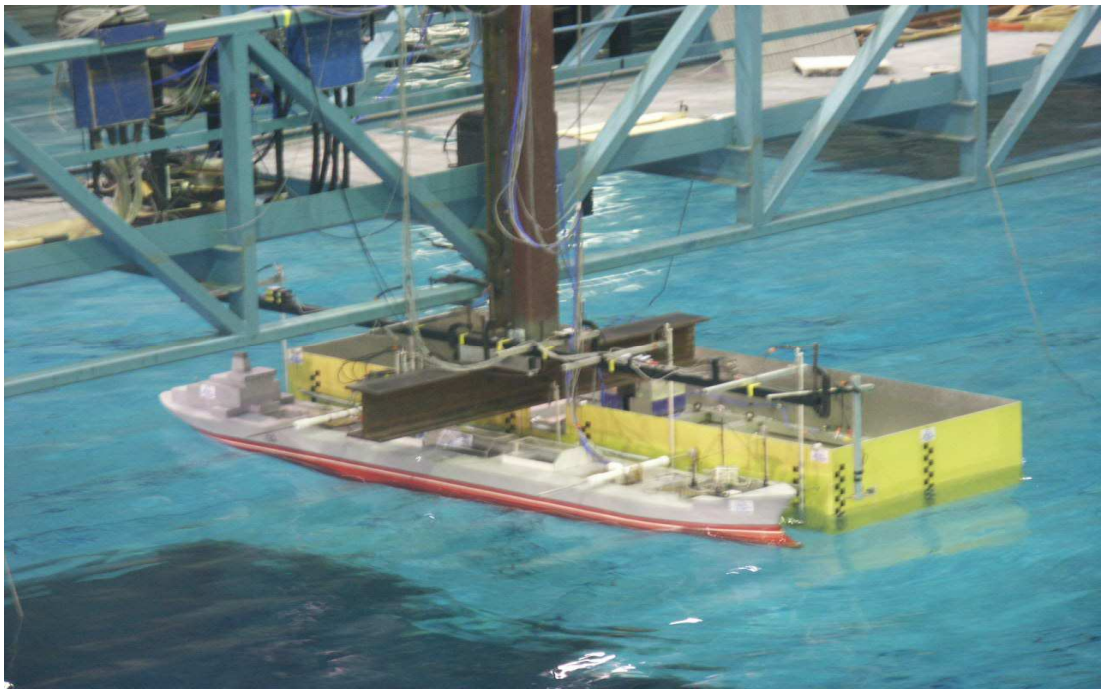

Figure 2.2 Model ship / barge system in head seas configuration

A picture of the ship-barge system taken during the model testing is presented in Figure 2.2. The origins of barge-fixed and ship-fixed coordinate systems are at keel / midship / centerline because it is preferable to pick a reference point that would remain constant considering the fact that different vessel drafts were tested.

The present study focuses upon the analysis of the experimental data related to this barge / ship system in random seas. A mild operational environment was simulated with a wave of significant wave height of 2m and period of 10.2s. The barge was fixed via the six degree of freedom load cell configuration during the testing whereas the ship was moored with a gap width of 8m between the two vessels. Both head seas (0°) and quartering seas (45° and -45°) conditions were tested for comparison. Different load levels of the ship, namely 80% water filled tanks vs. 10% filled tanks, were considered for each heading condition in order to assess the effect of the loading condition on the response behavior of the vessels. Note that the tests at 45° heading were performed only for the 80% filled condition.

2.2. Overall motion behavior

The barge was fixed by the 6 DOF load cell at its center during the model tests, thus the translational motions can be considered as zero. However some barge rotations were observed due in part to the large size of the barge. Table 2.2 indicated the standard deviation of the three rotational motions of the barge that are roll, pitch and yaw, each of them compared to the corresponding values of the ship motions. It is clear that all the three rotational motions are much smaller in the case of the barge, especially for the roll motion. For this reason, in the subsequent studies the barge roll motion will be neglected in the analysis of the two body system motion behavior as it does not contribute to any relative movements. The pitch and yaw motions, although they remain small, will be kept for the sake of the completeness of the analysis and to insure the

accuracy of the mooring line and fender force decomposition discussed in a later section. Note that the barge pitch and yaw motions were derived from the measured acceleration data using an integration algorithm in frequency domain and a geometrical derivation explained in Appendix A.

The relative movements between the two bodies can be used to study the overall motion of the two body system. They are simply obtained by subtracting the barge motion from the ship motion. Table 2.3 provides a listing of the means, standard deviations and extreme values of the motions in all six degrees of freedom in both head and quartering seas for 80% loaded and 10% loaded tanks. All these time series can be roughly considered as normally distributed considering their skewness and kurtosis.

A noticeable difference between the 80% and 10% filled cases, as shown in Table 2.3, is the higher surge fluctuation for the system with shallow draft ship. It is understandable that when the tanks contain less fluid the ship is more sensitive to the incident waves due to its lighter weight. Another interesting observation is that the relative roll motion is important in the head seas configuration although the two bodies are symmetric in the longitudinal direction. This phenomenon is due to the hydrodynamic interaction between the two vessels, more specifically the action of a pumping wave developed in the gap between the barge and the ship.

The -45° heading configuration corresponds to the case where the ship is shielded from the incident wave by the barge and when the 45° heading configuration occurs the ship is exposed. The standard deviation of the motions show large fluctuation in all the six time series of the relative motions in the exposed case compared to the shielded and head seas configurations. This result indicated that the shielding effect provided by the barge was able to effectively reduce the overall motions of the ship. The magnitude of the motion fluctuations in the shielded case is similar to that of the head seas configuration.

	80%, 0°	80%, -45°	80%, 45°	10%, 0°	10%, -45°
Barge roll	0.005	0.01	0.01	0.004	0.01
Ship roll	0.47	0.39	1.11	0.39	0.32
Barge pitch	0.10	0.18	0.09	0.10	0.18
Ship pitch	0.36	0.48	0.86	0.40	0.44
Barge yaw	0.03	0.05	0.04	0.03	0.05
Ship yaw	0.21	0.18	0.31	0.17	0.17

Table 2.2 Comparison between the standard deviations of the barge and ship rotation motions (unit: degree)

		80%				10%			
		μ	σ	min	max	μ	σ	min	max
Head seas (0°)	Surge	-0.53	0.03	-0.63	-0.45	-0.08	0.15	-0.62	0.41
	Sway	-0.02	0.17	-0.59	0.77	-0.35	0.13	-0.88	0.34
	Heave	0.08	0.22	-0.72	0.95	1.22	0.20	0.46	2.04
	Roll	-0.08	0.47	-1.94	1.82	-0.01	0.39	-1.59	1.84
	Pitch	0.05	0.29	-1.02	1.18	-0.17	0.33	-1.33	1.04
	Yaw	0.01	0.21	-1.03	0.81	-0.02	0.17	-0.93	0.53
Quartering seas (-45°)	Surge	-13.0	0.02	-13.16	-12.96	-12.8	0.15	-13.47	-12.22
	Sway	5.29	0.12	4.80	5.81	5.12	0.11	4.71	5.51
	Heave	-0.03	0.17	-0.68	0.61	1.21	0.17	0.59	1.84
	Roll	-0.19	0.39	-1.89	1.48	-0.29	0.32	-1.43	0.98
	Pitch	-0.05	0.56	-2.17	2.04	-0.11	0.52	-2.16	1.91
	Yaw	-0.00	0.20	-0.81	0.74	-0.08	0.19	-1.01	0.78
Quartering seas (45°)	Surge	12.10	0.47	10.80	13.47	--	--	--	--
	Sway	4.88	0.31	3.82	5.88	--	--	--	--
	Heave	0.37	0.46	-0.19	2.19	--	--	--	--
	Roll	-0.10	1.11	-4.77	4.61	--	--	--	--
	Pitch	0.18	0.88	-3.77	4.01	--	--	--	--
	Yaw	-0.12	0.31	-1.21	0.90	--	--	--	--

Table 2.3 Sample means (μ), standard deviations (σ), minima and maxima of the relative motions (units: meters for surge, sway, heave and degrees for roll, pitch and yaw)

Since the polarities were taken into account, the signs indicated whether the two vessels were driven closer or further apart. It is especially informative when considering the relative sway motions in order to monitor the gap distance between the ship and the barge: in head seas for instance a positive relative sway indicates a decrease in this distance whereas a negative value the opposite. Note that the values of the three translational motions indicate in fact the position of the ship with respect to its original reference center. The mean values of the surge and sway motions suggested that the centers of vessels stayed essentially inline in the y-direction in head seas, whereas the ship shifted backward in respect of the barge in the -45° heading condition and forward in the 45° heading condition. In addition, in both the shielding configuration and exposed configuration the distance between the two vessels became larger. This phenomenon is confirmed by the observation of the recorded model tests. The observation made for the configuration where the ship is exposed (45°) is somehow counter intuitive. The system parameters identified in later sections using the Reverse Multiple-Input / Single-Output (R-MISO) method are expected to give further information in the interpretation of such result.

2.2. Mooring line and fender forces

Similarly the forces of the four mooring lines and the two fenders were compared by using the mean and standard deviation of the data. This information is summarized in Table 2.4. The letter ‘B’ stands for ‘bow’ and ‘S’ for ‘stern’. The numbers provided already have their pretensions subtracted, thus a positive mooring line force indicates a tension force whereas a positive fender force indicates compression. During the model tests, the fenders were deliberately adjusted so that they would remain in contact with the barge to avoid any difficulty in numerical modeling. The similarity between the forces of line 1 at the bow and line 1 at the stern, as well as that between the forces of lines 2 at the bow and line 2 at the stern is due to the symmetry of the mooring system used. For all the four mooring lines and the two fenders, the in-line forces are higher for

the 10% filled case in both head and quartering seas due to the larger motions observed and explained in the previous section. Similarly the force fluctuations are higher for the configuration where the ship was exposed to the incident waves. This is consistent with the observed relative motions.

Figures 2.3a thru 2.3d illustrate the spectral densities of the mooring line forces in different cases which provide another perspective to examine the comparative force pattern. Each of the spectra shows a main peak in lower frequencies and a secondary peak corresponding to the wave frequencies. At the wave frequencies, a slightly larger energy content was observed for bow line 2 and stern line 1, but overall the mooring line forces are small compared to first order wave forces. The lower frequency peaks were of similar amplitude for the different cases. In the 80% filled configuration, the main peaks have a period around 52 s which corresponds to the surge peak period obtained from the decay test for the moored ship. In the 10% filled configuration, the main peaks of the breast line forces spectra were centered about a surge period of 45s which is consistent with the decrease of vessel mass.

To find the impact of the relative motions on the mooring line and fender forces, the time series of the relative motions can be plotted near the moment of occurrence of the maximum mooring line / fender forces (Naciri *et al*., 2007). Using this approach the relative motions in all six degrees of freedom and their relationship to each mooring line and fender load was studied. Since it was mentioned earlier that the surge motion is closely correlated to the mooring line forces, the example of the surge motion near the maximum force of a mooring line will be discussed. Figure 2.4 presents a plot of the relative surge time series around the occurrence of the maximum force of the mooring line which is indicated by the vertical line; the dash lines mark the extreme values of the entire surge time series. It can be seen that the maximum surge happens at the time when the maximum line force occurs. This confirms that the surge motion is indeed highly correlated to the line forces.

		80%				10%			
		μ	σ	min	max	μ	σ	min	max
Head seas (0°)	Line B1	16	16	-46	80	12	17	-46	92
	Line B2	6	16	-62	66	-1	17	-64	55
	Line S1	16	16	-57	76	8	17	-49	73
	Line S2	6	15	-57	62	-7	16	-77	48
	Fender B	-4	103	-229	228	13	133	-263	315
	Fender S	-25	103	-241	183	63	113	-193	304
Quartering seas (-45°)	Line B1	8	16	-60	67	13	17	-55	88
	Line B2	2	17	-77	68	-3	17	-63	59
	Line S1	7	16	-55	70	11	17	-50	74
	Line S2	-1	15	-67	62	-5	15	-58	54
	Fender B	-17	118	-277	238	-17	123	-313	238
	Fender S	-20	104	-277	184	-13	97	-230	173
Quartering seas (45°)	Line B1	3	24	-114	121	--	--	--	--
	Line B2	-10	27	-129	120	--	--	--	--
	Line S1	0	27	-124	131	--	--	--	--
	Line S2	-8	25	-110	109	--	--	--	--
	Fender B	0	116	-351	327	--	--	--	--
	Fender S	1	108	-278	305	--	--	--	--

Table 2.4 Sample means, standard deviations, minima and maxima of the mooring line and fender forces (unit: kN)

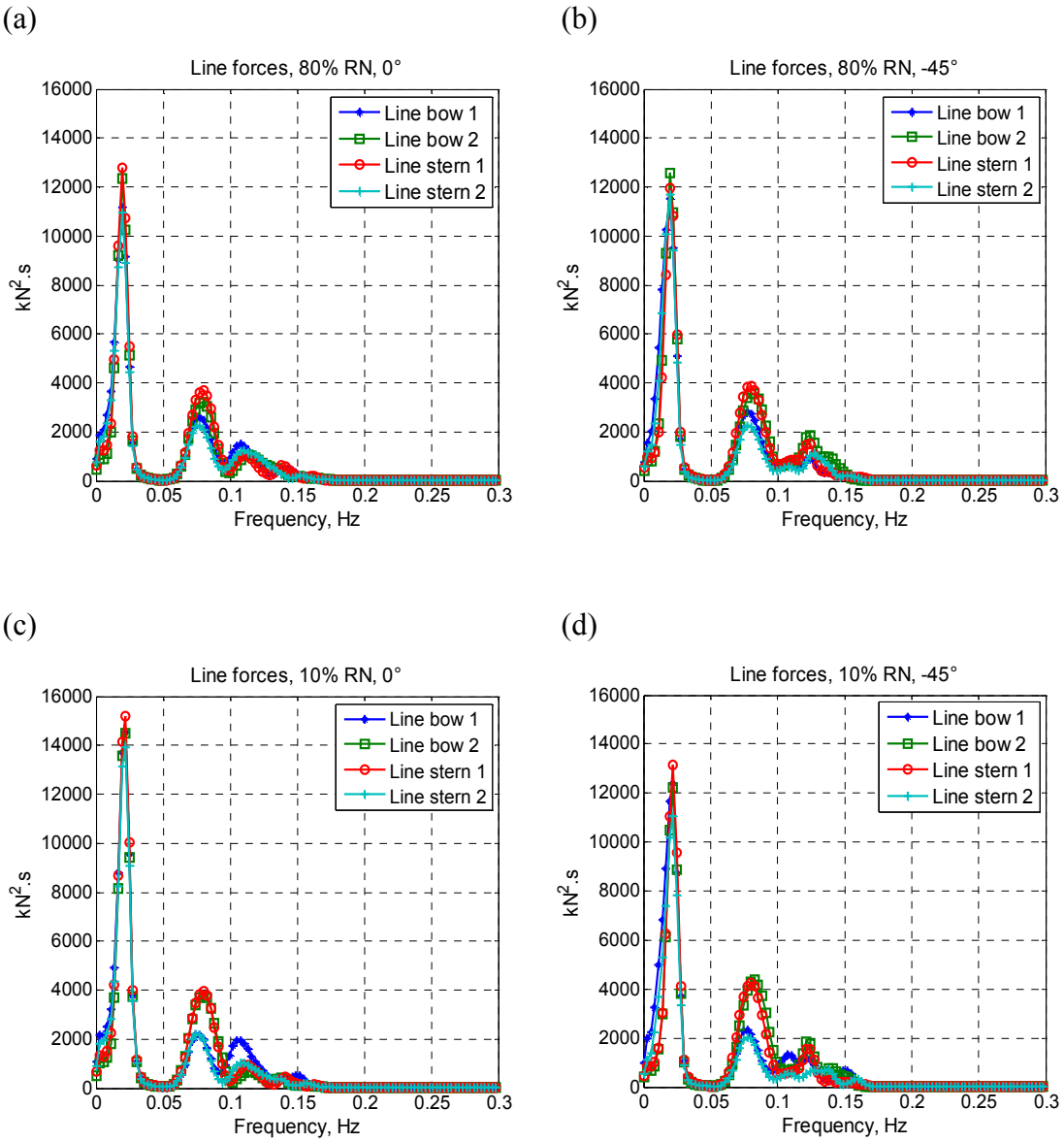

Figure 2.3 Spectral densities of the in-line forces of the mooring lines connecting the ship and the barge for (a) 80% filled tanks in head seas; (b) 80% filled tanks in quartering seas; (c) 10% filled tanks in head seas; and (d) 10% filled tanks in quartering seas.

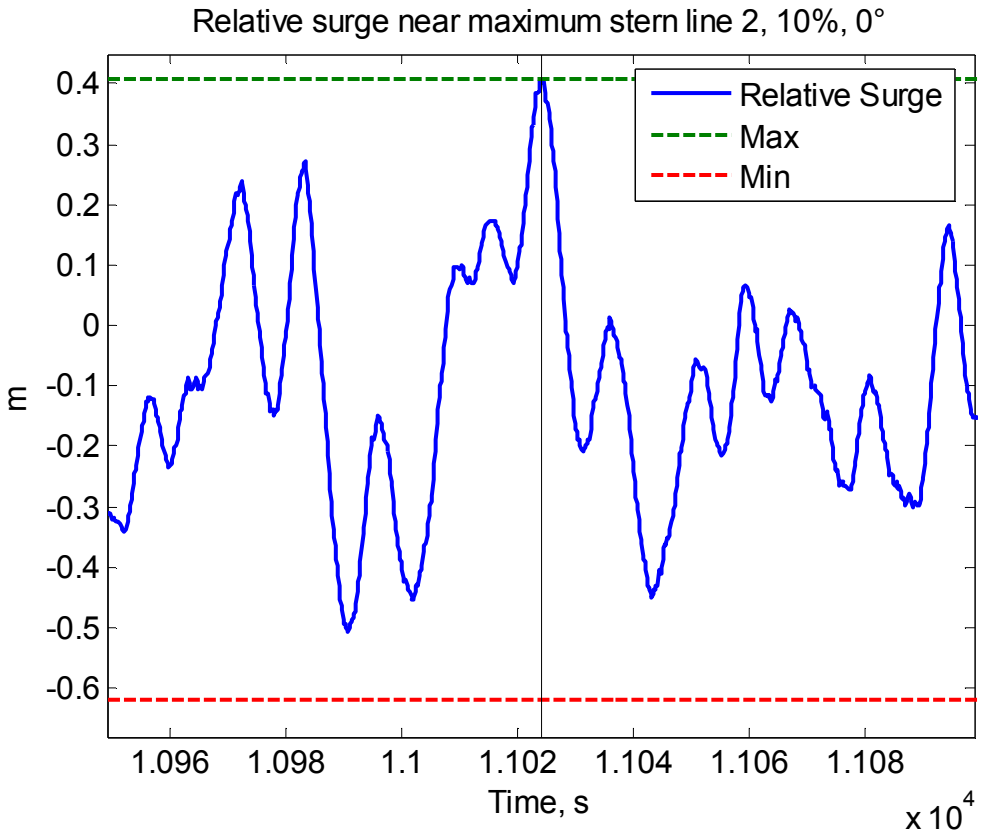

Figure 2.4 Relative surge near maximum force of a mooring line in head seas, with 10% filled tanks.

This correlation can be visualized in frequency domain as well by analyzing the cross-spectral density and the coherence function between the time series of surge motion and the mooring line force. Figure 2.5 again shows that there exists a high correlation between the two time series since the values of coherence functions are nearly one. In addition, the phase spectrum suggests that in this context bow line 1 and stern line 1 behave similarly and the same for bow line 2 and stern line 2, which is due to the symmetry of the mooring system. Note that in this figure only the frequency ranges corresponding to significant energy were considered, in the current case namely the lower frequencies and the wave frequencies.

The same cross-spectral analysis approach was used to examine the relationship between several other motion force pairs of interest. The behaviour of the surge / fender force pairing is shown in Figure 2.6. A large phase difference between the bow and stern fender forces is observed as well as relatively low coherence. This is consistent with the phase difference between lines 1 and lines 2 indicated by Figure 2.5. It can be concluded that the vessels are not quite collinear to each other in the sea states considered. The time series that shows the highest correlation with the fender force is the relative roll motion. As illustrated by Figure 2.7, a relatively high value of coherence function was observed between roll and fender force at the frequency range of interest. Note that this correlation relationship is not as pronounced as the one existing between the surge motion and the mooring line forces, indicating more of an impact of the system nonlinearity.

A review of the complete set of motion / force pairs show that in head seas, the relative surge and pitch are highly correlated with mooring line forces meaning these movements are the main responsible of the compression and tension of the lines. At the same time, the roll motion exerts a significant influence on the fender force although more nonlinear behaviour should be expected. In quartering seas, in addition to surge and pitch, roll and sway motions are also sources of influence to the line forces, whereas both roll and pitch are highly correlated with the fender forces.

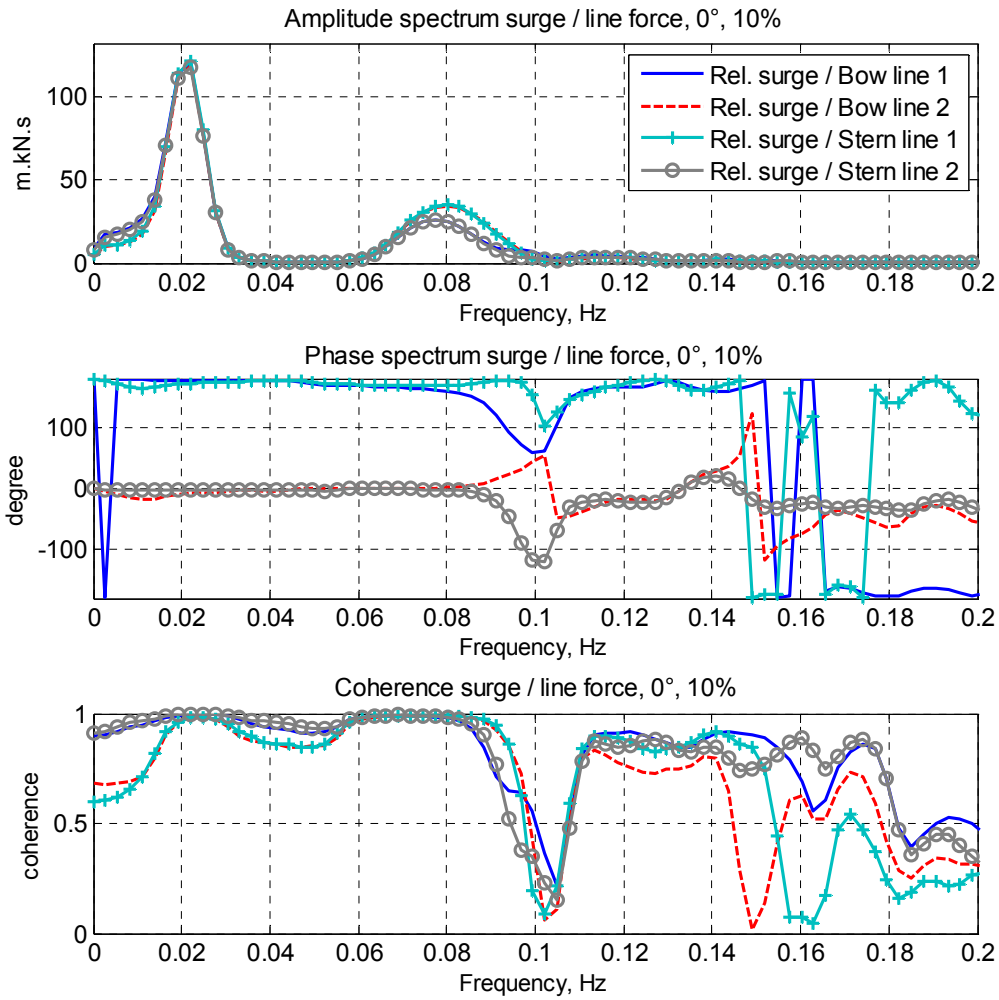

Figure 2.5 Cross-spectrum and coherence function between the surge motion and the mooring line forces in head seas, with 10% filled tanks.

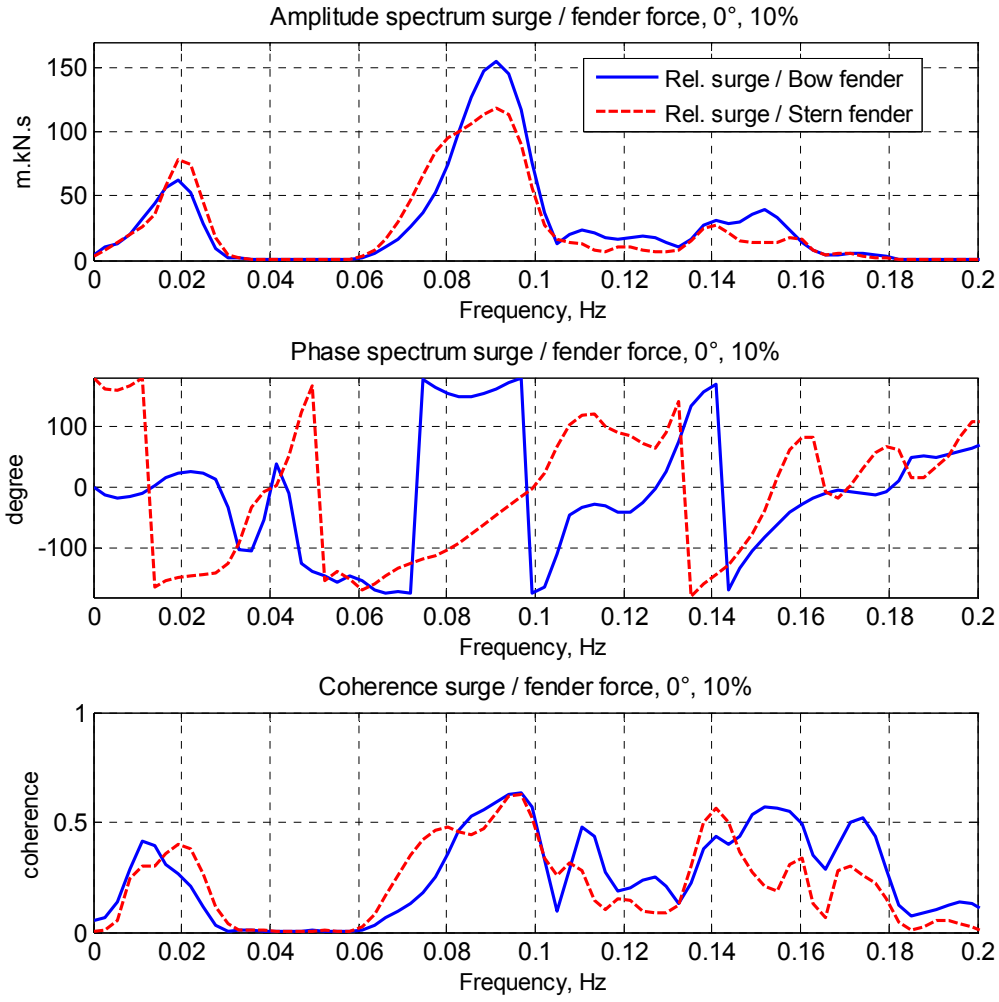

Figure 2.6 Cross-spectrum and coherence function between the surge motion and the fender forces in head seas, with 10% filled tanks

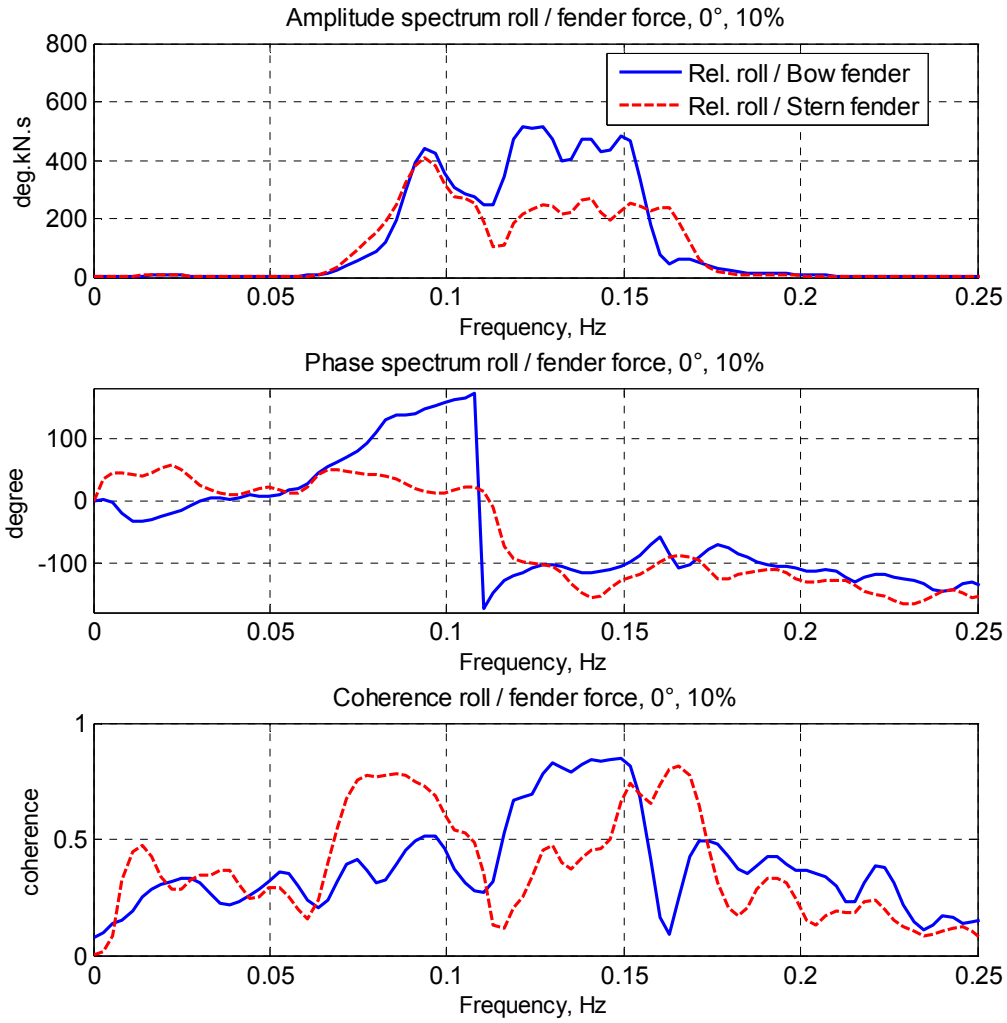

Figure 2.7 Cross-spectrum and coherence function between the roll motion and the fender forces in head seas, with 10% filled tanks

2.3. Influence of the tank waves

The sloshing of waves inside the three partially filled fluid tanks on board of the ship can influence the motion behaviour of the vessel. A total of six wave gages were installed inside the aft tank to measure the tank wave elevation. Five of wave gages were aligned along the tank centreline and set equally 2.50 m apart. The sixth one was installed in the transverse direction with the same separation distance as shown in Figure 2.8.

The natural frequency of the nth mode of the tank wave can be calculated based on the linear wave dispersion relationship:

$$\omega_n = \sqrt{g k_n \tanh\left(k_n h\right)} \tag{2.1}$$

Where k_n is the wave number corresponding the nth mode of the tank wave. Its value can be derived from the following form of velocity potential itself obtained using the separation of variable method:

$$\phi = A\cosh\left(k\left(z+h\right)\right)\cos kx\cos\omega t \tag{2.2}$$

The boundary conditions yield the value of k_n:

$$k_n = \frac{n\pi}{l}, \qquad n = 1, 2, 3, \ldots \tag{2.3}$$

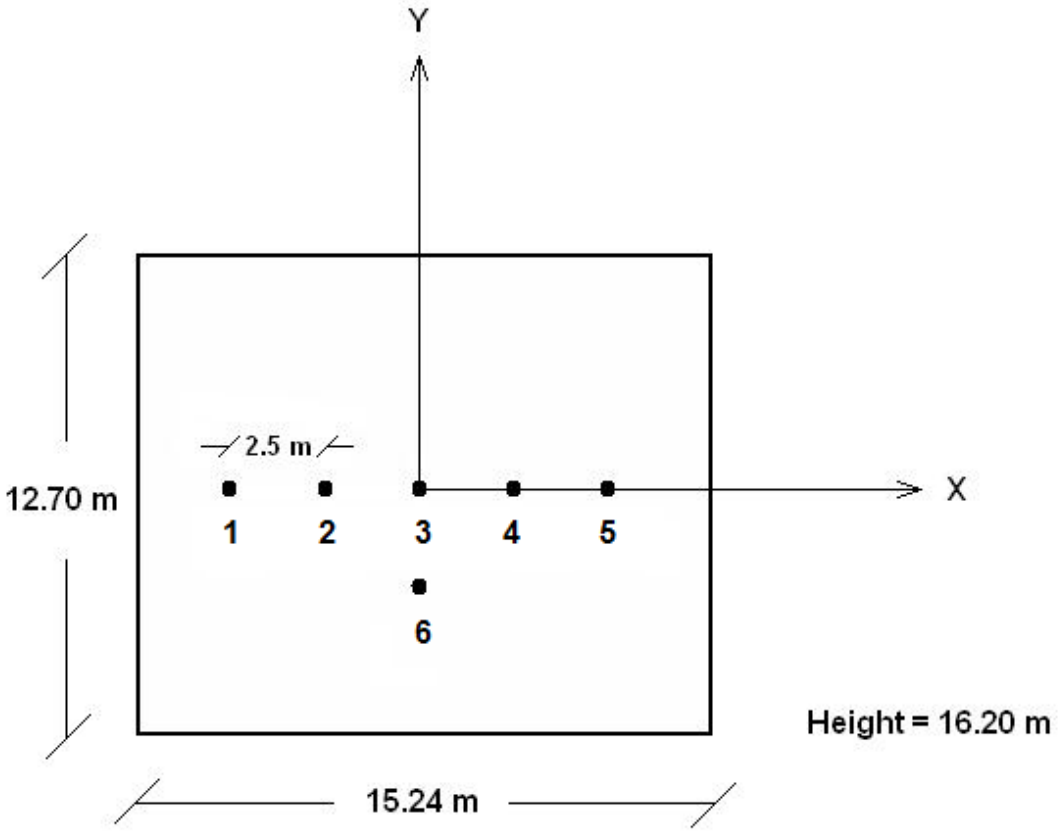

Figure 2.8 Distribution of the wave gages inside the aft tank of the model ship.

The frequencies of the first mode of the sloshing for both 80% and 10% filled cases were calculated and they are respectively 0.23 Hz (T = 4.3s) and 0.13 Hz (T = 7.7s).

It was initially planned to plot the profiles of the tank waves based on the data measured by the probes and compare these experimental wave profiles with the known theoretical profiles of the different modes of sloshing. Depending on the modes of sloshing the impact of the tank wave motion on the tank integrity can be different. However, the wave probes used were capacitance wave gages and did not perform well as hoped due to the small enclosure such as the tank. Consequently it was decided to use the response amplitude operators (RAO) to identify the global effect of the sloshing motions. If any peaks in the motion RAO correspond to the sloshing period then the sloshing may amplify the motion of the ship at that frequency. In the present case, none of such peaks were observed in the 80% filled case. However, for the 10% filled case, concentrations of energy were observed near the first mode of sloshing frequencies for roll motions in both 0° and -45° configurations and in the case of the pitch motion in the -45° configuration. Each of these findings are illustrated in Figure 2.9.

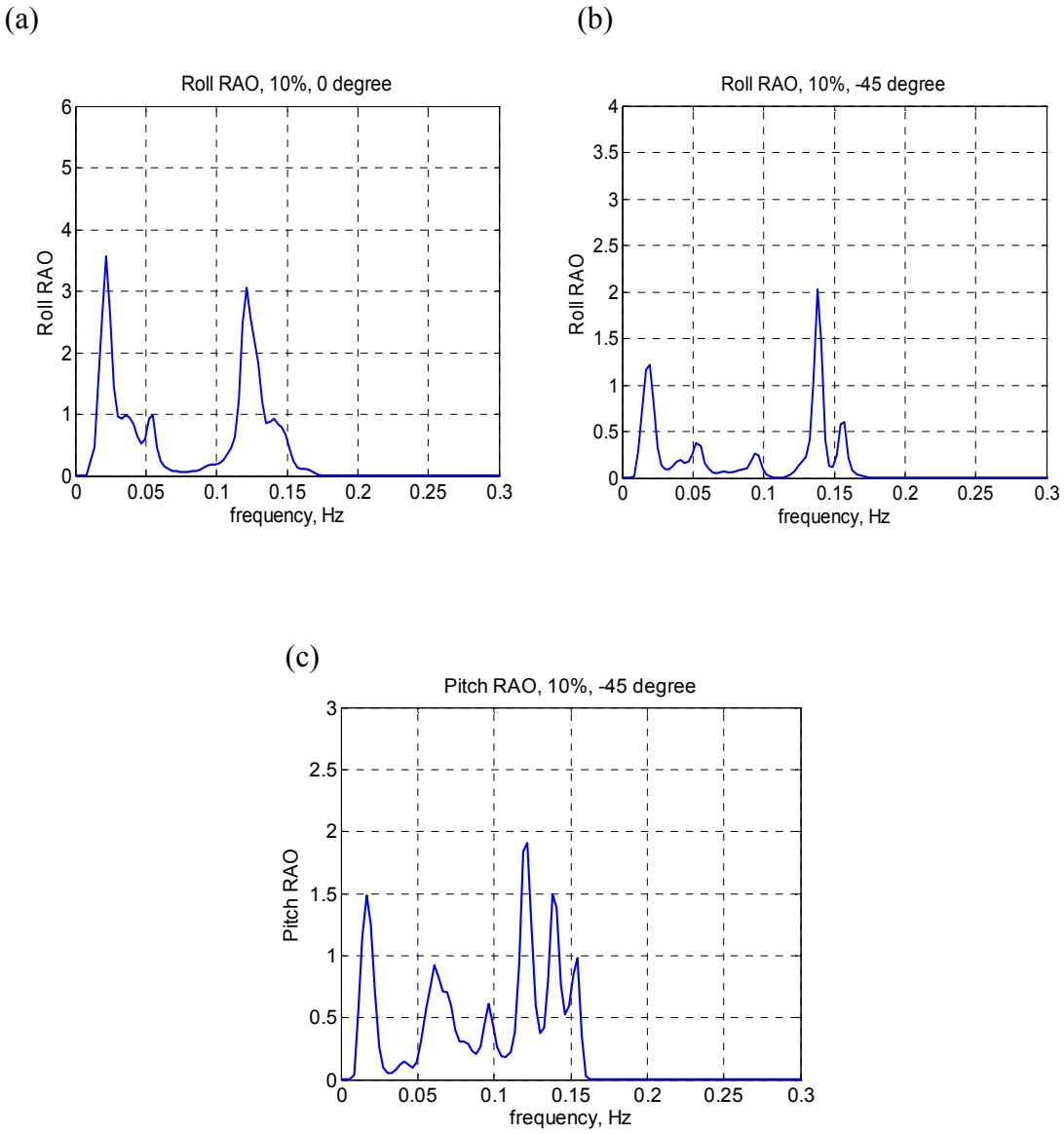

Figure 2.9 Motion response amplitude operators (RAO) of the (a) ship roll motion in 0° heading, (b) ship roll motion in -45° heading, and (c) ship pitch motion in -45° heading; in the case of 10% filled tanks.

3. IDENTIFICATION OF THE SYSTEM PARAMETERS OF THE SINGLE BARGE

The Reverse Multi-Input / Single-Output (R-MISO) method is an efficient system identification technique that allows for the estimation of the key system parameters. In the present section, this method is applied to the single barge data discussed in the previous section. The objective is to investigate the values and nature of the R-MISO output. Further, this is done in part to validate the program developed for later application to two body systems and for comparison between the motions of single and two-body systems.

3.1. Reverse Multi-Input / Single-Output (R-MISO) method

The Reverse Multi-Input / Single-Output (R-MISO) technique is a frequency domain system identification method that determines the system parameters of a proposed model based on measured input and output data. In a typical offshore body system, the system parameters include added mass, linear damping and stiffness as well as nonlinear damping and stiffness coefficients. The knowledge of these values from model testing data is important to validate and refine any numerical models that are developed for the analysis of the system.

To begin with, a set of possible nonlinear equations of motions will be given based on the physical knowledge of the system to be considered. The procedure converts the initial single-input / single-output nonlinear model into an equivalent dynamic multi-inputs / single-output linear model by reversing the roles of input and output functions. This manipulation eliminates the feedback terms necessitated by nonlinear systems that would otherwise require time-consuming iterative procedures. For this reason the R-

MISO method performs better than the conventional direct method when analyzing nonlinear systems. After the Fourier transform of the equation of motions, the reversed inputs need to be conditioned such that they each become uncorrelated. The knowledge of the measured original input and outputs allows for the recovery of the response transfer functions relating each reversed and conditioned input spectral density function to the output spectral density function. Once these response transfer functions are obtained, it is then possible to solve for the unknown system parameters. To assess the goodness of fit of each of the terms in the proposed model as well as the overall performance of the model, partial and cumulative coherence functions are used. For example, higher values of the coherence functions indicate that the model is more accurate. The partial coherence functions assess the proportion of the output spectrum that is due to each individual input term to the output through the corresponding response function. When a particular individual parameter contribution is quite low, it indicates that the parameter is not relevant and can be neglected in the equation of motion. For this reason, when deciding the form of the equation of motion at the beginning of the procedure, a lack of knowledge of the proper form of the nonlinearities is not an insurmountable problem. Arbitrary terms can be used and replaced if revealed to be irrelevant. This flexibility in choosing nonlinear terms as well as its proved robustness in applications makes the R-MISO method a good tool for analyzing nonlinear systems. The details of the calculation procedure for this method are well documented by Bendat (1990).

A Matlab program was written based on the steps described above and is used to analyze the single and two-body systems studied in the present research work. This program is validated by simulating a single degree-of-freedom (SDOF) case study discussed in Bendat's book (1990). The results provided by the program match well with the published results. Both the Matlab code and the comparison results can be viewed in Appendix B.

3.2. Equation of motion

In this section, the case of the fixed single barge will be studied. It will be later compared with the two-body system. The environmental conditions are the same as described in Section 2 with the peak period equals to 10.2 s and the significant wave height equals to 2 m. The equation of motion of the barge can be written in the following matrix form:

$$(M+a)\ddot{q}(t)+c\dot{q}(t)+kq(t)+dD(t)+rR(t)=F(t) \tag{3.1}$$

With:

$$\text{M = mass matrix} = \begin{pmatrix} m & 0 & 0 & 0 & mz_G & 0 \\ 0 & m & 0 & -mz_G & 0 & 0 \\ 0 & 0 & m & 0 & 0 & 0 \\ 0 & -mz_G & 0 & I_{xx} & 0 & 0 \\ mz_G & 0 & 0 & 0 & I_{yy} & 0 \\ 0 & 0 & 0 & 0 & 0 & I_{zz} \end{pmatrix} \tag{3.2}$$

Assuming the barge has two plans of symmetry, m is the mass of the barge and I_{xx}, I_{yy} and I_{zz} are the moments of inertia of the barge, and z_G is the vertical coordinate of the center of gravity in the barge-fixed reference system. Note that the center of gravity is different from the center of the reference system which is at the keel/center/midship. It is preferable to pick a reference point that would remain constant considering the fact that different barge drafts were considered during the model test.

$$\text{a = added mass matrix} = \begin{pmatrix} a_{11} & 0 & 0 & 0 & 0 & 0 \\ 0 & a_{22} & 0 & 0 & 0 & 0 \\ 0 & 0 & a_{33} & 0 & 0 & 0 \\ 0 & 0 & 0 & a_{44} & 0 & 0 \\ 0 & 0 & 0 & 0 & a_{55} & 0 \\ 0 & 0 & 0 & 0 & 0 & a_{66} \end{pmatrix} \tag{3.3}$$

The subscripts 1, 2, …6 correspond respectively to the vessel surge, sway, heave, roll, pitch and yaw motions.

$(M + a)$ forms the so-called virtual mass matrix.

The linear damping matrix c has the same structure as the added mass matrix. Whereas the linear stiffness matrix k has only three non-zero elements for a vessel with two planes of symmetry: k_{33}, k_{44} and k_{55}.

The nonlinear damping matrix d and the nonlinear stiffness matrix r are as followed if the second order terms are assumed to be negligible.

$$\text{d = nonlinear damping matrix} = \begin{pmatrix} d_{11} & 0 & 0 & 0 & 0 & 0 \\ 0 & d_{22} & 0 & 0 & 0 & 0 \\ 0 & 0 & d_{33} & 0 & 0 & 0 \\ 0 & 0 & 0 & d_{44} & 0 & 0 \\ 0 & 0 & 0 & 0 & d_{55} & 0 \\ 0 & 0 & 0 & 0 & 0 & d_{66} \end{pmatrix} \tag{3.4}$$

$$\text{r = nonlinear stiffness matrix} = \begin{pmatrix} r_{11} & 0 & 0 & 0 & 0 & 0 \\ 0 & r_{22} & 0 & 0 & 0 & 0 \\ 0 & 0 & r_{33} & 0 & 0 & 0 \\ 0 & 0 & 0 & r_{44} & 0 & 0 \\ 0 & 0 & 0 & 0 & r_{55} & 0 \\ 0 & 0 & 0 & 0 & 0 & r_{66} \end{pmatrix} \tag{3.5}$$

q and F are respectively the motion and force vector:

$$\text{q(t)} = \begin{pmatrix} x(t) \\ y(t) \\ z(t) \\ \phi(t) \\ \theta(t) \\ \psi(t) \end{pmatrix} = \begin{pmatrix} surge \\ sway \\ heave \\ roll \\ pitch \\ yaw \end{pmatrix} \tag{3.6}$$

Surge, sway, heave are the translational motions of the vessels respectively in the x-, y-, and z-axis. Roll, pitch and yaw motions are the rotational motions of the vessels around respectively the x-, y-, and z-axis.

$$\text{F(t)} = \begin{pmatrix} F_x(t) \\ F_y(t) \\ F_z(t) \\ M_x(t) \\ M_y(t) \\ M_z(t) \end{pmatrix} = \begin{pmatrix} surge\ force \\ sway\ force \\ heave\ force \\ roll\ moment \\ pitch\ moment \\ yaw\ moment \end{pmatrix} \tag{3.7}$$

$D(t)$ and $R(t)$ are respectively the nonlinear hydrodynamic damping force term and the nonlinear restoring force term. Unlike the terms in the linear part of the equation of motions which are well known, these nonlinear terms vary depending on specific

problems. As mentioned earlier, one of the advantages of the R-MISO method is the flexibility in the choice of nonlinear terms. The terms that are not relevant would be eventually sorted out at the end with coherence analysis. In the current study, the nonlinear hydrodynamic damping force $D(t)$ is chosen to be a quadratic relative vertical velocity term and the nonlinear restoring force $R(t)$ is chosen to be a quadratic displacement term. These terms correspond to the nonlinearities that are commonly observed for barge type vessels. But they can be replaced by other forms of nonlinear damping and stiffness if they reveal to be no relevant at the end of the R-MISO system identification procedure.

Since the barge is fixed at its center, only pitch and yaw rotations were observed. Thus the equation of motion is reduced to:

$$\begin{pmatrix} I_{yy}+a_{55} & 0 \\ 0 & I_{zz}+a_{66} \end{pmatrix}\begin{pmatrix} \ddot{\theta}(t) \\ \ddot{\psi}(t) \end{pmatrix}+\begin{pmatrix} c_{55} & 0 \\ 0 & c_{66} \end{pmatrix}\begin{pmatrix} \dot{\theta}(t) \\ \dot{\psi}(t) \end{pmatrix}+\begin{pmatrix} k_{55} & 0 \\ 0 & k_{66} \end{pmatrix}\begin{pmatrix} \theta(t) \\ \psi(t) \end{pmatrix}$$
$$+\begin{pmatrix} d_{55} & 0 \\ 0 & d_{66} \end{pmatrix}\begin{pmatrix} (\dot{z}(t)-\dot{w}(t))|\dot{z}(t)-\dot{w}(t)| \\ (\dot{z}(t)-\dot{w}(t))|\dot{z}(t)-\dot{w}(t)| \end{pmatrix}+\begin{pmatrix} r_{55} & 0 \\ 0 & r_{66} \end{pmatrix}\begin{pmatrix} \theta(t)|\theta(t)| \\ \psi(t)|\psi(t)| \end{pmatrix}=\begin{pmatrix} M_y \\ M_z \end{pmatrix} \tag{3.8}$$

Here, $\dot{w}(t)$ represents the vertical wave elevation velocity and is introduced in to each quadratic vertical relative velocity term. Note that the pitch and yaw motions are uncoupled in the present case due to the symmetry of the barge in both x-z and y-z planes.

3.3. System identification analysis and results

3.3.1 Methodology applied to the barge pitch

Consider the example of pitch which was observed to be the most prominent motion for the fixed barge. The equation of motion should be expressed in strict sense in an integro-differential form because the added mass and the damping coefficients are frequency dependent:

$$\begin{aligned}&\int_0^t \left(I_{yy}+a_{55}\right)(\tau)\ddot{\theta}(t-\tau)d\tau+\int_0^t c_{55}(\tau)\dot{\theta}(t-\tau)\,d\tau+k_{55}\theta(t)\\&+\int_0^t d_{55}(\tau)\left[\dot{z}(t-\tau)-\dot{w}(t-\tau)\right]\left|\dot{z}(t-\tau)-\dot{w}(t-\tau)\right|d\tau+\int_0^t r_{55}(\tau)\theta(t-\tau)\left|\theta(t-\tau)\right|\\&=M_y(t)\end{aligned} \tag{3.9}$$

The physical input and outputs are inversed to obtain respectively the mathematical inputs and output. After Fourier transform the equation of motion becomes:

$$A_1(f)X_1(f)+A_2(f)X_2(f)+A_3(f)X_3(f)=Y(f) \tag{3.10}$$

With X_i the Fourier transform of the mathematical inputs, Y the Fourier transform of the output and A_i the transfer functions relating each input to the output.

$$A_1(f)=k_{55}+j(2\pi f)c_{55}(f)-(2\pi f)^2\left(I_{yy}+a_{55}\right)(f) \tag{3.11}$$

$$A_2(f)=d_{55} \tag{3.12}$$

$$A_3(f)=r_{55} \tag{3.13}$$

$$X_1(f) = \text{Fourier transform of } \theta(t) \tag{3.14}$$

$$X_2(f) = \text{Fourier transform of } \left(\dot{z}(t) - \dot{w}(t)\right)\left|\dot{z}(t) - \dot{w}(t)\right| \tag{3.15}$$

$$X_3(f) = \text{Fourier transform of } \theta(t)\left|\theta(t)\right| \tag{3.16}$$

$$Y(f) = \text{Fourier transform of } M_y \tag{3.17}$$

Once the transfer functions A_i are found, it will be possible to identify the parameters in the following way:

$$c_{55}(f) = \frac{\mathrm{Im}\left(A_1(f)\right)}{2\pi f} \tag{3.18}$$

$$\left(I_{aa} + a_{55}\right)(f) = \frac{k_{55} - \mathrm{Re}\left(A_1(f)\right)}{\left(2\pi f\right)^2} \tag{3.19}$$

$$d_{55} = \mathrm{Re}\left(A_2\right) \tag{3.20}$$

$$r_{55} = \mathrm{Re}\left(A_3\right) \tag{3.21}$$

The linear stiffness k_{55} is not frequency dependant because it reflects hydrostatic effects. It is a constant whose value was estimated directly using the following equation (Faltinsen, 1990):

$$k_{55} = \rho g V\left(z_B - z_G\right) + \rho g \iint_{A_{WP}} x^2 ds \tag{3.22}$$

With

A_{WP} = waterplane area

V = displaced volume of water

z_B = z-coordinate of the center of buoyancy

z_G = z-coordinate of the center of gravity

ρ = density of seawater

The center of buoyancy is simply the center of the displaced volume, whereas the center of gravity is approximated at 10m from the keel based on available information. The moment of inertia about y-axis $\iint_{A_{WP}} x^2 ds$ is that of a $160\text{m} \times 60\text{m}$ rectangle, x-axis being the longitudinal axis. It is observed that the second term at the right-hand side of the equation 3.22, which contains $\iint_{A_{WP}} x^2 ds$, is the dominant contributor due to the large waterplane area of the barge. Thus, it is expected that the calculated linear stiffness k_{55} remains quite accurate despite the use of an approximate value for the center of gravity. The detailed calculation of the linear stiffness coefficient k_{55} is discussed in Appendix C. It is theoretically possible to identify k_{55} directly using the system identification method, but one would have encountered the practical problem of partitioning the linear stiffness and the added mass which are both contained in the real part of the transfer function A_1.

It was mentioned in section 3.1 that the original inputs need to be conditioned to become uncorrelated for the R-MISO procedure. The variables $\gamma_{u_1 y}{}^2$, $\gamma_{u_2 y}{}^2$, $\gamma_{u_3 y}{}^2$ are the ordinary coherence functions between each uncorrelated input and the output, they represent the proportion of the output spectrum that is due to each uncorrelated input passing through the corresponding linear system:

$$\gamma_{u_1 y}{}^2 = \frac{\left|S_{u_1 y}\right|^2}{S_{u_1 u_1} S_{yy}} = \frac{\left|S_{1y}\right|^2}{S_{11} S_{yy}} \tag{3.23}$$

$$\gamma_{u_2 y}{}^2 = \frac{\left|S_{u_2 y}\right|^2}{S_{u_2 u_2} S_{yy}} = \frac{\left|S_{2y\cdot 1}\right|^2}{S_{22\cdot 1} S_{yy}} \tag{3.24}$$

$$\gamma_{u_3 y}{}^2 = \frac{\left|S_{u_3 y}\right|^2}{S_{u_3 u_3} S_{yy}} = \frac{\left|S_{3y\cdot 1,2}\right|^2}{S_{33\cdot 1,2} S_{yy}} \tag{3.25}$$

u_i designates the conditioned uncorrelated inputs. Similarly $S_{ij\cdot k}$ is the cross spectral density between inputs x_i and x_j with the influence of x_k removed. The subscript "y" designates the output pitch moment.

The successive summation of these values is defined as the cumulative coherence function and it is used to indicate the overall goodness-of-fit of the model. When the coherence function is close to unity, it is an indication that the model provides a good fit to the data. The extraneous noise spectrum is defined as:

$$\begin{aligned} S_{nn}(f) &= \left[1 - \left(\text{last cumulative coherence function}\right)\right] S_{yy} \\ &= \left[1 - \left(\gamma_{u_1 y}{}^2 + \gamma_{u_2 y}{}^2 + \gamma_{u_3 y}{}^2\right)\right] S_{yy} \end{aligned} \tag{3.26}$$

Often the ratio $\frac{S_{nn}}{S_{yy}}$ is used to represent the goodness-of-fit of the model, it is satisfactory when this ratio is close to 0.

3.3.2 Results and discussion

Figure 3.1 shows the spectral densities of the pitch motion which is a mathematical input in the present R-MISO system, and the pitch moment which is the mathematical output. It can be observed that most of the spectral energies are contained within the frequency range of [0.05Hz, 0.15 Hz] which is the frequency range of interest of the present problem. But this frequency range will be extended to [0.05Hz, 0.25 Hz] to be consistent with the one used later in the study of the two body system. A strong linear relationship can be observed between the pitch and the pitch moment due to the similarity of their spectral densities. This linearity is confirmed by the probability distributions of the input pitch motion and the output pitch moment in Figure 3.2 which both follow the Gaussian distribution.

The cumulative coherence functions are presented in Figure 3.3. The first cumulative coherence function represents the contribution of the pitch motion which is the first input time series, to the output pitch moment. The second and the third ones correspond respectively to when the contribution of the relative vertical velocity term and then that of the quadratic pitch are added. A very high final coherence can be observed in nearly the entire frequency range of interest, the model can thereby be considered satisfactory. Usually when one single input contributes more than 80% of coherence, this is a strong indication of a linear relation between this input and the output. This is the case of the input pitch motion. The second input, that is the relative vertical velocity, provides very slight improvement at some frequencies, especially around 0.12 Hz. The quadratic pitch term which is the third input does not seem to provide any noticeable additional coherence to the system. These individual contributions can be better visualized with the partial coherence functions plotted in Figure 3.5. The extraneous noise / output ratio illustrated in Figure 3.4 gives an alternative view of the goodness-of-fit of the model.

(a)

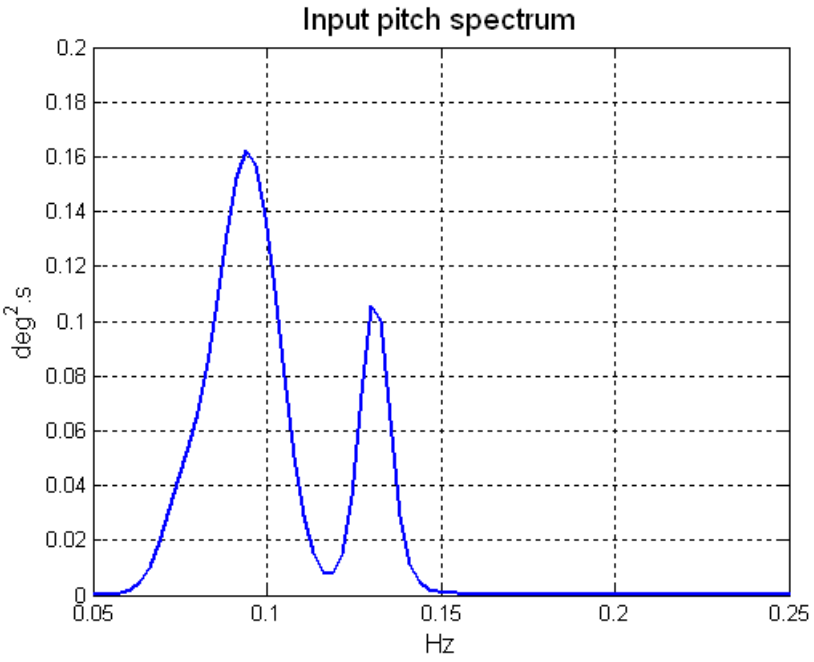

(b)

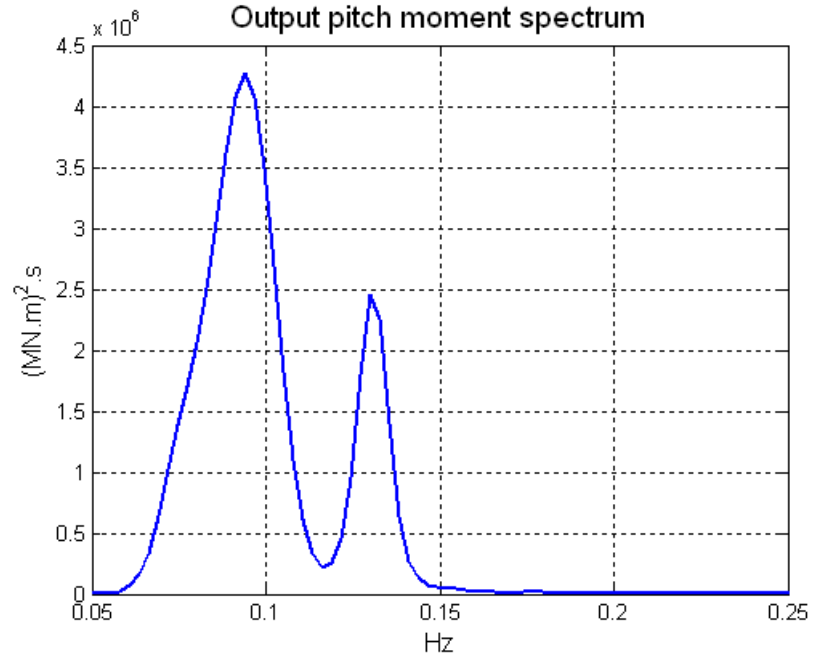

Figure 3.1 Spectral density of (a) the input pitch, (b) the output pitch moment.

(a)

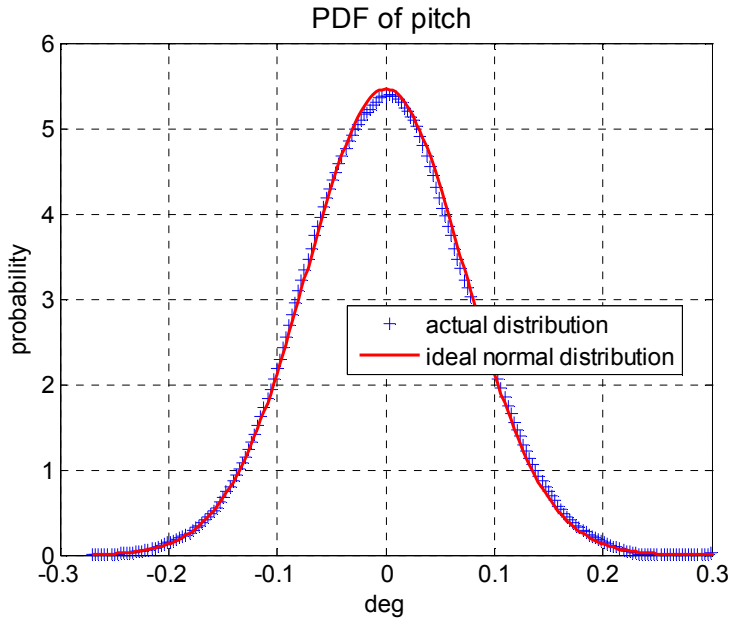

(b)

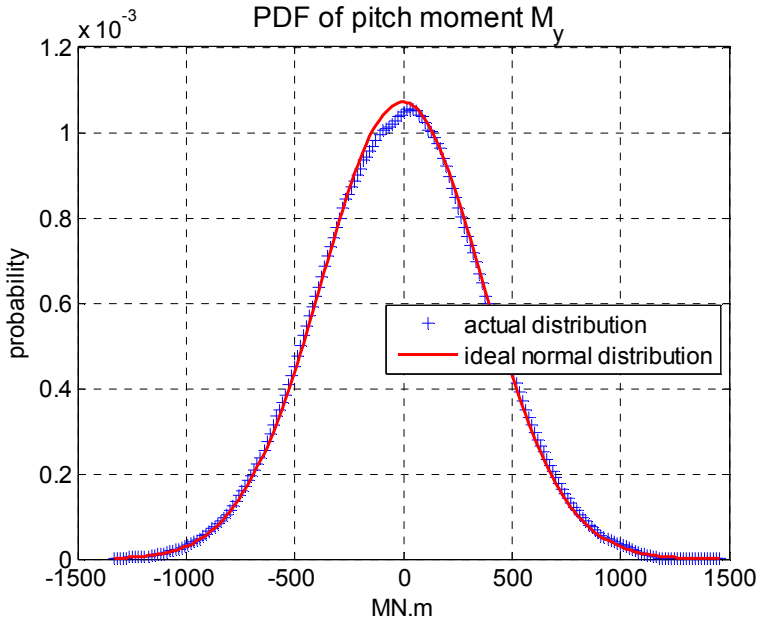

Figure 3.2 Comparison between the actual probability density function and the ideal normally distributed function with the same mean and variance for (a) the pitch motion, (b) the pitch moment.

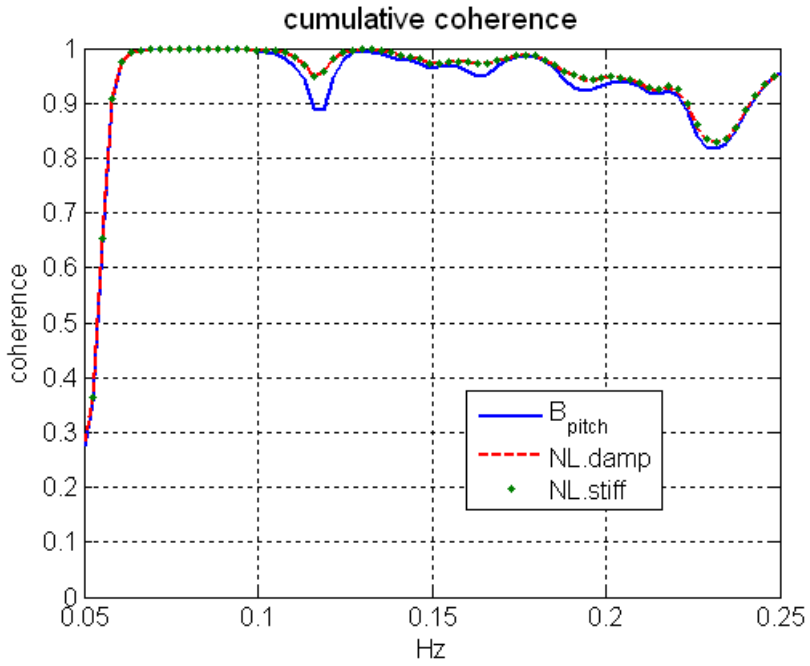

Figure 3.3 Cumulative coherence functions.

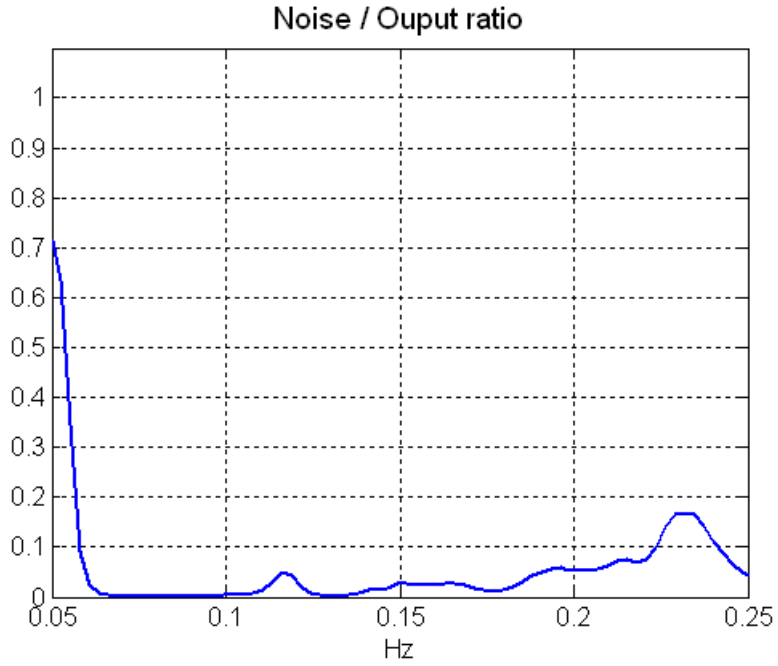

Figure 3.4 Extraneous noise / output ratio.

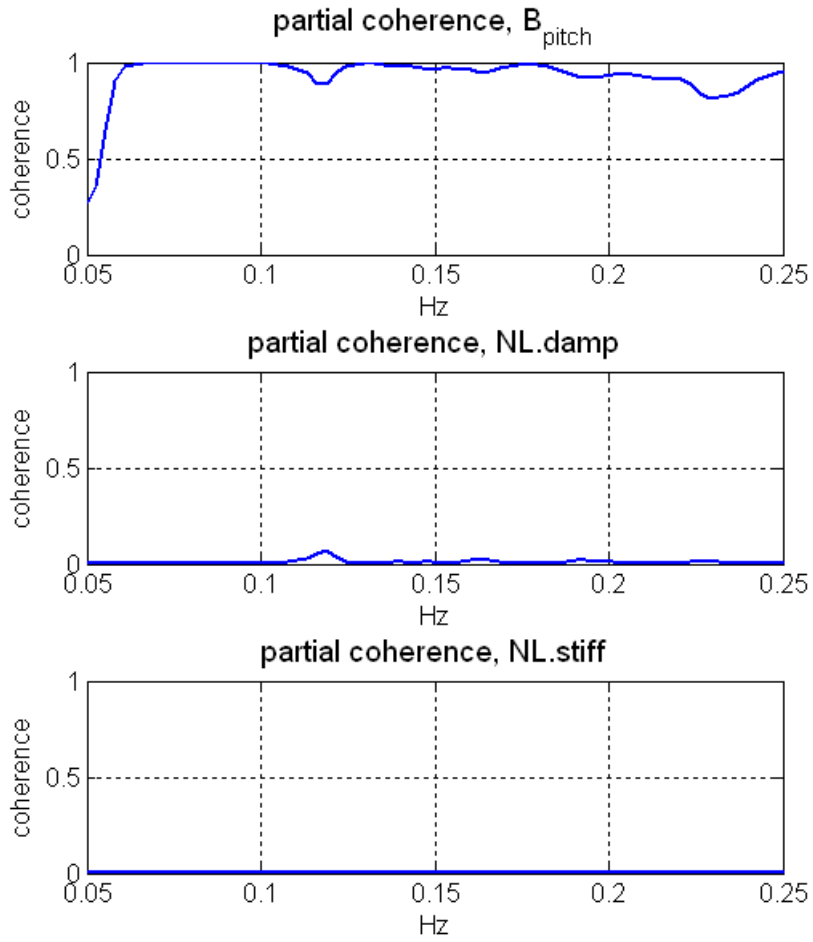

Figure 3.5 Partial coherence functions.

Since it has no contribution, the nonlinear stiffness term under the form of quadratic pitch can be neglected in the present system. This ability of using arbitrary nonlinear terms and sorting out the non-relevant ones at the end constitutes an important advantage that the R-MISO method presents. Before testing other forms of nonlinear terms in an attempt to improve the total goodness-of-fit of the model, it is important to examine the behavior of the system at the frequencies where the coherence is relatively less satisfactory. Lower coherence occurs notably at the two extremities of the frequency range of interest where the coherence decreases rapidly. This is due to the low energy concentration of the input and output spectra at these frequencies.

To explain the reason why the coherence is usually low at the frequencies where the input and output data have low energy concentrations, recall that the partial coherence between the input barge pitch and the output barge pitch moment is defined as (same as Equation 3.23):

$$\gamma_{u_1 y}{}^2 = \frac{\left|S_{u_1 y}\right|^2}{S_{u_1 u_1} S_{yy}} = \frac{\left|S_{1y}\right|^2}{S_{11} S_{yy}} \tag{3.26}$$

It can be alternatively viewed as the ratio between the ideal model spectrum and the estimated model spectrum. Figure 3.6a shows the absolute difference $S_{11}S_{yy} - \left|S_{1y}\right|^2$ near the frequency 0.23Hz where the energy concentration of the input and output data is low and where a sudden dip is presented in the coherence function. It can be seen that the difference between the ideal model and the estimated model is actually smaller around 0.23Hz than other frequencies. One would first expect the goodness-of-fit to be higher for this frequency. However the opposite situation occurs as shown in Figure 3.6b. This demonstrates that when the energy concentration is small, even a small noise can be proportionally important compared to the low energy output.

(a)

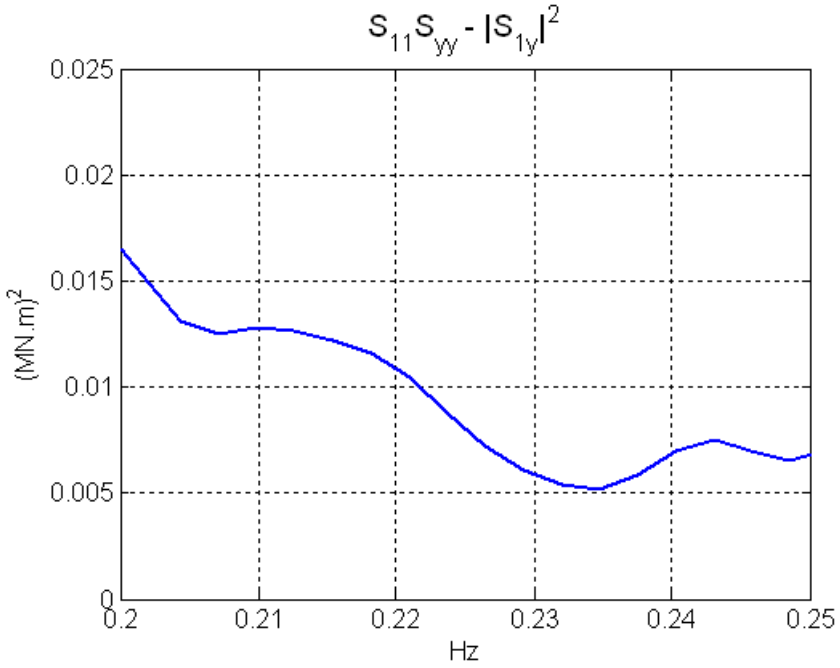

(b)

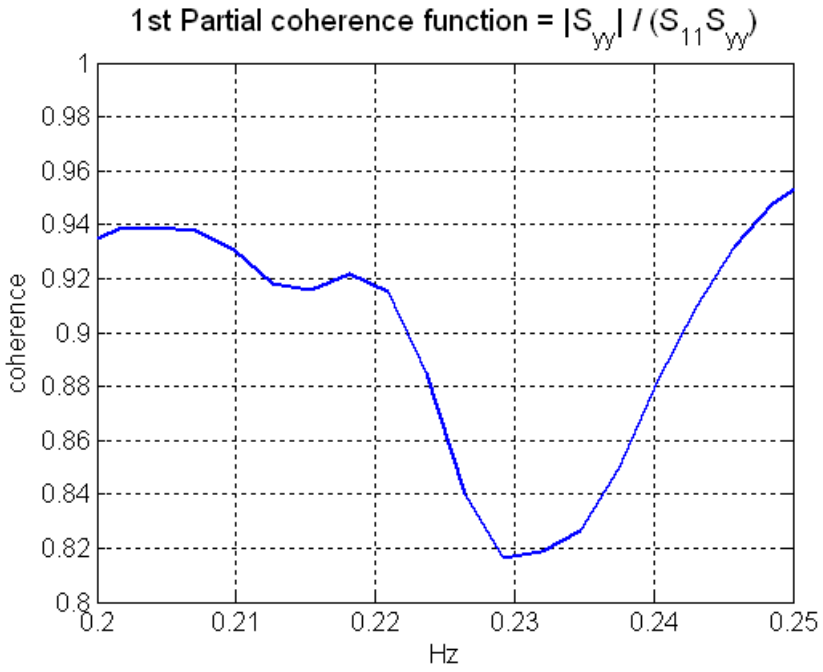

Figure 3.6 (a) The difference $S_{11}S_{yy} - \left|S_{1y}\right|^2$, and (b) the ratio $\left|S_{1y}\right|^2 / S_{11}S_{yy}$, around 0.23 Hz where the coherence is low.

Another visible dip in coherence is observed at around 0.12 Hz which corresponds in fact to the pitch natural frequency measured during decay tests. It was documented in literature that such decrease of coherence exists near resonance (Selvam and Bhattacharyya, 2006). In addition, being forced to move in wave frequencies, the input pitch and the output pitch moment have a quite low energy concentration at the pitch natural frequency which only makes an accurate estimation around this frequency more difficult.

Since the quadratic pitch term does not contribute much to the overall goodness-of-fit of the model, different other forms of nonlinear stiffness terms were tested. This includes mainly the use of other vessel motion vectors that have a higher energy concentration around 0.12Hz. However no visible improvement was observed, it was thus decided to discard the nonlinear stiffness term from the equation of motion. This simplification does not change the cumulative coherence calculated earlier and is justified since there is no mooring or connection system that creates nonlinearities in the present case. The final identification of the hydrodynamic parameters is based on the simplified equation of motion.

The R-MISO analysis computes the transfer functions and the hydrodynamic parameters. Figure 3.7 shows the magnitude and the phase of the first transfer function relating the mathematical barge pitch input to the mathematical barge pitch moment output. From the equation of this transfer function, the constant linear stiffness coefficients can be estimated:

$$A_1(f) = k_{55} + j(2\pi f)c_{55}(f) - (2\pi f)^2 \left(I_{yy} + a_{55}\right)(f) \tag{3.27}$$

$$A_1(0) = k_{55} \tag{3.28}$$

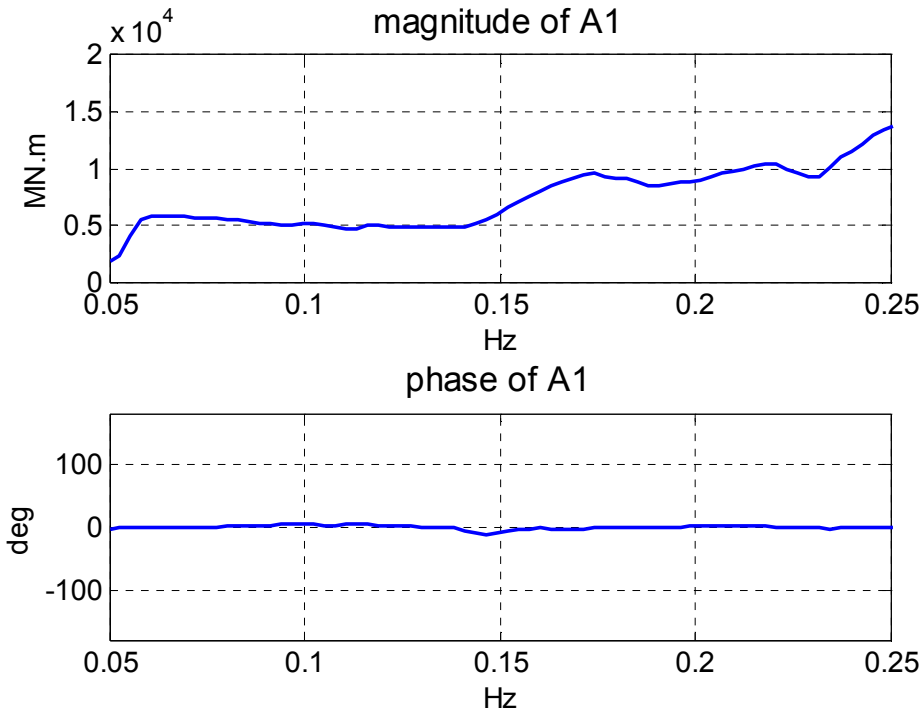

Figure 3.7 Magnitude and phase spectra of the transfer function A1.

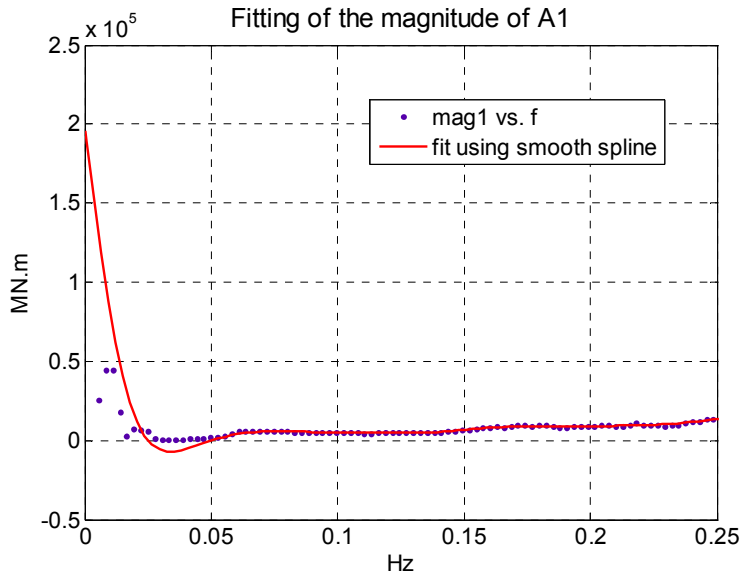

Figure 3.8 Fitting of the magnitude of A1 near the zero frequency.

However the behavior of the transfer function A_1 is not very smooth, thus the Matlab curve fitting toolbox was used to smooth and fit the curve and to find the value of the transfer function at the zero frequency. The fitting curve is plotted in Figure 3.8, it gives 195,800 MN.m as the value for the linear stiffness k_{55}, which is not very different from the 202,700 MN.m estimated in Appendix C. Since the selection of the curve fitting parameter can be somehow subjective, it is decided to use it as a verification tool rather as a direct estimation of the linear stiffness.

The virtual mass of the system is plotted in Figure 3.9, it decreases with the increasing frequencies. It would have been more informative if the added mass can be separated from the mass moment of inertia I_{yy}. But the calculation of I_{yy}, which should not be confused with the area moment of inertia used for the computation of the linear stiffness, cannot be performed without an accurate knowledge of the mass distribution of the barge especially when additional weights were added during the tests.

The linear damping has low amplitude as shown in Figure 3.10. Actually the phase spectrum of the transfer function A1 in Figure 3.7 has also very small values. Since the damping is associated with the velocity, a phase shift is expected. The zero phase shift may indicates a very small damping in the system. To prove that, the fraction between the damping and the critical damping is calculated:

$$\text{Fraction between damping and critical damping} = \frac{c_{55}\left(\omega_{n,5}\right)}{2\left(I_{55} + a_{55}\left(\omega_{n,5}\right)\right)\omega_{n,5}} \tag{3.29}$$

With $\omega_{n,5}$ the angular natural frequency of the pitch motion.

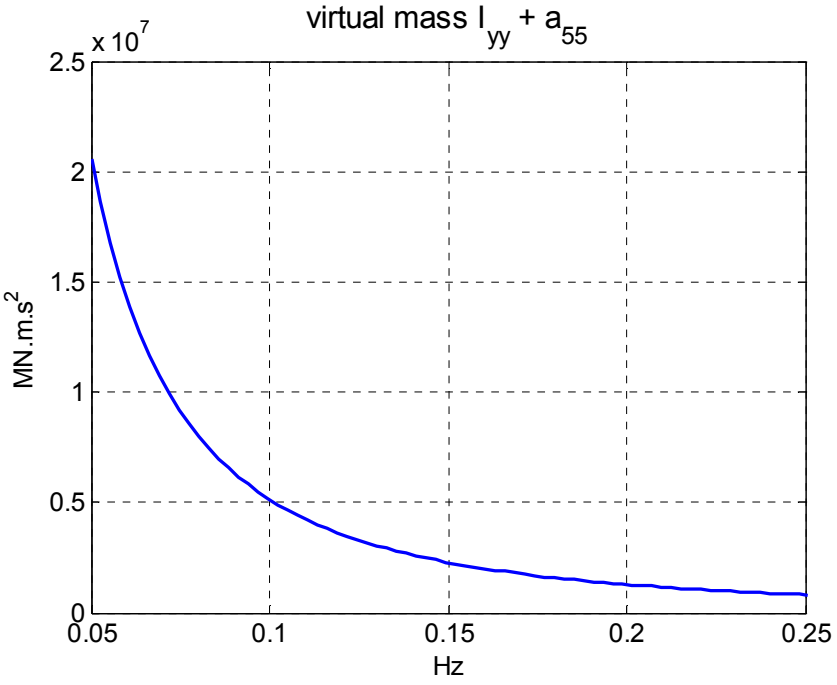

Figure 3.9 Virtual mass coefficient $I_{yy} + a_{55}$

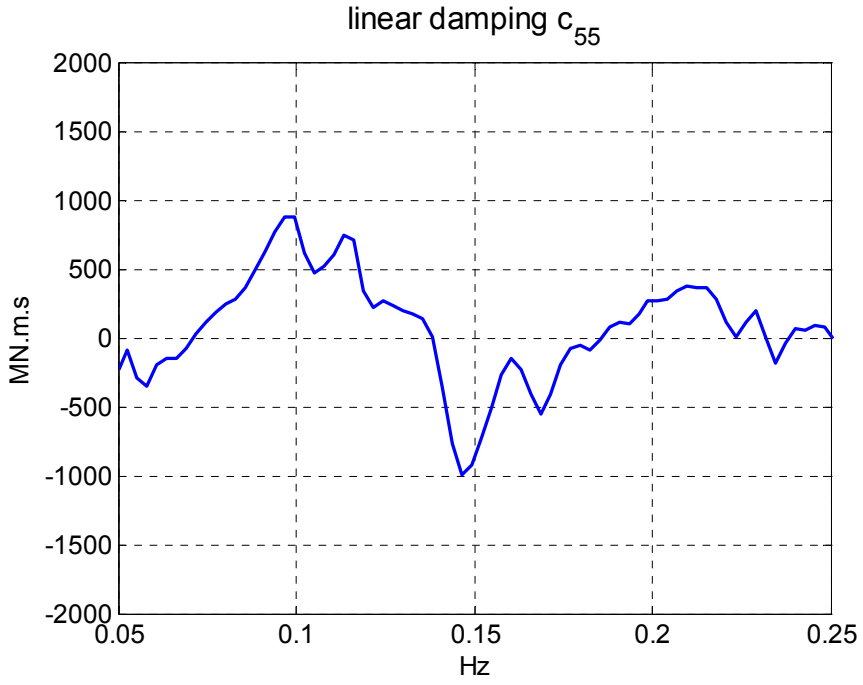

Figure 3.10 Linear damping coefficient c_{55}

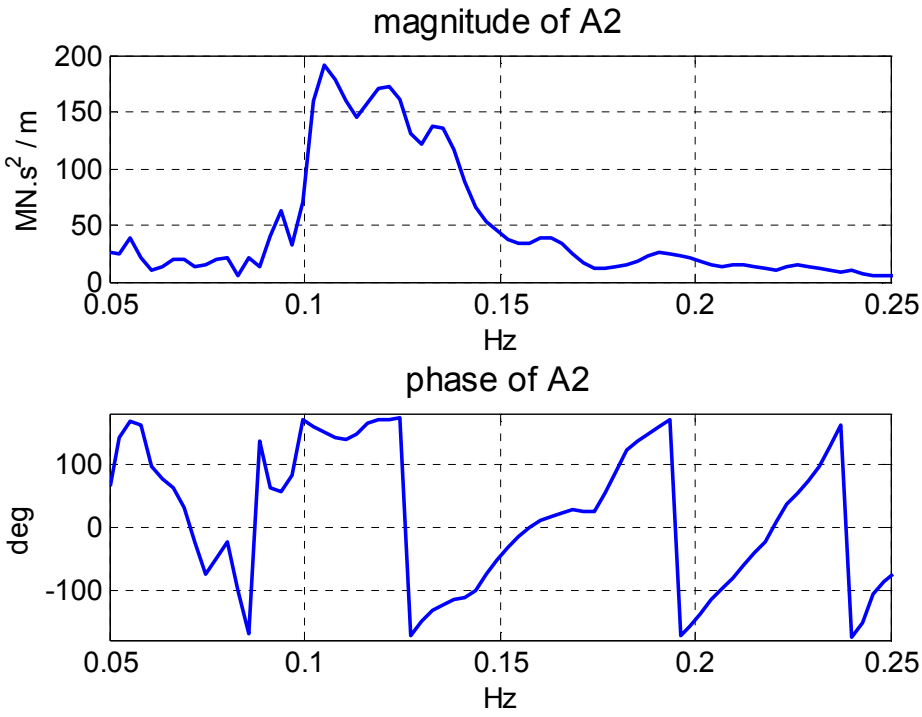

Figure 3.11 Magnitude and phase spectra of the transfer function A2.

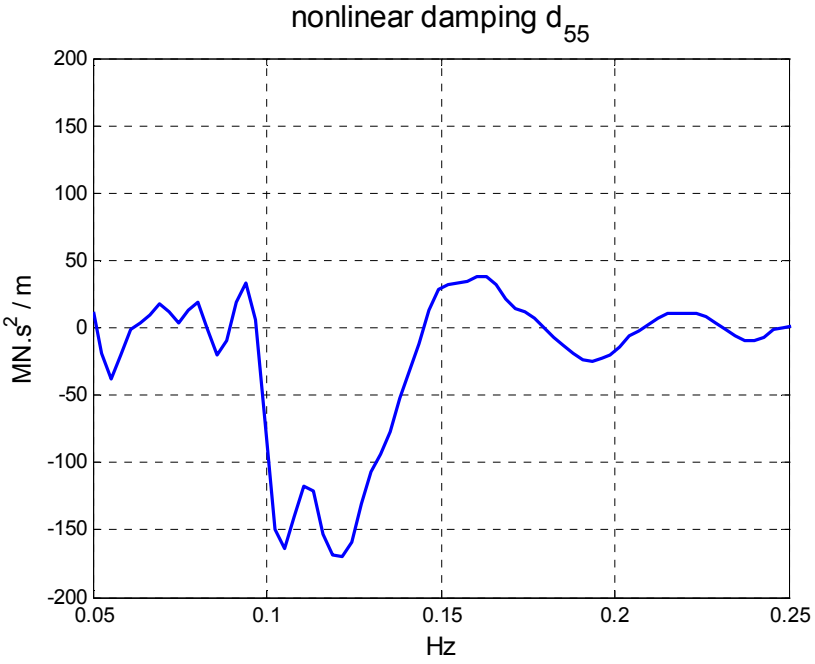

Figure 3.12 Nonlinear damping coefficient d_{55}

A result nearly equal to 0% shows that there is almost no damping force observed. This lack of damping may be due to the fact that the barge is fixed at its center and can only undergo small pitch motions. Some negative damping is observed near 0.15Hz, it can be also caused by the fixation of the barge. Toward the higher frequencies, the beginning of a convergence of damping toward 0 can be observed. Indeed, in high frequencies the damping should be close to 0.

Figures 3.11 and 3.12 shows respectively the transfer function A_2 and the nonlinear damping coefficients derived from this transfer function. A possible explanation of the negative values of the nonlinear damping coefficients is again the fixation of the barge. A convergence to 0 can be also observed at high frequencies.

3.3.3. Validation of the results

It is known that

$$\omega_{n,5} = \left(\frac{k_{55}}{I_{55} + a_{55}\left(\omega_{n,5}\right)} \right)^{0.5} \tag{3.30}$$

The linear stiffness coefficient was estimated in the earlier section to be 202,700 MN.m. Reading from Figure 3.9, mass term is equal to 356,000 MN.m.s² at the pitch natural period which is 0.12 Hz (0.754 rad/s). The term at the right-hand side of the Equation 3.30 can be calculated and it is equal to 0.755 rad/s, which is very close to the term at the left-hand side of the equation (0.754 rad/s). This shows the consistency between the estimated value (linear stiffness coefficient), the identified value (added mass) and the experimentally measured value (pitch natural period).

The measured mathematical inputs (barge pitch and the quadratic barge pitch) and the identified parameters are substituted back into Equation 3.9, with the exception of the nonlinear stiffness term which has been neglected. The mathematical output pitch moment can thus be reconstituted and it is compared with the measured values in Figure 3.13. The simulated data has a periodicity that marches well with the measured data; however its amplitude tends to be somehow smaller. Besides the imperfection of the model, some inaccuracies could have been introduced during the derivation of the time series for the calculation of the velocity and acceleration data.

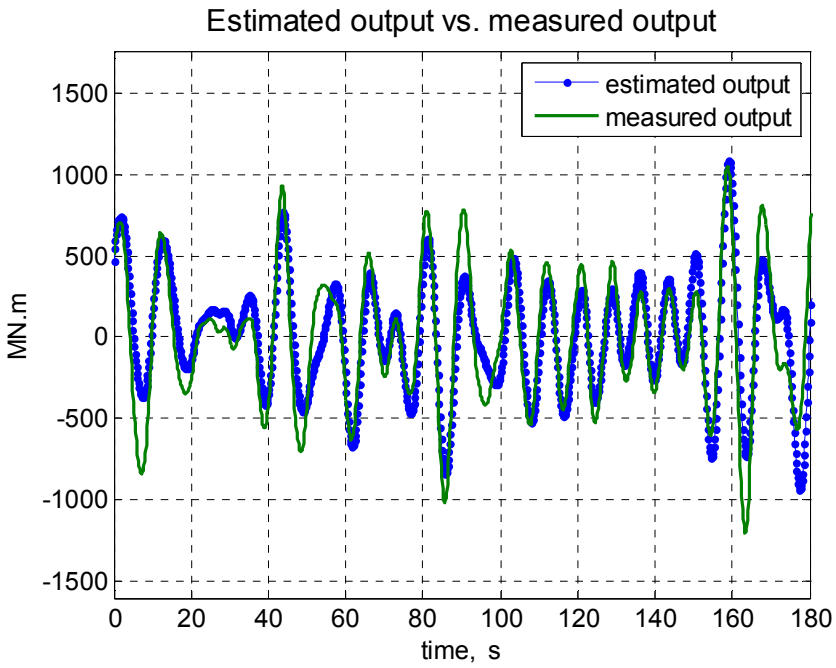

Figure 3.13 Comparison between the reconstituted barge pitch moment and the measured barge pitch moment.

4. IDENTIFICATION OF THE SYSTEM PARAMETERS OF A COUPLED BARGE AND SHIP SYSTEM

Based upon the formulation and numerical results shown in the previous section, the R-MISO method is an efficient and robust methodology for the identification of the system parameters of a single body. In this section the R-MISO method is extended to analyze a two-body system. Several issues specific to multi-body problems in general need to be addressed, including how to differentiate the importance of the significantly increasing number of variables, and the interpretation of the results. These issues are addressed through the problem formulation and of the coupled barge and ship system first described in Section 2.

4.1 Equation of motion

4.1.1 General form of the equation of motion of a two body system

The equations of motion of a coupled system needs to account for the coupling due to hydrodynamic forces and those due to mechanical connections such as mooring lines and fenders. Thus, the equations of motion for the barge and ship system presented in Section 2 can be expressed in the following compact matrix form:

$$\begin{aligned}
&\begin{pmatrix} M^{BB}+a^{BB} & M^{BS}+a^{BS} \\ M^{SB}+a^{SB} & M^{SS}+a^{SS} \end{pmatrix}\begin{pmatrix} \ddot{q}^{B}(t) \\ \ddot{q}^{S}(t) \end{pmatrix}+\begin{pmatrix} c^{BB} & c^{BS} \\ c^{SB} & c^{SS} \end{pmatrix}\begin{pmatrix} \dot{q}^{B}(t) \\ \dot{q}^{S}(t) \end{pmatrix} \\
&+\begin{pmatrix} k^{BB}+k_l^{BB}+k_f^{BB} & k^{BS}+k_l^{BS}+k_f^{BS} \\ k^{SB}+k_l^{SB}+k_f^{SB} & k^{SS}+k_l^{SS}+k_f^{SS} \end{pmatrix}\begin{pmatrix} q^{B}(t) \\ q^{S}(t) \end{pmatrix} \\
&+\begin{pmatrix} d^{B} & 0 \\ 0 & d^{S} \end{pmatrix}\begin{pmatrix} D^{B}(t) \\ D^{S}(t) \end{pmatrix}+\begin{pmatrix} r^{B} & 0 \\ 0 & r^{S} \end{pmatrix}\begin{pmatrix} R^{B}(t) \\ R^{S}(t) \end{pmatrix}=\begin{pmatrix} F_w^{\ B} \\ F_w^{\ S} \end{pmatrix}
\end{aligned} \tag{4.1}$$

where, M is the vessel mass, a is the hydrodynamic added-mass, c is the linear damping, k is the linear stiffness, k_l is the linearized mooring line stiffness, k_f is the linearized fender stiffness, d is the nonlinear damping, r is the nonlinear stiffness, F_w is the wave induced excitation, and q contains the vessel motions. Further, the superscript "B" indicates values related to the barge and the superscript "S" indicates values related to the ship. The major difference between Equation 4.1 and Equation 3.1 for single body is that this formulation includes the various cross-coupling terms. Since the mooring line forces and fender forces were measured during the model tests, the matrix equations can re-written as:

$$\begin{pmatrix} M^{BB}+a^{BB} & a^{BS} \\ a^{SB} & M^{SS}+a^{SS} \end{pmatrix}\begin{pmatrix} \ddot{q}^{B}(t) \\ \ddot{q}^{S}(t) \end{pmatrix}+\begin{pmatrix} c^{BB} & c^{BS} \\ c^{SB} & c^{SS} \end{pmatrix}\begin{pmatrix} \dot{q}^{B}(t) \\ \dot{q}^{S}(t) \end{pmatrix}+\begin{pmatrix} k^{BB} & k^{BS} \\ k^{SB} & k^{SS} \end{pmatrix}\begin{pmatrix} q^{B}(t) \\ q^{S}(t) \end{pmatrix}$$
$$+\begin{pmatrix} d^{B} & 0 \\ 0 & d^{S} \end{pmatrix}\begin{pmatrix} D^{B}(t) \\ D^{S}(t) \end{pmatrix}+\begin{pmatrix} r^{B} & 0 \\ 0 & r^{S} \end{pmatrix}\begin{pmatrix} R^{B}(t) \\ R^{S}(t) \end{pmatrix}=\begin{pmatrix} F_w{}^{B} \\ F_w{}^{S} \end{pmatrix}-\begin{pmatrix} F_f{}^{B} \\ F_f{}^{S} \end{pmatrix}-\begin{pmatrix} F_l^{B} \\ F_l^{S} \end{pmatrix} \tag{4.2}$$

where, F_l are the measured mooring line contributions, F_f are the measured fender forces, and F_w contains the measured wave induced force and moment contributions. Since the ship is moored to a relatively rigid barge, it is necessary to decompose the mooring line and fender forces in order to obtain the normal components as described in Appendix D.

The six degrees of freedom of the barge will be indicated using the subscripts $i = 1, 2, \ldots 6$, which correspond to the barge surge, sway, heave, roll, pitch and yaw motions. The six degrees of freedom of the ship will be indicated by the subscripts $i = 7, 8, \ldots 12$, corresponding to the ship surge, sway, heave, roll, pitch and yaw motions. The matrices related to the barge are identical to those presented earlier in Section 3. As in the previous section, due to the nature of the barge restraint only the barge pitch and yaw motions are retained in the formulation. Although the barge yaw motion is quite

small when compared to that of the ship motions, it is kept to illustrate the cross-coupling between the two vessels.

The matrixes of the hydrodynamic coefficients related to the ship are complicated due to the fact that the ship has only one plane of symmetry, which is the x-z plane. This is reflected in the matrix equations that follow.

$$\mathrm{M}^{SS} = \text{mass matrix} = \begin{pmatrix} m_S & 0 & 0 & 0 & m_S \cdot z_{G_S} & 0 \\ 0 & m_S & 0 & -m_S \cdot z_{G_S} & 0 & 0 \\ 0 & 0 & m_S & 0 & 0 & 0 \\ 0 & -m_S \cdot z_{G_S} & 0 & I_{xx_S} & 0 & -I_{xz_S} \\ m_S \cdot z_{G_S} & 0 & 0 & 0 & I_{yy_S} & 0 \\ 0 & 0 & 0 & -I_{xz_S} & 0 & I_{zz_S} \end{pmatrix} \tag{4.3}$$

Note that unlike the barge configuration used in this study, the center of gravity varies with the onboard shipload configurations and is not a constant. Thus, it is preferable to select a point of reference point that would remain constant regardless of the loading condition.

$$\mathrm{a}^{SS} = \text{added-mass matrix} = \begin{pmatrix} a_{7,7} & 0 & a_{7,9} & 0 & a_{7,11} & 0 \\ 0 & a_{8,8} & 0 & a_{8,10} & 0 & a_{8,12} \\ a_{9,7} & 0 & a_{9,9} & 0 & a_{9,11} & 0 \\ 0 & a_{10,8} & 0 & a_{10,10} & 0 & a_{10,12} \\ a_{11,7} & 0 & a_{11,9} & 0 & a_{11,11} & 0 \\ 0 & a_{12,8} & 0 & a_{12,10} & 0 & a_{12,12} \end{pmatrix} \tag{4.4}$$

The linear damping matrix c^{SS} has the same structure as the added mass matrix. Both the added mass matrix and the linear damping matrix are assumed to be symmetric because there is no current and the ship does not have any forward speed.

The linear stiffness matrix k^{SS} is not frequency dependent and consequently the linear stiffness coefficients are reflective of only the hydrostatic effects. Thus, they can be estimated based upon the submerged volume as detailed in Appendix C.

$$k^{SS} = \text{linear stiffness matrix} = \begin{pmatrix} 0 & 0 & 0 & 0 & 0 & 0 \\ 0 & 0 & 0 & 0 & 0 & 0 \\ 0 & 0 & k_{9,9} & 0 & k_{9,11} & 0 \\ 0 & 0 & 0 & k_{10,10} & 0 & 0 \\ 0 & 0 & k_{11,9} & 0 & k_{11,11} & 0 \\ 0 & 0 & 0 & 0 & 0 & 0 \end{pmatrix} \tag{4.5}$$

The nonlinear damping and stiffness matrices d^{SS} and r^{SS} were developed by assuming that the second order terms are negligible, and thus can be expressed as:

$$\mathrm{d}^{SS} = \text{nonlinear damping matrix} = \begin{pmatrix} d_{7,7} & 0 & 0 & 0 & 0 & 0 \\ 0 & d_{8,8} & 0 & 0 & 0 & 0 \\ 0 & 0 & d_{9,9} & 0 & 0 & 0 \\ 0 & 0 & 0 & d_{10,10} & 0 & 0 \\ 0 & 0 & 0 & 0 & d_{11,11} & 0 \\ 0 & 0 & 0 & 0 & 0 & d_{12,12} \end{pmatrix} \tag{4.6}$$

$$\mathrm{r}^{SS} = \text{nonlinear stiffness matrix} = \begin{pmatrix} r_{7,7} & 0 & 0 & 0 & 0 & 0 \\ 0 & r_{8,8} & 0 & 0 & 0 & 0 \\ 0 & 0 & r_{9,9} & 0 & 0 & 0 \\ 0 & 0 & 0 & r_{10,10} & 0 & 0 \\ 0 & 0 & 0 & 0 & r_{11,11} & 0 \\ 0 & 0 & 0 & 0 & 0 & r_{12,12} \end{pmatrix} \tag{4.7}$$

The cross-coupling of the stiffness between the barge and ship, k^{BS} and k^{SB}, can be neglected based on the reasoning that the buoyancy of one vessel does not change because of the presence of another vessel.

The cross-coupling matrices of the hydrodynamic added-mass a^{BS}, c^{BS} have the similar forms. For instance the cross-coupling added mass coefficients between the two vessels are:

$$a^{BS} = \begin{pmatrix} a^{5,7} & a^{5,8} & a^{5,9} & a^{5,10} & a^{5,11} & a^{5,12} \\ a^{6,7} & a^{6,8} & a^{6,9} & a^{6,10} & a^{6,11} & a^{6,12} \end{pmatrix} \tag{4.8}$$

And the cross-coupling matrixes a^{SB} and c^{SB} have the following form:

$$a^{BS} = \begin{pmatrix} a^{7,5} & a^{7,6} \\ a^{8,5} & a^{8,6} \\ a^{9,5} & a^{9,6} \\ a^{10,5} & a^{10,6} \\ a^{11,5} & a^{11,6} \\ a^{12,5} & a^{12,6} \end{pmatrix} \tag{4.9}$$

None of the elements are neglected directly based on the geometry because two vessels are attached via the mooring lines. However, one can simplify these matrixes by determining the significance of each terms based on degree of interaction between each pair of motions of the barge and ship. This is the subject of study in the following section.

4.1.2 Cross-coupling terms

Equations 4.2 – 4.9 show that when the barge pitch and yaw motions are considered along with the six translational and rotational motions of the ship, there can be up to 24 linear system parameters to be identified for each SDOF system. That is 192 linear system parameters for the whole system without simplification. Some of these terms can be neglected directly considering the vessel geometry, others are more case dependant especially in a two-body configuration where the cross-coupling between the certain vessel motions can be important. The cross-coupling terms between different vessels are sometime entirely neglected in studies of multi-body systems because of the complexity they bring. In the present investigation they are selectively preserved for the equations of motion to obtain a relatively accurate result while avoiding heavy computational load.

The selection of these terms needs to be based on the importance of their physical meaning. The energy related to the motion interaction is chosen to measure the relative importance of each term. In wave mechanics, the wave energy is often measured using power density spectrum which is proportional to the square of the wave height for each frequency. By analogy, cross power density spectrum S_{ij} can describe how the power, thereby the energy related to the motion interaction is distributed. The total power, also called the 0^{th} moment of the cross power density spectrum is obtained by integrating the spectrum over all the frequencies:

$$0^{th} \text{ moment} = \text{area under the cross density spectrum} = \int_0^\infty S_{ij}(f)\,df \tag{4.10}$$

For i, j = 1, 2, …, 12.

In the present study, the integration is performed over the frequency range of interest which is [0.05Hz, 0.25Hz] as in the case of the single barge, because the energy is negligible outside of this range.

Figure 4.1 illustrates the example of the cross power density spectrum between the ship pitch and the barge pitch motions in head seas for the 80% filled case. The peak locates near the frequency corresponding to the input wave period; this shows that the interaction of these two motions provides most of the energy in wave frequencies. The integrated area of this case is, as will be seen later, relatively large. The cross-coupling between the barge pitch and ship pitch may thus be important and the corresponding hydrodynamic parameters $a_{5,11}$ and $c_{5,11}$ will be kept in the equations of motion for the system identification analysis later.

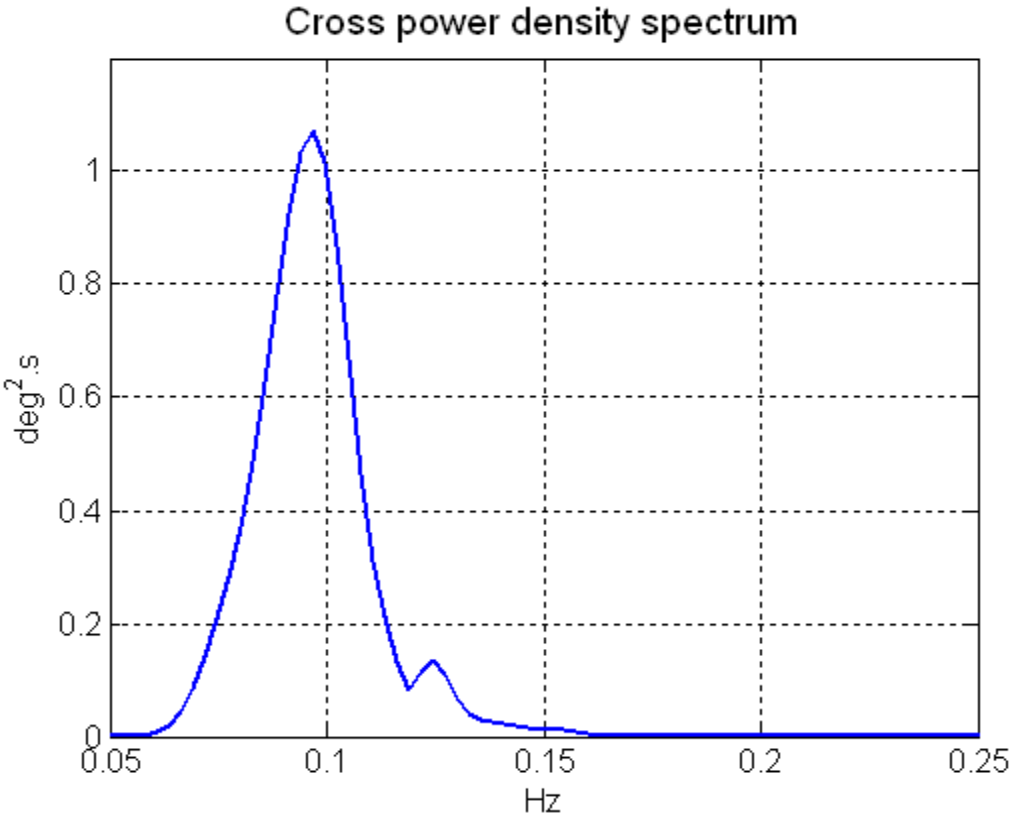

Figure 4.1 Cross power density spectrum of the barge pitch / ship pitch pair.

Before calculating the 0^{th} moment of the other motion pairs, the following assumptions are made: first, the diagonal terms in the coefficient matrix are systematically kept, it is thereby no need to calculate their 0^{th} moment to determine their importance. Secondly, the barge has two planes of symmetry and the ship has one plane of symmetry, the terms that can be neglected by geometry are discarded. And the final assumption is that the coefficient matrixes are symmetric.

Table 4.1 lists the values of the 0^{th} moment of all pairs of motion couplings that were not simplified with the previous assumptions. It can be observed that some pairs have consistently low energy concentration in all headings, such as the barge pitch / ship surge couple and the barge pitch / ship sway couple. All the pairs involving the barge yaw motion also have very low energy because of the low input provided by barge yaw, it confirms the earlier observation stating that the barge yaw motion is small and could have been neglected. For some pairs, the behavior can be very different depending on the heading condition. For instance the ship sway and ship roll pair, the energy is the largest for the 45° heading which is the configuration where the ship is exposed to the incident wave, and it is the smallest for the -45° heading where the ship is shielded. This difference brings to believe that the hydrodynamic parameters can be different too depending on the heading condition for two-body systems unlike the single body systems whose hydrodynamic parameters are solely dependent of the form of the submerged area. This discussion is further developed in later sections. Note that the results involving the ship surge motion are not reliable for the 0° heading case because of the mediocre quality of the measured surge time series for this configuration.

Cross power density spectrum *	80%, 0	80%, 45	80%, -45
B pitch / S surge, $S_{5,7}$ (deg.m.s)	*0.06***	*1.67*	*0.05*
B pitch / S sway, $S_{5,8}$ (deg.m.s)	*2.16*	*2.22*	*1.25*
B pitch / S heave, $S_{5,9}$ (deg.m.s)	5.38	7.12	4.87
B yaw / S surge, $S_{6,7}$ (deg.m.s)	*0.02*	*0.50*	*0.02*
B yaw / S sway, $S_{6,8}$ (deg.m.s)	*0.51*	*0.66*	*0.63*
B yaw / S heave, $S_{6,9}$ (deg.m.s)	*1.39*	*1.82*	*2.12*
S surge / S pitch, $S_{7,11}$ (deg.m.s)	*0.26*	16.76	*0.24*
S sway / S roll, $S_{8,10}$ (deg.m.s)	13.16	28.72	5.96
S sway / S yaw, $S_{8,12}$ (deg.m.s)	5.16	7.10	*1.57*
S heave / S pitch, $S_{9,11}$ (deg.m.s)	22.15	57.28	17.32
B yaw / S roll, $S_{6,10}$ (deg².s)	*1.75*	*4.89*	*3.60*
B yaw / S pitch, $S_{6,11}$ (deg².s)	*2.76*	*3.20*	*4.84*
B yaw / S yaw, $S_{6,12}$ (deg².s)	*0.61*	*1.05*	*1.62*
S roll / S yaw, $S_{10,12}$ (deg².s)	15.97	56.60	8.67
B pitch / S roll, $S_{5,10}$ (deg².s)	6.26	25.37	9.18
B pitch / S pitch, $S_{5,11}$ (deg².s)	10.49	15.82	16.35
B pitch / S yaw, $S_{5,12}$ (deg².s)	*2.52*	*4.68*	*4.09*
S surge / S heave, $S_{7,9}$ (m².s)	*0.15*	13.25	*0.09*

* A spacing of 1 is used for the integration of all the areas for a more reasonable size. To have the real values of area, the listed values need to be multiplied by the spacing increment which is $\frac{1}{\text{sampling rate} \times \text{nfft}} = \frac{1}{0.1768 \times 2048} = 0.0028 Hz$

** The values in italic are below the chosen threshold value: 5. They will be neglected in the equation of motion.

Table 4.1 Area under the cross power density spectrum (0^{th} moment) of different motion pairs.

Although the cross power density spectra help to visualize the quantitative of the cross coupling effect, but since both translational motions (surge, sway and heave) and angular motions (roll, pitch and yaw) are involved, they have different units. The question arises as how to compare the importance of the cross coupling terms having different units. In the present case, the fluctuations of the motions have about the same order of magnitude (see Tables 2.2 and 2.3), it is reasonable to choose a single threshold value. Otherwise the values will need to be normalized by a characteristic magnitude of translational motion and / or rotation angle. It was initially considered to use coherence function or correlation coefficient for this purpose because they are both dimensionless and they can indicate the linear correlation between two motions. However, it is possible to obtain a very high coherence or correlation coefficient even when the related energy is low. This can be misleading for the problem here, which is why only the energy is considered.

After having performed several sensitivity tests, the threshold value is chosen to be 5 for all the 0^{th} moments. The cross-coupling terms that are kept in the barge and ship system are those for the ship surge / ship heave, ship surge / ship pitch, ship sway / ship roll, ship sway / ship yaw, ship heave / ship pitch, ship roll / ship yaw, barge pitch / ship heave, barge pitch / ship roll, barge pitch / ship pitch. Among which ship surge / ship pitch and ship surge / ship heave interaction is important only for the 45° exposed configuration (considering the fact that the surge time series is not reliable for the 0° heading configuration), and ship sway / ship yaw interaction can be neglected for the shielded -45° heading condition. To summarize, the surge, heave and pitch motions are coupled between them and the sway, roll and yaw motions are coupled between them as in a single body system, but pitch / roll interaction can be observed as well in this two-body system.

To valid the threshold value, the equation of motion with simplified matrix and that with the complete matrix were used in the R-MISO analysis and the goodness of fit of each model was calculated and compared. The example of the barge pitch motion in head

seas is used to illustrate that because several elements are neglected (three for each of the added-mass and the linear damping matrix) and still both hydrodynamic parameters for the single barge and those for the two-body interaction are presented. In the simplified calculation, all the motion data that have a low 0^{th} moment with the output barge pitch moment are not used as input. Note that the nonlinear terms are not considered in this section, because the objective is not to have the optimal model but, to assess the difference of results when the hydrodynamic parameter matrixes of the linear terms are simplified. The nonlinear terms are presented in both simplified and complete equations of motion, thus do not provide additional help when comparing the two alternatives. They will however be considered in the next section when the detailed R-MISO analysis is carried out.

The cumulative coherence functions for the case with complete matrixes and that with simplified matrixes are compared as shown in Figure 4.2. The curve with the highest coherence represents the final goodness-of-fit of the model. It can be seen that in the barge pitch case, the model with simplified matrixes using only four inputs has a goodness-of-fit that is similar to the one of the model with complete matrixes using all the seven inputs. The largest difference occurs around the dip at 0.133Hz and is about 3%. The further simplification of the matrixes will however cause quite significant decrease in the total coherence. This shows that the choice of the threshold value is adequate.

(a)

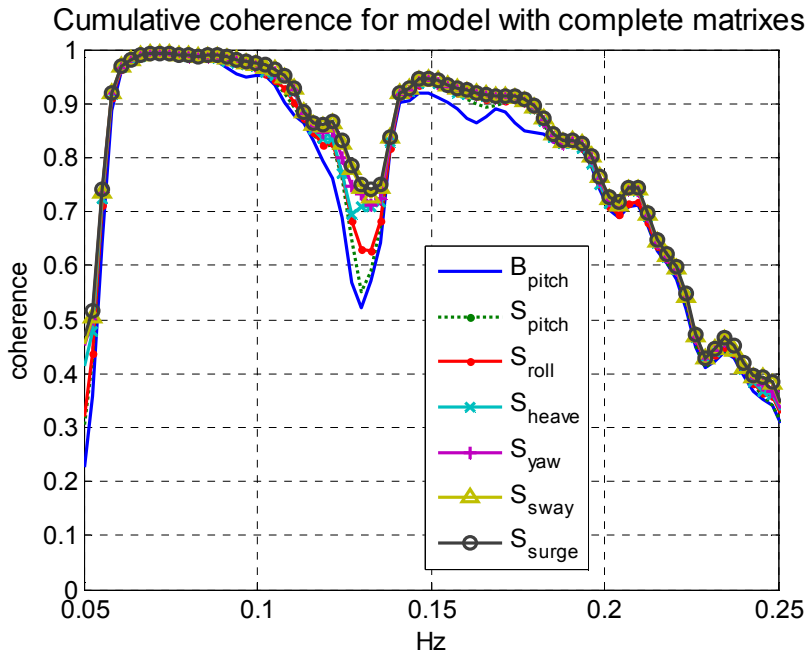

(b)

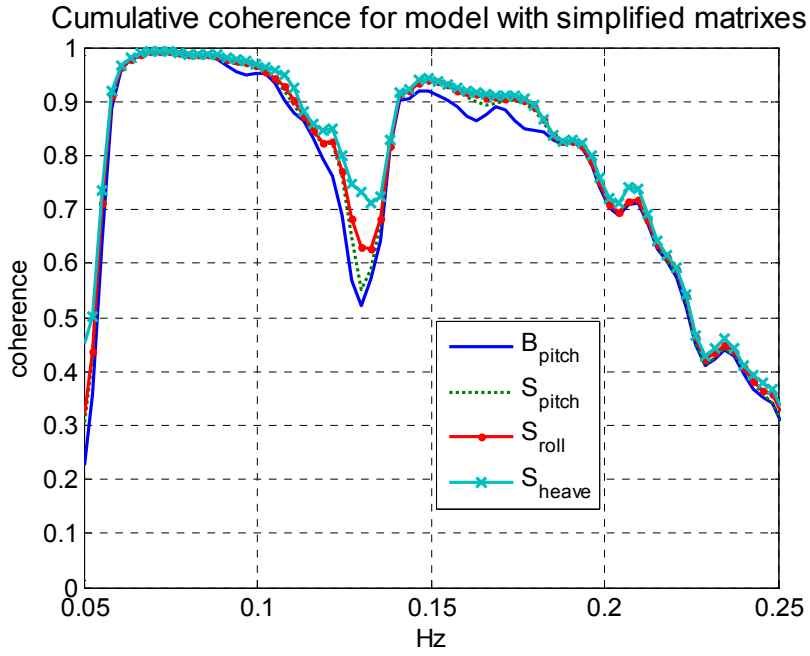

Figure 4.2 (a) Cumulative coherence function with all the coefficients; (b) Cumulative coherence function with only the most important coefficients.

Note that the cumulative coherence functions shown can be decomposed into partial coherence functions that give a better visualization of the contribution of each input to the goodness-of-fit of the model. Figure 4.3 shows clearly that the three discarded inputs have the smallest contribution. It needs to be underlined that the partial coherence functions provide the individual contribution of the inputs that are conditioned, meaning that the influences of the previous inputs are successively removed. If the inputs are not well sorted according to the degree of interaction between them and the output the results can be somehow different. Thus although it is a good tool to double check the adequacy of the simplification, it is preferable to use the cross-power density spectrum between the non-conditioned time series for the simplification itself.

With the simplification of the parameter matrixes based on both the geometry symmetry and the energy concentration, the number of the hydrodynamic parameters to be identified is largely reduced. For the ship and barge system considered in the current problem, the total number of non-zero parameters range from 33 for the -45° shielded configuration to 39 for the 45° exposed configuration.

4.2 System identification analysis and results

Several cases were studied for the coupled barge and ship system. First, the barge pitch motion in head seas, it allows for a comparison with the same motion in the single barge configuration studied in Section 3. Followed by an analysis of the ship roll motion in head seas to show how the interaction can alter the motion behavior of a vessel. And finally the ship heave motion is studied in both head seas and quartering seas to assess the effect of the heading condition.

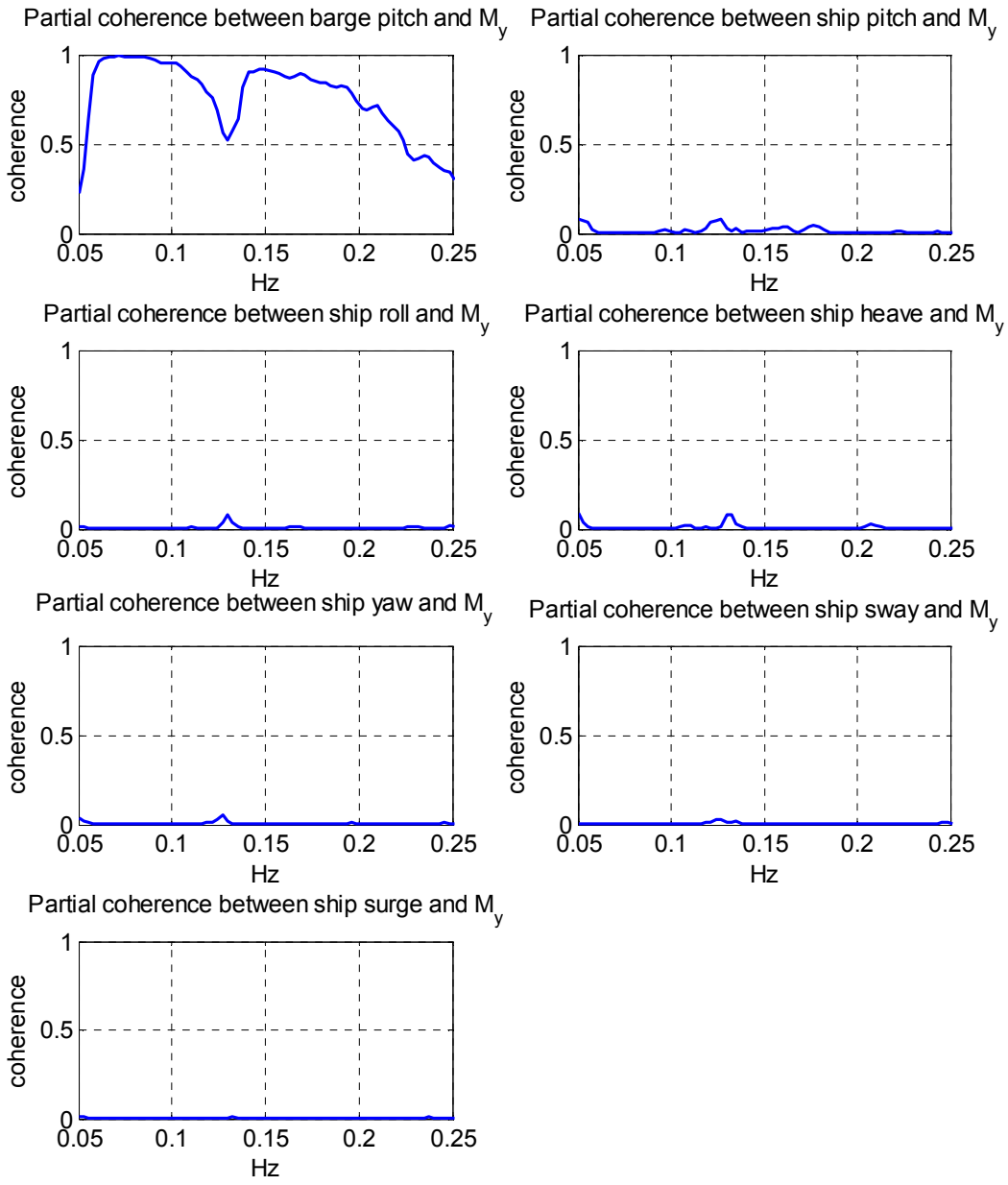

Figure 4.3 Partial coherence functions between the inputs and the output of the model.

4.2.1 Barge pitch in head seas

The integro-differential equation of motion for barge pitch is:

$$\begin{aligned}
&\int_0^t \left(I_{yy_B} + a_{5,5}\right)(\tau)\ddot{\theta}_B(t-\tau)d\tau + \int_0^t c_{5,5}(\tau)\dot{\theta}_B(t-\tau)\,d\tau + k_{5,5}\theta_B(t) \\
&+\int_0^t a_{5,9}(\tau)\ddot{z}_S(t-\tau)d\tau + \int_0^t c_{5,9}(\tau)\dot{z}_S(t-\tau)\,d\tau \\
&+\int_0^t a_{5,10}(\tau)\ddot{\phi}_S(t-\tau)d\tau + \int_0^t c_{5,10}(\tau)\dot{\phi}_S(t-\tau)\,d\tau \\
&+\int_0^t a_{5,11}(\tau)\ddot{\theta}_S(t-\tau)d\tau + \int_0^t c_{5,11}(\tau)\dot{\theta}_S(t-\tau)\,d\tau \\
&+\int_0^t d_{5,5}(\tau)\left[\dot{z}_B(t-\tau)-\dot{w}(t-\tau)\right]\left|\dot{z}_B(t-\tau)-\dot{w}(t-\tau)\right|d\tau + \int_0^t r_{5,5}(\tau)\theta_B(t-\tau)\left|\theta_B(t-\tau)\right|d\tau \\
&= M_y(t)
\end{aligned} \tag{4.11}$$

This equation only contains the mathematical input motions that are viewed as important based on Table 4.1: barge pitch, ship heave, ship roll and ship pitch. Compared to the equation of motion of the same motion in the single barge configuration (see Equation 3.9), Equation 4.11 is more complicated because of the interaction with the ship. The ship heave, roll and pitch motions will all be coupled to the barge pitch motion. There are thereby four linear and two nonlinear physical outputs. The physical input $M_y(t)$ is also different from the one in the single barge case because the moments due to the mooring line and fender forces were accounted for too. Again, the quadratic relative vertical velocity term $\left[\dot{z}_B(t)-\dot{w}(t)\right]\left|\dot{z}_B(t)-\dot{w}(t)\right|$ is used for the nonlinear damping force and the quadratic angular displacement $\theta_B(t)\left|\theta_B(t)\right|$ is used for the nonlinear restoring force because they are the most common nonlinear expressions that one would expect. However, the R-MISO method can estimate their relevancy at the end of the parameter identification procedure and they can be replaced by other nonlinear terms as deemed appropriate.

The physical input and outputs are inversed to obtain respectively the mathematical inputs and output. After Fourier transform the equation of motion becomes:

$$\begin{aligned} &A_1(f)X_1(f)+A_2(f)X_2(f)+A_3(f)X_3(f)+A_4(f)X_4(f) \\ &+A_5(f)X_5(f)+A_6(f)X_6(f)=Y(f) \end{aligned} \tag{4.12}$$

With X_i the Fourier transform of the mathematical inputs, Y the Fourier transform of the output and A_i the transfer functions relating each input to the output.

$$A_1(f)=k_{5,5}+j(2\pi f)c_{5,5}(f)-(2\pi f)^2\left(I_{yy_B}+a_{5,5}\right)(f) \tag{4.13}$$

$$A_2(f)=k_{5,9}+j(2\pi f)c_{5,9}(f)-(2\pi f)^2 a_{5,9}(f) \tag{4.14}$$

$$A_3(f)=k_{5,10}+j(2\pi f)c_{5,10}(f)-(2\pi f)^2 a_{5,10}(f) \tag{4.15}$$

$$A_4(f)=k_{5,11}+j(2\pi f)c_{5,11}(f)-(2\pi f)^2 a_{5,11}(f) \tag{4.16}$$

$$A_5(f)=d_{5,5} \tag{4.17}$$

$$A_6(f)=r_{5,5} \tag{4.18}$$

$$X_1(f)=\text{Fourier transform of } \theta_B(t) \text{ (barge pitch)} \tag{4.19}$$

$$X_2(f)=\text{Fourier transform of } z_S(t) \text{ (ship heave)} \tag{4.20}$$

$$X_3(f)=\text{Fourier transform of } \phi_S(t) \text{ (ship roll)} \tag{4.21}$$

$X_4(f)$ = Fourier transform of $\theta_S(t)$ (ship pitch) (4.22)

$X_5(f)$ = Fourier transform of $(\dot{z}(t)-\dot{w}(t))|\dot{z}(t)-\dot{w}(t)|$ (4.23)

$X_6(f)$ = Fourier transform of $\theta(t)|\theta(t)|$ (4.24)

$Y(f)$ = Fourier transform of M_y (4.25)

Once the transfer functions A_i are found, it will be possible to identify the parameters in the following way:

$$(I_{yy}+a_{5,5})(f)=\frac{k_{5,5}-\mathrm{Re}(A_1(f))}{(2\pi f)^2} \tag{4.26}$$

$$a_{5,9}(f)=\frac{-\mathrm{Re}(A_2(f))}{(2\pi f)^2} \tag{4.27}$$

$$a_{5,10}(f)=\frac{-\mathrm{Re}(A_3(f))}{(2\pi f)^2} \tag{4.28}$$

$$a_{5,11}(f)=\frac{-\mathrm{Re}(A_4(f))}{(2\pi f)^2} \tag{4.29}$$

$$c_{5,5}(f)=\frac{\mathrm{Im}(A_1(f))}{2\pi f} \tag{4.30}$$

$$c_{5,9}(f) = \frac{\mathrm{Im}(A_2(f))}{2\pi f} \tag{4.31}$$

$$c_{5,10}(f) = \frac{\mathrm{Im}(A_3(f))}{2\pi f} \tag{4.32}$$

$$c_{5,11}(f) = \frac{\mathrm{Im}(A_4(f))}{2\pi f} \tag{4.33}$$

$$d_{5,5} = \mathrm{Re}(A_5) \tag{4.34}$$

$$r_{5,5} = \mathrm{Re}(A_6) \tag{4.35}$$

The linear stiffness coefficient $k_{5,5}$ is constant and is calculated in Appendix C. The coefficients $k_{5,9}$, $k_{5,10}$, and $k_{5,11}$ are neglected as stated earlier.

Figure 4.4 shows the auto-spectral densities of the most important input barge pitch and the auto-spectrum of the output barge pitch moment. Two peaks can be observed: one wave frequency peak corresponding to the 10.2s wave period, another one, around 0.13Hz, corresponds likely to the resonance frequency for the pitch motion. Outside of the frequency range [0.05Hz, 0.2Hz], the energy is almost zero. However in Section 2 it was estimated that the frequency of the first mode tank wave sloshing is 0.23Hz in the 80% filled configuration in head seas, the frequency range of interest is thereby extended to [0.05Hz, 0.25Hz] in order to detect the influence of the tank wave, if any.

(a)

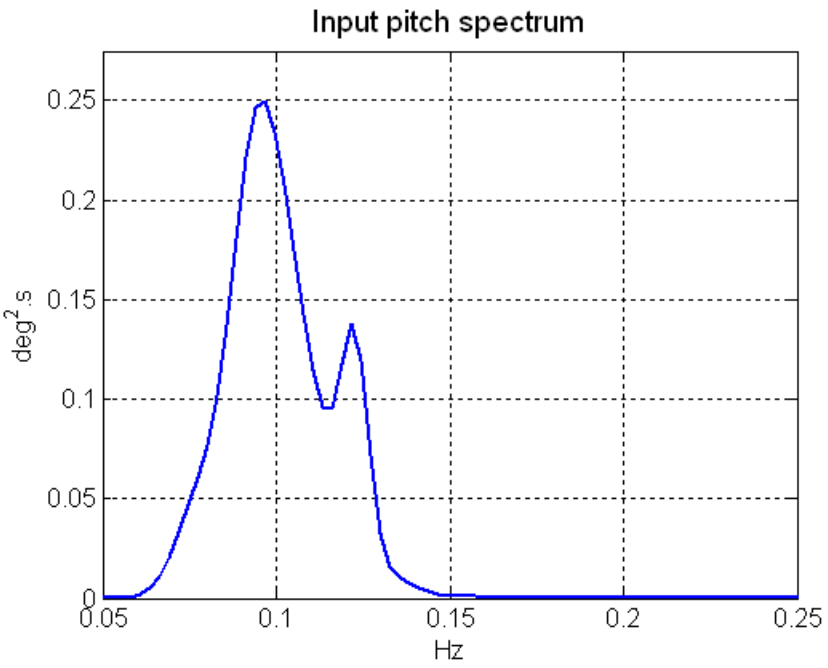

(b)

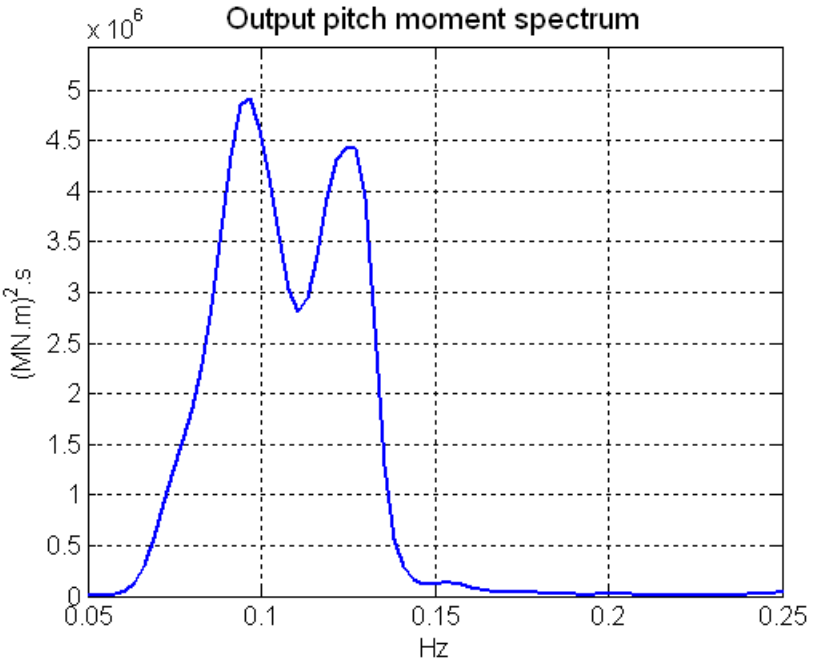

Figure 4.4 Auto-spectral densities of (a) the input barge pitch $\theta_B(t)$, and (b) the output barge pitch moment $M_y(t)$, 0° heading.

A first attempt was made using the equation of motion of Equation 4.11. The cumulative coherence function is shown in Figure 4.6. It is different from Figure 4.2b because it contains also the nonlinear damping and the nonlinear stiffness terms. It is obvious that the system remain very linear with the barge pitch motion being the most important input. Surge pitch, roll and heave motions as well as the nonlinear damping term add more coherence near the resonance frequencies. There is no contribution from the nonlinear stiffness except a very slight additional goodness-of-fit around 0.23Hz. Since this frequency corresponds to the frequency of the first mode tank wave sloshing in the 80% filled configuration in head seas, it can be assumed that some nonlinear stiffness is brought from the tank wave sloshing effect. Due to its very low contribution, the quadratic pitch nonlinear stiffness term is discarded.

There is a large dip around 0.13Hz due to the deterioration of the R-MISO method accuracy around resonance frequencies. The coherence is also low at the extremity of the frequency range which is caused by the low energy presented in those frequencies as explained in Section 3. For the frequencies corresponding to significant energy concentration of the input barge pitch and output barge pitch moment (roughly from 0.06Hz to 0.15Hz), the final goodness-of-fit is higher than 70% which is a quite satisfactory result. However it is still desirable to improve the coherence. Since the linear part of the equation of motion is quite well established, to improve the overall goodness-of-fit of the model different forms of nonlinear terms were tested. This including using other vessel motions that have a higher energy concentration around 0.13Hz than the barge pitch motion, as well as the mooring line and fender forces. It was observed that adding quadratic mooring line forces can improve the overall coherence of the model as illustrated by Figure 4.7. It was seen in Section 2 that the surge motion and the mooring line forces were highly coupled, this may explain why the pitch motion, which is usually coupled with the surge motion is influenced by the mooring line forces. Only three of the four mooring lines need to be used: bow lines #1 and #2 and stern line #1.

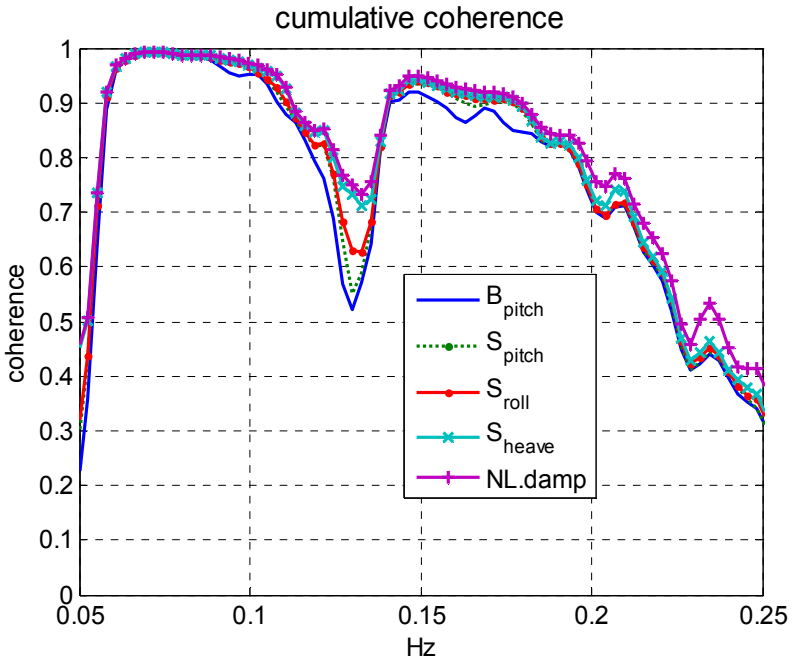

Figure 4.5 Goodness-of-fit of the initial model, barge pitch case, 0˚ heading.

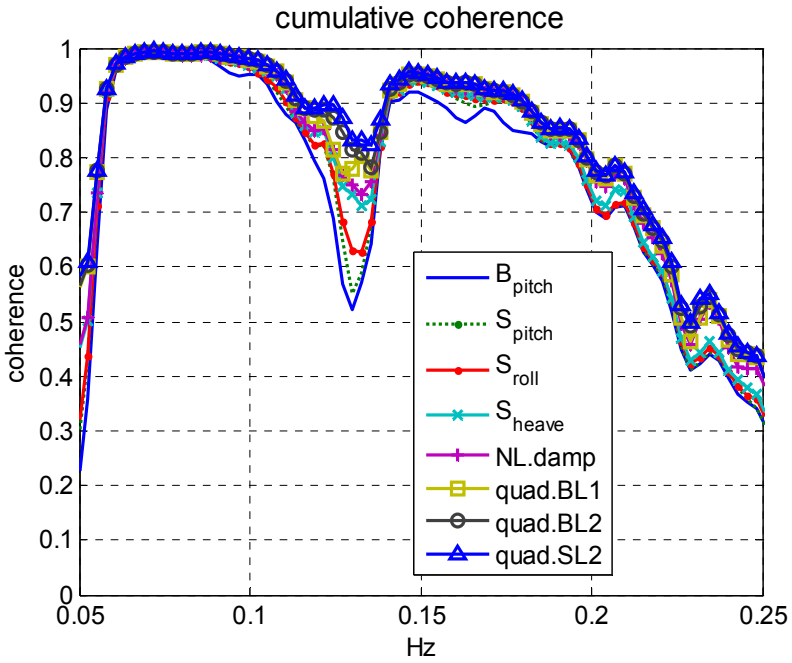

Figure 4.6 Goodness-of-fit of the final model, barge pitch case, 0˚ heading.

Figure 4.8 gives an overview of the individual contribution of each input.

After the abandon of the nonlinear stiffness term and the addition of the three quadratic mooring line force terms, the final equation of motion adopted for the problem becomes:

$$
\begin{aligned}
&\int_0^t \left(I_{yy_B} + a_{5,5}\right)(\tau)\ddot{\theta}_B(t-\tau)d\tau + \int_0^t c_{5,5}(\tau)\dot{\theta}_B(t-\tau)\,d\tau + k_{5,5}\theta_B(t) \\
&+\int_0^t a_{5,9}(\tau)\ddot{z}_S(t-\tau)d\tau + \int_0^t c_{5,9}(\tau)\dot{z}_S(t-\tau)\,d\tau \\
&+\int_0^t a_{5,10}(\tau)\ddot{\phi}_S(t-\tau)d\tau + \int_0^t c_{5,10}(\tau)\dot{\phi}_S(t-\tau)\,d\tau \\
&+\int_0^t a_{5,11}(\tau)\ddot{\theta}_S(t-\tau)d\tau + \int_0^t c_{5,11}(\tau)\dot{\theta}_S(t-\tau)\,d\tau \\
&+\int_0^t d_{5,5}(\tau)\left[\dot{z}_B(t-\tau) - \dot{w}(t-\tau)\right]\left|\dot{z}_B(t-\tau) - \dot{w}(t-\tau)\right|d\tau \\
&+\int_0^t l_{B1}(\tau)\,BL1(t-\tau)\left|BL1(t-\tau)\right|d\tau \\
&+\int_0^t l_{B2}(\tau)\,BL2(t-\tau)\left|BL2(t-\tau)\right|d\tau \\
&+\int_0^t l_{S2}(\tau)\,SL2(t-\tau)\left|SL2(t-\tau)\right|d\tau \\
&= M_y(t)
\end{aligned}
\tag{4.36}
$$

With

$BL1(t)\left|BL1(t)\right|$ = the quadratic mooring line force of bow line #1.

$BL2(t)\left|BL2(t)\right|$ = the quadratic mooring line force of bow line #2.

$SL2(t)\left|SL2(t)\right|$ = the quadratic mooring line force of stern line #2.

l_{B1}, l_{B2}, l_{S2} = the coefficients related to the previous three quadratic terms.

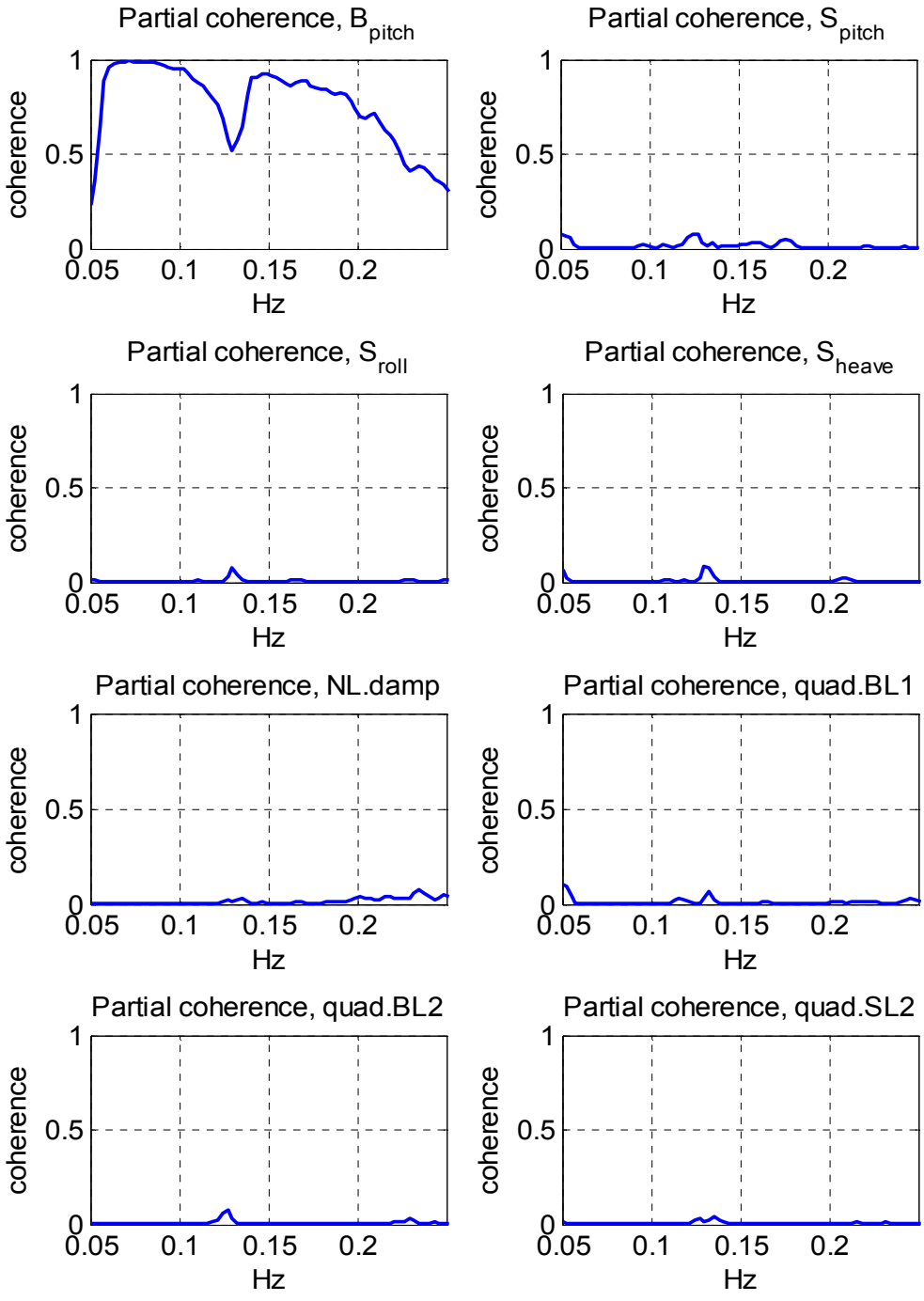

Figure 4.7 Partial coherence functions of the inputs, barge pitch case, 0˚ heading.

Figure 4.9 illustrates the magnitude and the phase of the transfer function $A_1(f)$ which relates the barge pitch motion to the output barge pitch moment. Compared to the same transfer function in case of the single barge (Figure 3.7), the main shape of the magnitude remains quite similar although the fluctuation is larger in the present case. The related virtual mass $\left(I_{yy_B} + a_{5,5}\right)(f)$ is also very similar to the one in the single barge case as indicated by Figure 4.10.

As for the phase of the transfer function $A_1(f)$, the phase shift is no longer close to 0. In particular a 90 degree shift can be observed near the resonance frequency around 0.12 Hz. This shows that the damping affects more the barge pitch motion in the present case than it did when the barge was alone. Indeed the values of the linear damping coefficient $c_{5,5}(f)$ are much larger than the ones estimated for the single barge. However, negative linear damping was observed around the resonance frequency which is fundamentally different from the behavior of a single body vessel. This can be caused by the pumping mode of the water trapped in the gap between the barge and the ship which excites the vessel motions instead of providing damping effects. If the moment of inertia I_{yy_B} could have been estimated, then the extracted added mass $a_{5,5}(f)$ would most likely to behave in a similar way, i.e. to have negative values near the resonance frequencies due to the pumping mode of the gap water.

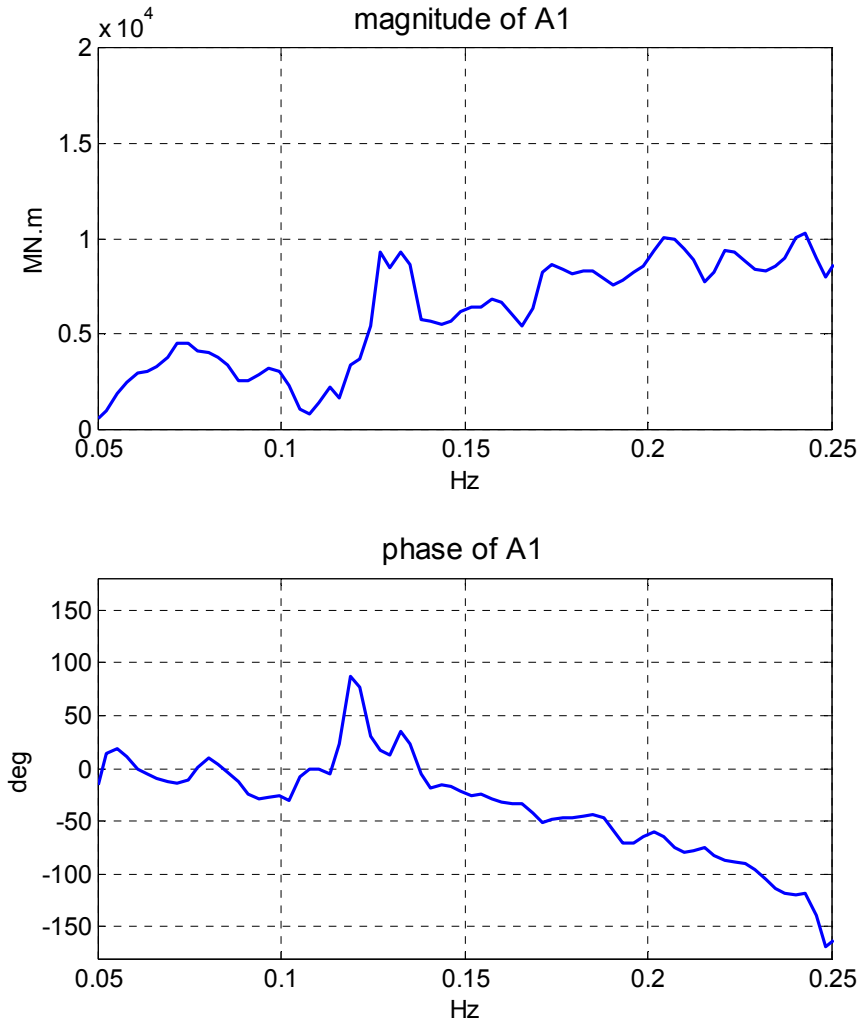

Figure 4.8 Magnitude and phase of the transfer function $A_1(f)$, barge pitch case, 0° heading.

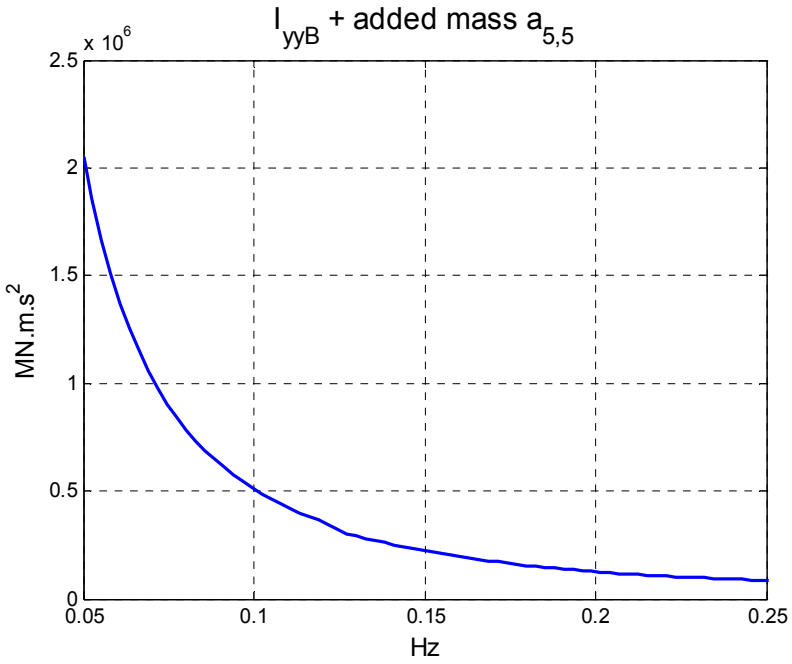

Figure 4.9 Virtual mass coefficient $\left(I_{yy_B} + a_{5,5}\right)(f)$, barge pitch case, 0° heading.

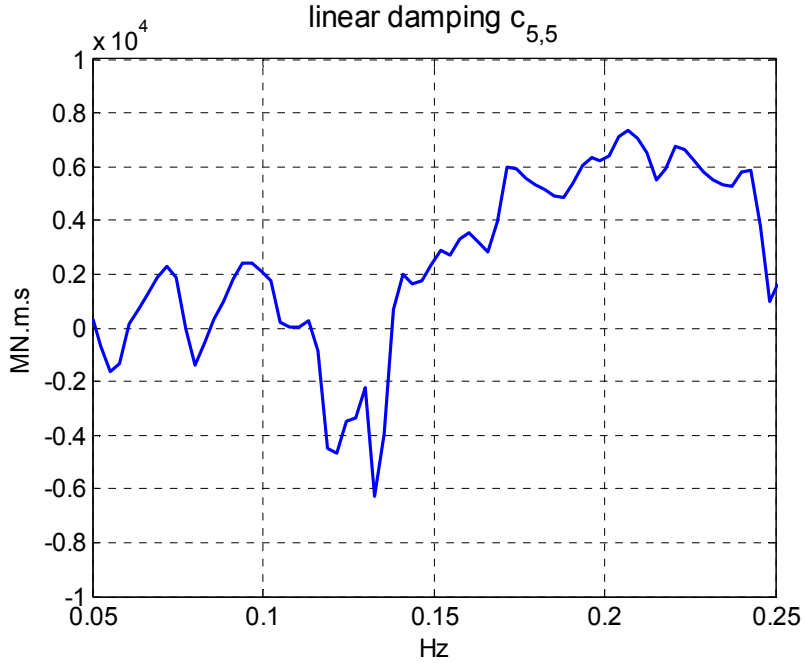

Figure 4.10 Linear damping coefficient $c_{5,5}(f)$, barge pitch case, 0° heading.

$a_{5,5}(f)$ and $c_{5,5}(f)$ are the diagonal terms from the equation of motion. In the case of a two-body system, the off-diagonal terms can be important as well as mentioned earlier. Figure 4.12 assembles the plots of the three cross-coupling added-mass coefficients estimated important: $a_{5,9}(f)$, $a_{5,10}(f)$ and $a_{5,11}(f)$ which relate the barge pitch motion to respectively the ship heave, ship roll and ship pitch motions. For $a_{5,9}(f)$ and $a_{5,11}(f)$, their values are generally close to zero, except near the resonance frequencies where some of negative results can be observed. It seems that the hydrodynamic interactions are important due to the proximity between the two vessels. In the case of the added-mass $a_{5,10}(f)$, visible oscillation can be observed in lower frequencies, it is possible that the interaction between the barge pitch and the ship roll motion is partly caused by lower frequency effect of the mooring system. Similarly, Figure 4.13 illustrate the cross-coupling linear damping coefficients $c_{5,9}(f)$, $c_{5,10}(f)$ and $c_{5,11}(f)$. Again, outside of the resonance frequencies these values are quite small unlike the diagonal linear damping coefficient $c_{5,5}(f)$, confirming that the interaction is caused by the close proximity of the two vessels. The magnitudes of these cross-coupling terms remain small compared to the diagonal term.

Two kinds of nonlinear terms were included in the equation of motion for the study of the barge pitch motion: quadratic relative vertical velocity term (nonlinear damping) and the quadratic mooring line force terms. Their estimated values are plotted respectively in Figure 4.14 and Figure 4.15. The quadratic mooring line force terms are only relevant to the two body system and they reveal to be important since they improved the overall goodness-of-fit of the model by almost 10% near the resonance frequencies.

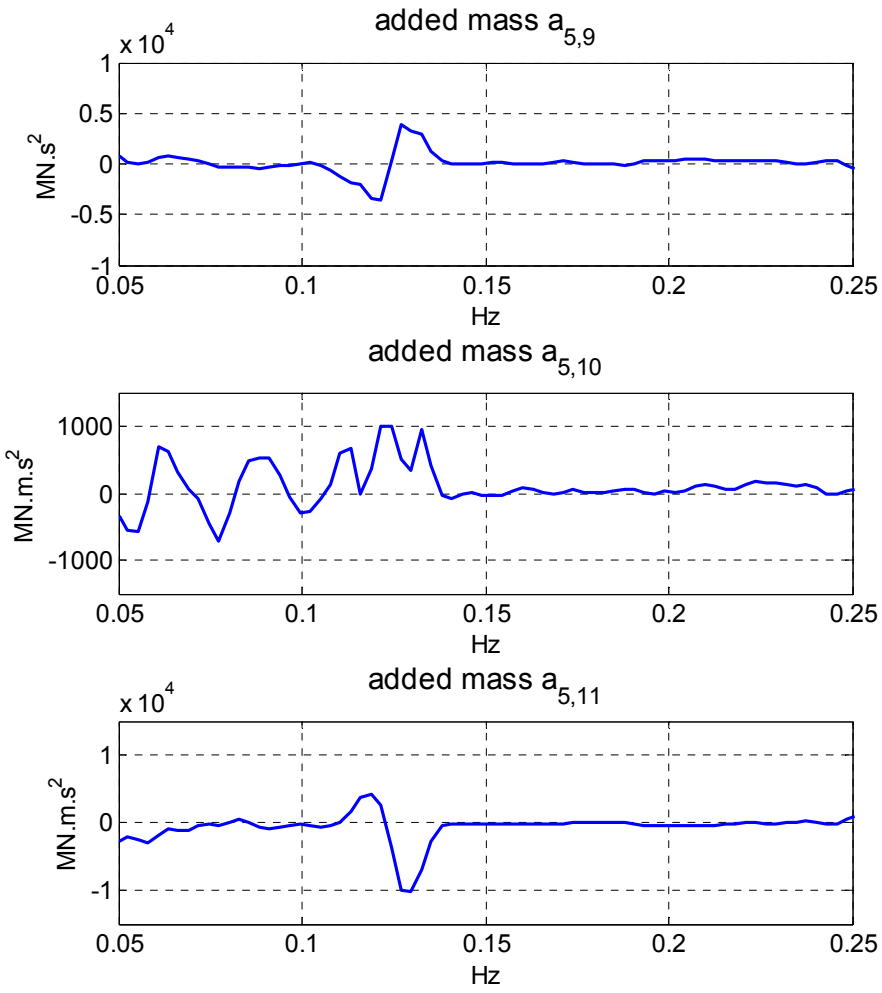

Figure 4.11 Added mass coefficients of the cross coupling terms, barge pitch case, 0˚ heading.

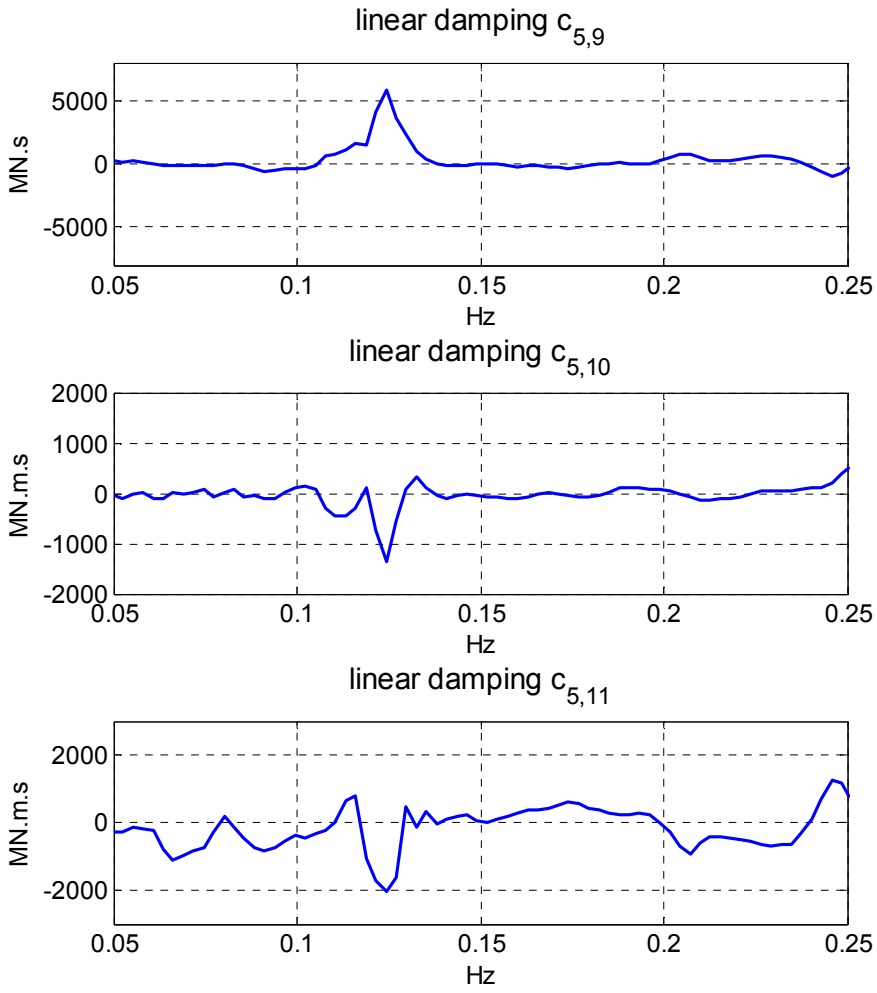

Figure 4.12 Linear damping coefficients of the cross coupling terms, barge pitch case, 0˚ heading.

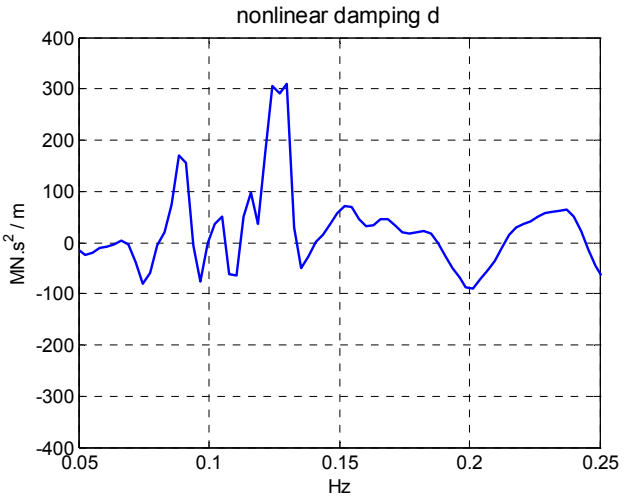

Figure 4.13 Nonlinear damping coefficient, barge pitch case, 0˚ heading.

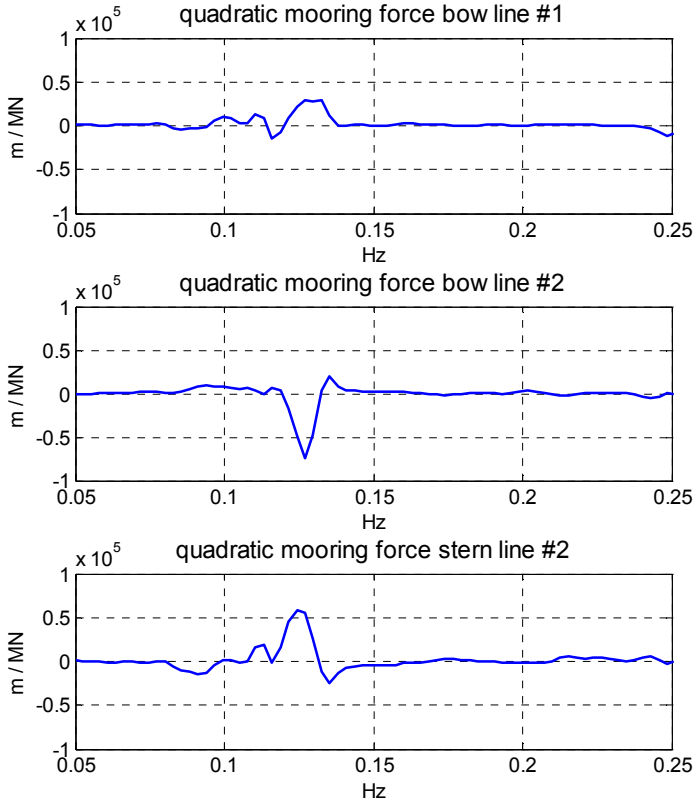

Figure 4.14 Quadratic mooring line force coefficients, barge pitch case, 0˚ heading.

The measured mathematical inputs and the identified parameters were used to reconstitute the output barge pitch moment. The estimated output data was compared with the measured values in Figure 4.16. As in the single body case, the simulated data has a periodicity that marches in general quite well with the measured data although some phase shifts can be observed. The amplitude of the simulated data can however largely deviate from the measured value. Besides the imperfection of the mathematical model itself and some possible measurement noises induced during the model tests, the numerous estimations (derivatives of the time series, linear stiffness coefficient and decomposed mooring and fender forces) can be an important source of inaccuracy of the result.

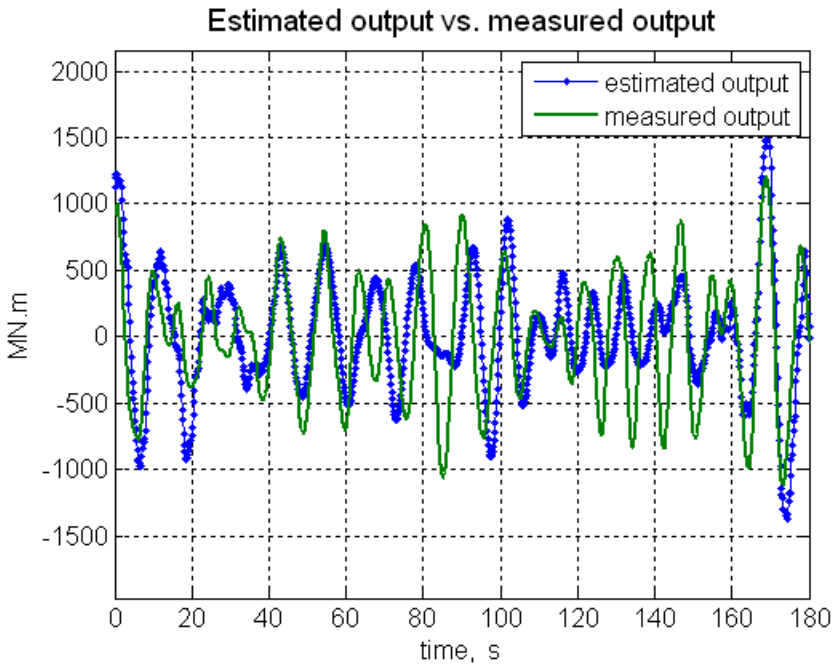

Figure 4.15 Comparison between the reconstituted barge pitch moment and the measured barge pitch moment, two body system.

4.2.2 Ship roll in head seas

The ship roll motion in head seas is an interesting subject of study. Since the ship is longitudinally symmetric, it is expected that its roll motion will be minimal in head seas. However in Section 2 it was seen that its magnitude is quite important. Hydrodynamic parameters for this configuration were computed with R-MISO method in order to give some insight.

Based on Table 4.1, the simplified equation of motion is:

$$\begin{aligned}
&\int_0^t a_{10,5}(\tau)\ddot{\theta}_B(t-\tau)d\tau + \int_0^t c_{10,5}(\tau)\dot{\theta}_B(t-\tau)\,d\tau \\
&+\int_0^t \left(-mz_G + a_{10,8}\right)(\tau)\ddot{y}_S(t-\tau)d\tau + \int_0^t c_{10,8}(\tau)\dot{y}_S(t-\tau)\,d\tau \\
&+\int_0^t \left(I_{xx_S} + a_{10,10}\right)(\tau)\ddot{\phi}_S(t-\tau)d\tau + \int_0^t c_{10,10}(\tau)\dot{\phi}_S(t-\tau)\,d\tau + k_{10,10}\phi_S(t) \\
&+\int_0^t \left(-I_{xz} + a_{10,12}\right)(\tau)\ddot{\psi}_S(t-\tau)\,d\tau + \int_0^t c_{10,12}(\tau)\dot{\psi}_S(t-\tau)\,d\tau \\
&+\int_0^t d_{10,10}(\tau)\left[\dot{z}_S(t-\tau) - \dot{w}(t-\tau)\right]\left|\dot{z}_S(t-\tau) - \dot{w}(t-\tau)\right|d\tau \\
&+\int_0^t r_{10,10}(\tau)\phi_S(t-\tau)\left|\phi_S(t-\tau)\right|d\tau \\
&= M_x(t)
\end{aligned} \tag{4.37}$$

The cross-coupling terms that are deemed to be important include those relate the ship roll motion to the barge pitch, ship sway and ship yaw motions. Again, the quadratic relative vertical velocity term $\left[\dot{z}_B(t) - \dot{w}(t)\right]\left|\dot{z}_B(t) - \dot{w}(t)\right|$ is used for the nonlinear damping force and the quadratic displacement $\phi_S(t)\left|\phi_S(t)\right|$ is used for the nonlinear restoring force because they are the most common nonlinear expressions that one would expect. But the R-MISO method can estimate their relevancy at the end of the parameter identification procedure and replace them by other nonlinear terms if necessary.

Figure 4.16 shows the spectral densities of the mathematical input ship roll and the mathematical output ship roll moment, [0.05Hz, 0.25Hz] remains the frequency range of interest.

The overall goodness-of-fit of the model proposed by Equation 4.36 can be quite low for certain frequencies as shown by Figure 4.18. To improve this, different forms of nonlinear terms were tested. As in the previous case of barge pitch, other vessel motions that have a higher energy concentration around 0.13Hz than the ship roll motion were tested, as well as the mooring line and fender forces. The quadratic mooring line forces and the quadratic fender forces can effectively add coherence to the model. Figure 4.19 shows the improved goodness-of-fit. Although the coherence remains relatively low at some frequencies, but improvements up to 20% can be observed. Figure 4.20 lists the partial coherence functions that put into evidence the individual contribution of each input. It is interesting to see that in the barge pitch case studied earlier only the quadratic mooring line forces were relevant, whereas in the present case the quadratic fender forces are important as well. Actually one of the main conclusions from the motion analysis in Section 2 is that the roll motion is the motion most correlated with the fender forces. Consistently the R-MISO analysis demonstrated that the model needs to include the influences of these forces. The nonlinear stiffness term which is expressed as the quadratic roll motion has very small contribution to the model and is therefore neglected.

(a)

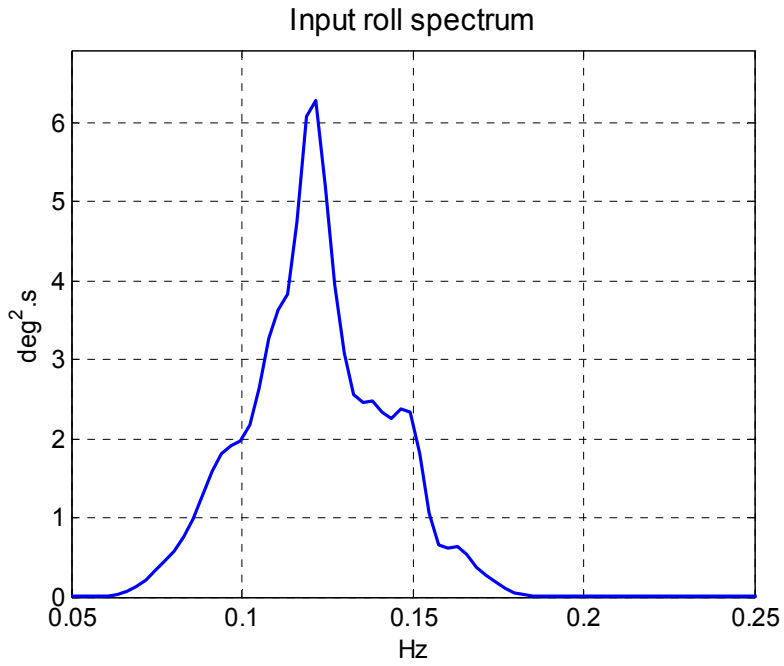

(b)

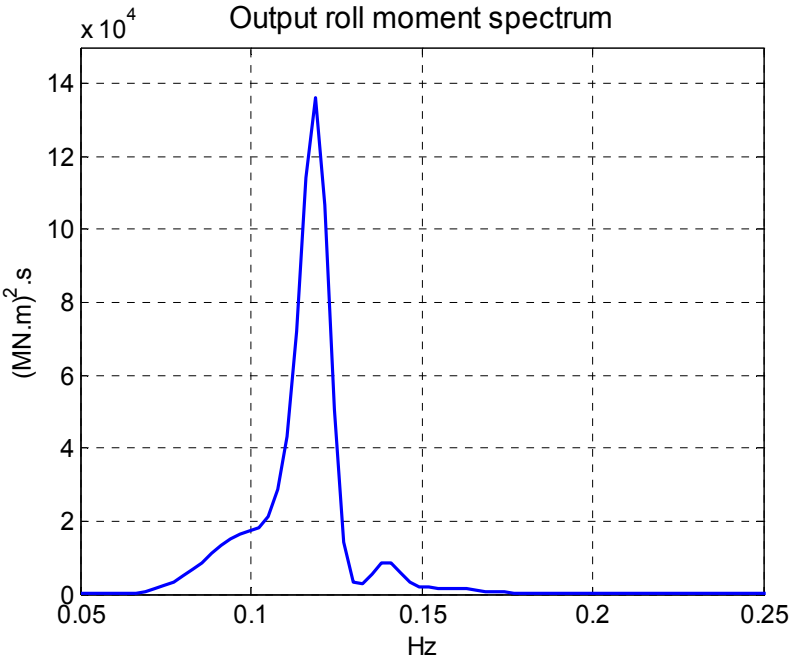

Figure 4.16 Auto-spectral densities of (a) the input ship roll $\phi_S(t)$, and (b) the output ship roll moment $M_x(t)$, 0° heading.

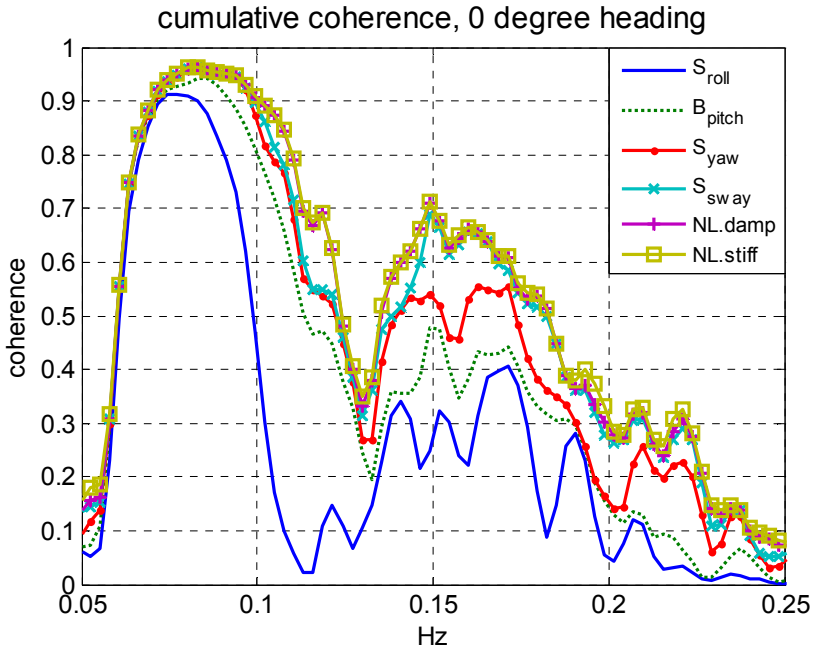

Figure 4.17 Goodness-of-fit of the initial model, ship roll case, 0˚ heading.

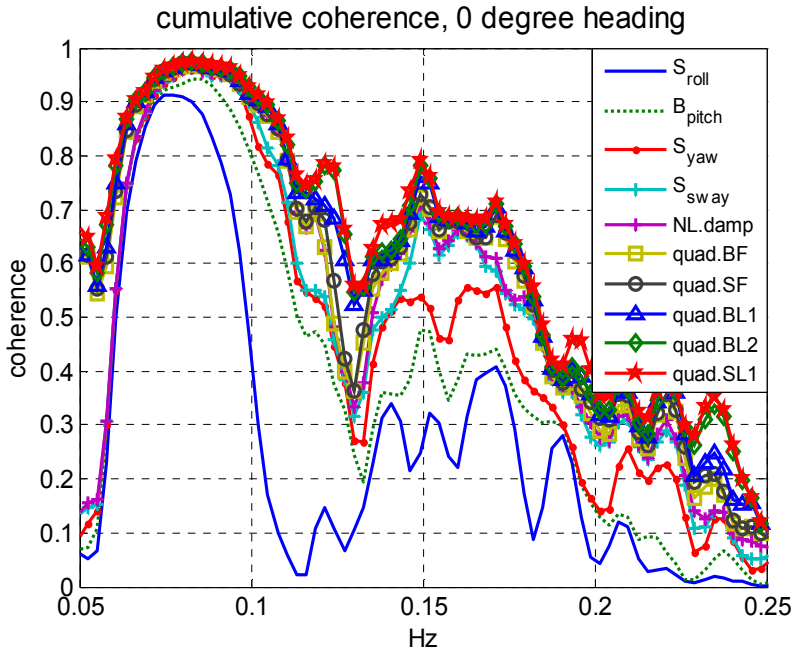

Figure 4.18 Goodness-of-fit of the final model, ship roll case, 0˚ heading.

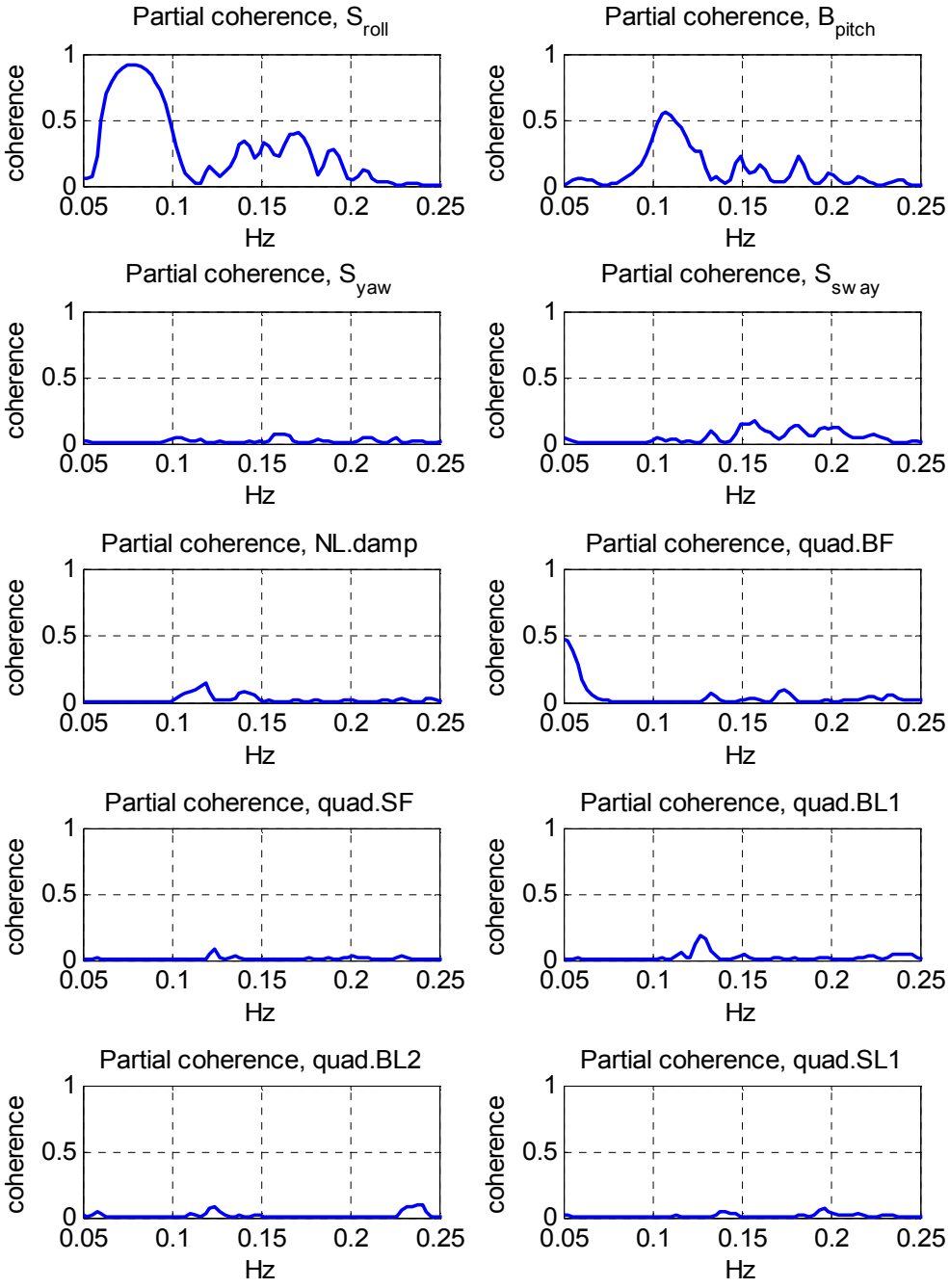

Figure 4.19 Partial coherence functions of the inputs, ship roll case, 0˚ heading.

The equation of motion of the final model is:

$$\begin{aligned}
&\int_0^t a_{10,5}(\tau)\ddot{\theta}_B(t-\tau)d\tau + \int_0^t c_{10,5}(\tau)\dot{\theta}_B(t-\tau)d\tau \\
&+\int_0^t \left(-mz_G + a_{10,8}\right)(\tau)\ddot{y}_S(t-\tau)d\tau + \int_0^t c_{10,8}(\tau)\dot{y}_S(t-\tau)d\tau \\
&+\int_0^t \left(I_{xx_S} + a_{10,10}\right)(\tau)\ddot{\phi}_S(t-\tau)d\tau + \int_0^t c_{10,10}(\tau)\dot{\phi}_S(t-\tau)d\tau + k_{10,10}\phi_S(t) \\
&+\int_0^t \left(-I_{xz} + a_{10,12}\right)(\tau)\ddot{\psi}_S(t-\tau)d\tau + \int_0^t c_{10,12}(\tau)\dot{\psi}_S(t-\tau)d\tau \\
&+\int_0^t d_{10,10}(\tau)\left[\dot{z}_S(t-\tau) - \dot{w}(t-\tau)\right]\left|\dot{z}_S(t-\tau) - \dot{w}(t-\tau)\right|d\tau \\
&+\int_0^t l_{BF}(\tau)BF(t-\tau)\left|BF(t-\tau)\right|d\tau + \int_0^t l_{SF}(\tau)SF(t-\tau)\left|SF(t-\tau)\right|d\tau \\
&+\int_0^t l_{B1}(\tau)BL1(t-\tau)\left|BL1(t-\tau)\right|d\tau + \int_0^t l_{B2}(\tau)BL2(t-\tau)\left|BL2(t-\tau)\right|d\tau \\
&+\int_0^t l_{S1}(\tau)SL1(t-\tau)\left|SL1(t-\tau)\right|d\tau \\
&= M_x(t)
\end{aligned} \tag{4.38}$$

All the notations are the same as before, with the addition of the quadratic bow fender force term $BF(t)\left|BF(t)\right|$ and the quadratic stern fender force term $SF(t)\left|SF(t)\right|$ and their related coefficients l_{BF}, l_{SF}.

After the Fourier transform, Equation 4.37 becomes:

$$\begin{aligned}
&A_1(f)X_1(f) + A_2(f)X_2(f) + A_3(f)X_3(f) + A_4(f)X_4(f) + A_5(f)X_5(f) \\
&+A_6(f)X_6(f) + A_7(f)X_7(f) + A_8(f)X_8(f) + A_9(f)X_9(f) + A_{10}(f)X_{10}(f) \\
&= Y(f)
\end{aligned} \tag{4.39}$$

The transfer functions $A_1(f)$ to $A_4(f)$ have the form of:

$$A_1(f) = k_{10,10} + j(2\pi f)c_{10,10}(f) - (2\pi f)^2\left(I_{xx_S} + a_{10,10}\right)(f) \tag{4.40}$$

And the transfer functions $A_5(f)$ to $A_{10}(f)$ only have real parts that equal directly to the coefficients $d_{10,10}$, $r_{10,10}$, l_{BF}, l_{SF}, l_{B1}, l_{B2} and l_{S2}.

The R-MISO identification procedure is the same as the one described in section 4.2.1 and the hydrodynamic parameters were estimated. Figure 4.21 and Figure 4.22 are respectively the diagonal virtual mass coefficient $\left(I_{xx_S} + a_{10,10}\right)(f)$ and the diagonal linear damping coefficient $c_{10,10}(f)$. The virtual mass has the same decreasing shape as those observed in earlier cases and the linear damping coefficient is negative near the resonance frequency likely due to the gap wave effect. Negative values can also be observed in the off-diagonal added mass and linear damping coefficients as can be seen in Figures 4.23 and 4.24. Similar to what has been observed for the barge pitch motion, the cross-coupling linear damping coefficients are significant only for the frequencies near the resonance. However in the present case these cross-coupling coefficients are large compared to the diagonal coefficient $c_{10,10}(f)$, which was not true for the pitch motion. This indicates that the hydrodynamic interaction has a larger impact on the ship roll motion. The nonlinear damping, mooring line force and fender force terms are plotted respectively in Figures 4.25, 4.26 and 4.27. They also peak around the resonance frequencies and the mooring force coefficient has quite high values. All these observations show that although theoretically the roll motion should be minimal owed to the translational symmetry of the ship, it is actually important in a side-by-side moored two body system due to the hydrodynamic interactions caused by the presence of the nearby barge and the pumping wave in the gap between the vessels. The mechanical connectors such as the mooring lines and fenders also add to the interaction between the roll motion and other motions.

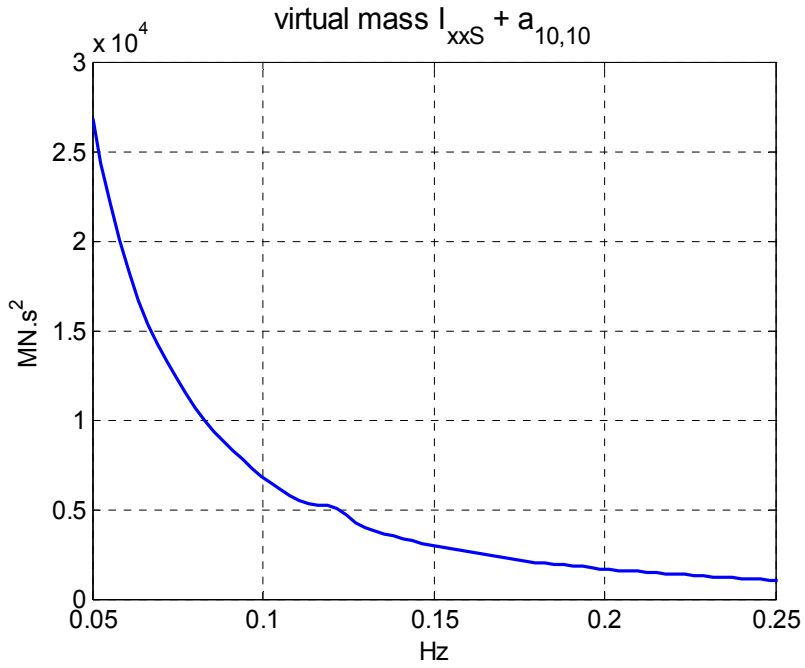

Figure 4.20 Virtual mass coefficient $\left(I_{xx_S} + a_{10,10}\right)(f)$, ship roll case, 0° heading.

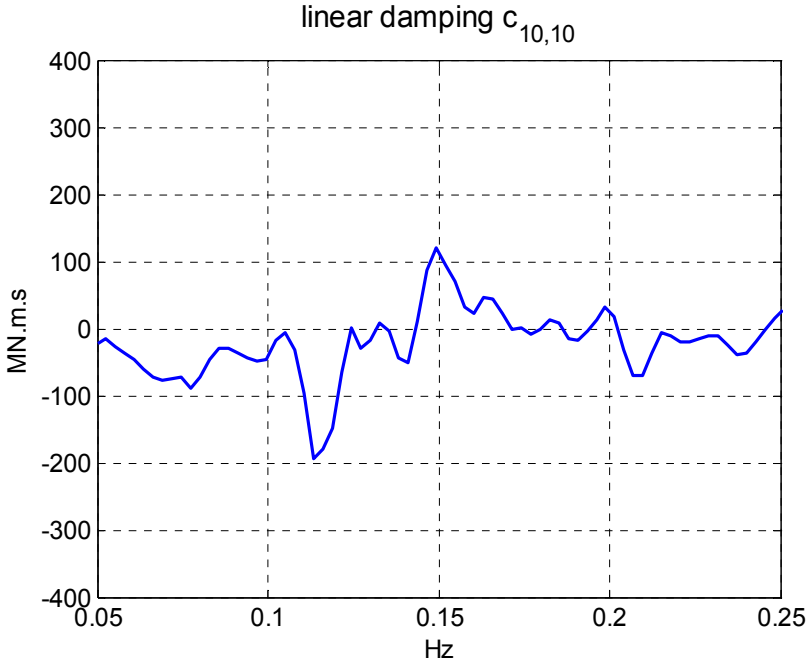

Figure 4.21 Linear damping coefficient $c_{10,10}(f)$, ship roll case, 0° heading.

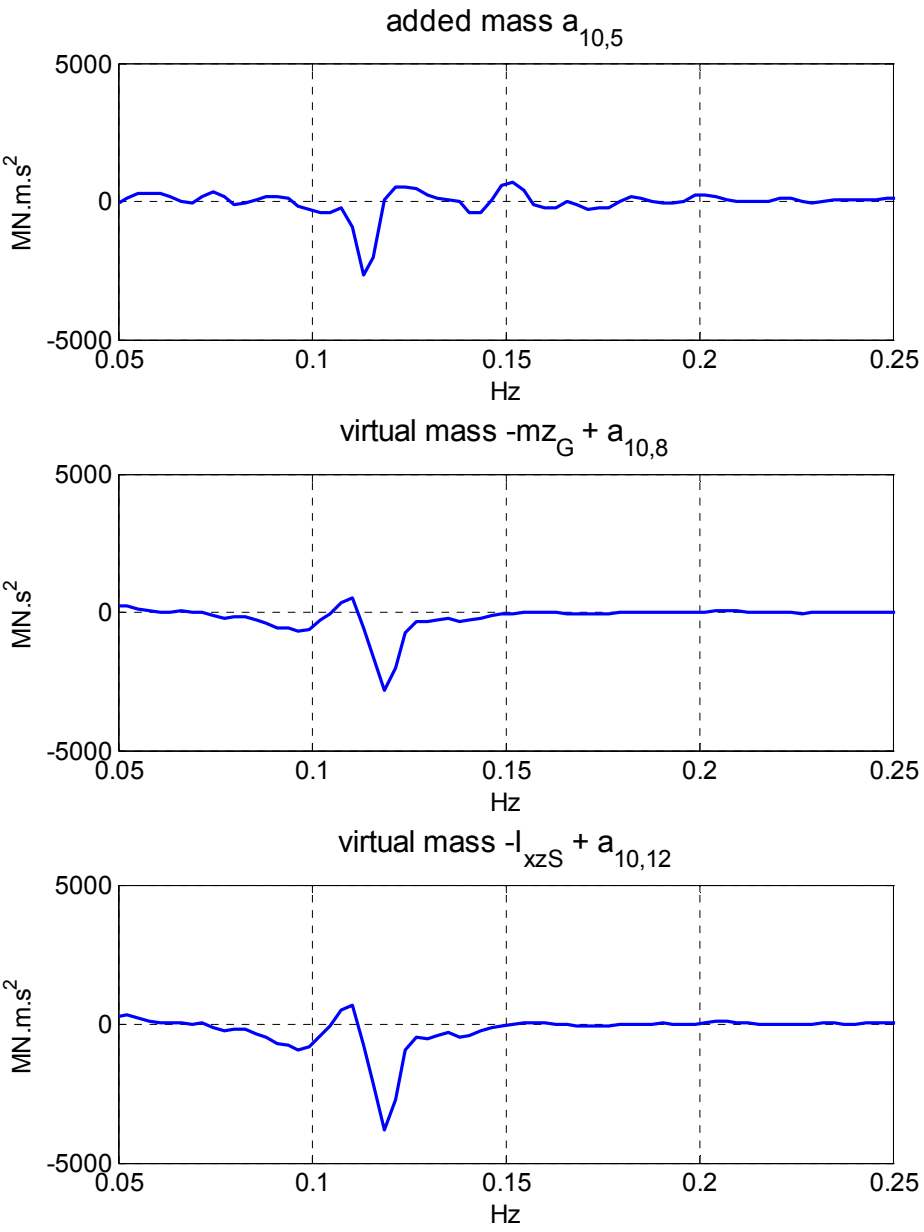

Figure 4.22 Added mass and virtual mass coefficients of the cross coupling terms, ship roll case, 0˚ heading.

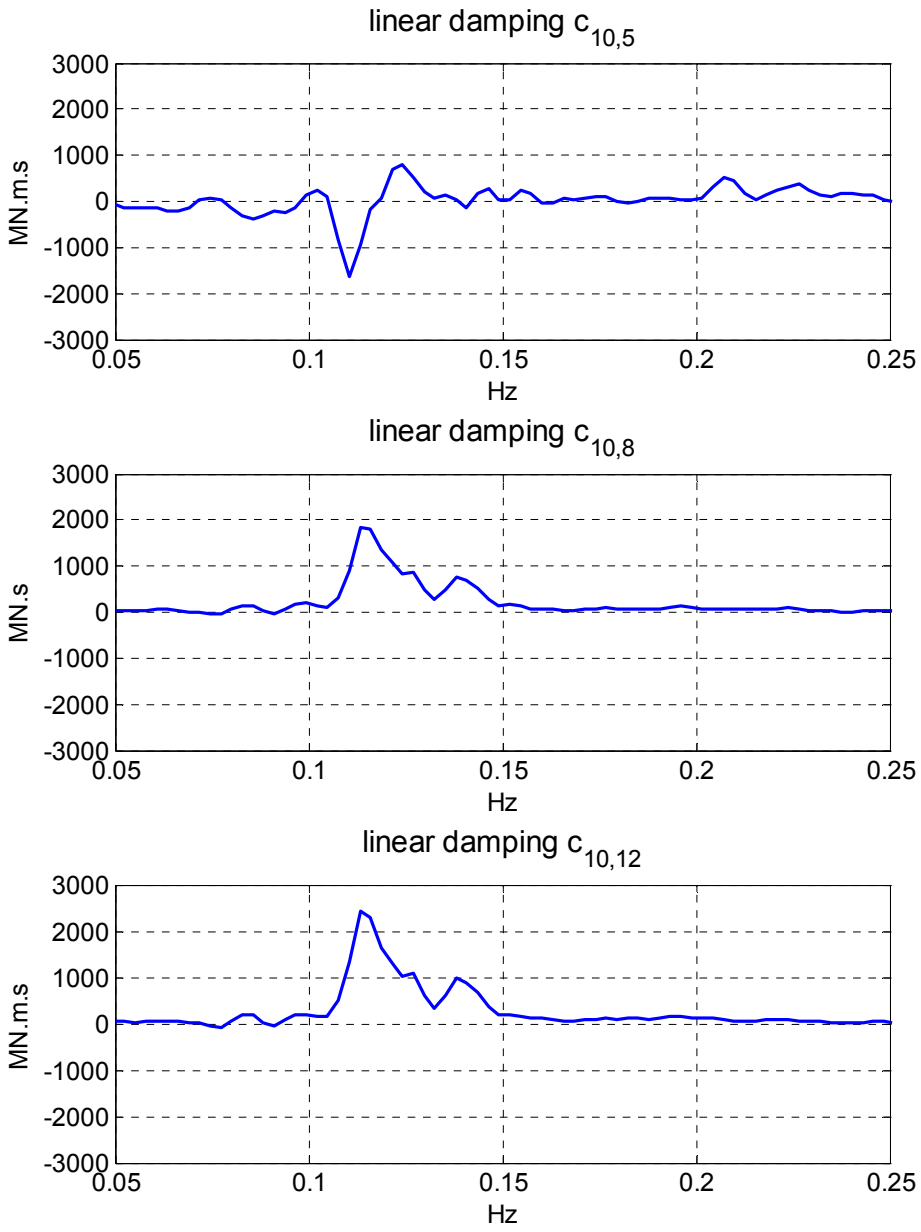

Figure 4.23 Linear damping coefficients of the cross coupling terms, ship roll case, 0˚ heading.

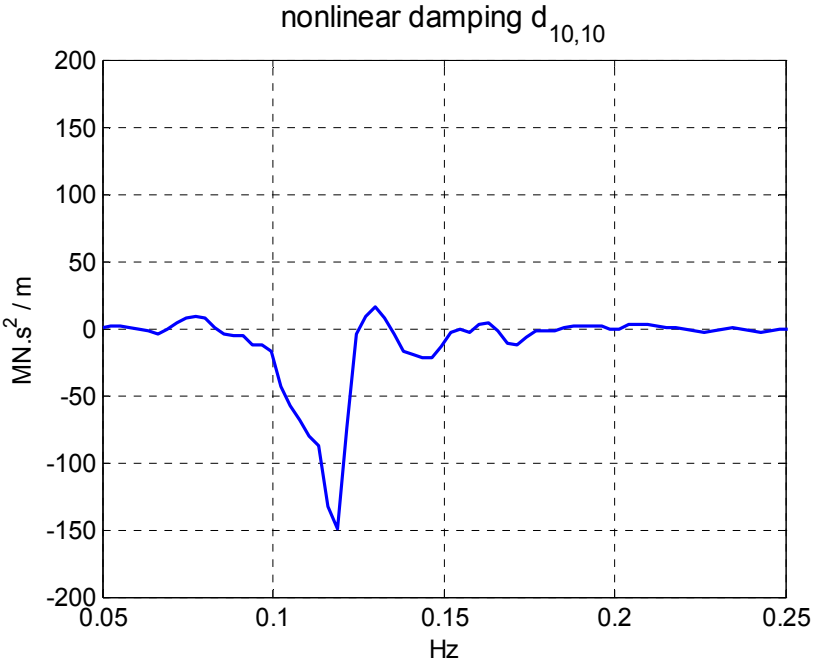

Figure 4.24 Nonlinear damping coefficient, ship roll case, 0˚ heading.

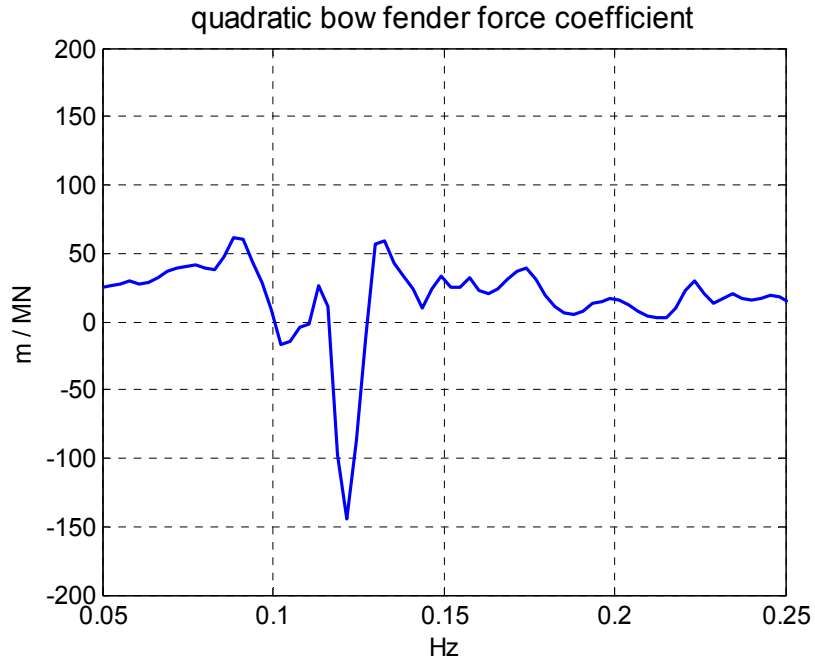

Figure 4.25 Quadratic fender force coefficients, ship roll case, 0˚ heading.

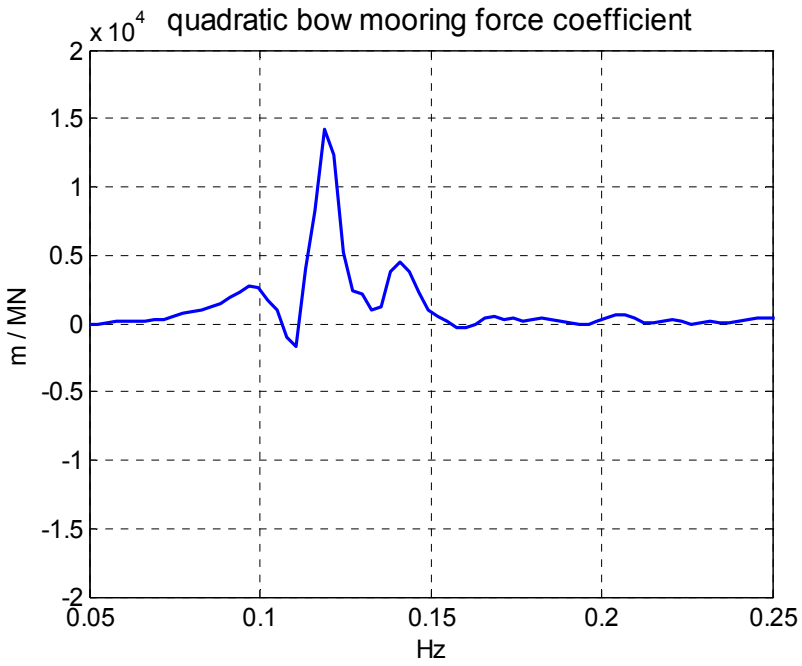

Figure 4.26 Quadratic mooring line force coefficients, ship roll case, 0˚ heading.

4.2.3 Ship heave in head and quartering seas

The last case study is concentrated on the ship heave which is a translational movement unlike the pitch and roll motions studied earlier. All the three heading conditions were considered: the head seas at 0˚ heading, the quartering seas at 45˚ heading where the ship is exposed to the incident wave and the quartering seas at -45˚ where the ship is partly shielded from the incident wave by the barge.

Based on Table 4.1, the simplified equation of motion is slightly different depending on the heading condition. For the 0˚ and the -45˚ headings, the cross-coupling terms that are deemed to be important include those relate the ship heave motion to the barge pitch and ship pitch motions. The corresponding equation of motion is:

$$\begin{aligned}
&\int_0^t a_{9,5}(\tau)\ddot{\theta}_B(t-\tau)d\tau + \int_0^t c_{9,5}(\tau)\dot{\theta}_B(t-\tau)d\tau \\
&+\int_0^t \left(m + a_{9,9}\right)(\tau)\ddot{z}_S(t-\tau)d\tau + \int_0^t c_{9,9}(\tau)\dot{z}_S(t-\tau)d\tau + k_{9,9}z_S(t) \\
&+\int_0^t a_{9,11}(\tau)\ddot{\theta}_S(t-\tau)d\tau + \int_0^t c_{9,11}(\tau)\dot{\theta}_S(t-\tau)d\tau \\
&+\int_0^t d_{9,9}(\tau)\left[\dot{z}_S(t-\tau) - \dot{w}(t-\tau)\right]\left|\dot{z}_S(t-\tau) - \dot{w}(t-\tau)\right|d\tau \\
&+\int_0^t r_{9,9}(\tau)z_S(t-\tau)\left|z_S(t-\tau)\right|d\tau \\
&= F_z(t)
\end{aligned} \tag{4.41}$$

With the usual quadratic relative vertical velocity term $\left[\dot{z}_B(t) - \dot{w}(t)\right]\left|\dot{z}_B(t) - \dot{w}(t)\right|$ and the quadratic displacement $z_S(t)\left|z_S(t)\right|$ as the nonlinear damping and the nonlinear stiffness terms for time being.

In the -45˚ heading condition however, the ship surge motion will also be important and should be added to the equation of motion. Thus this last one becomes:

$$\begin{aligned}
&\int_0^t a_{9,5}(\tau)\ddot{\theta}_B(t-\tau)d\tau + \int_0^t c_{9,5}(\tau)\dot{\theta}_B(t-\tau)d\tau \\
&+\int_0^t a_{9,7}(\tau)\ddot{x}_S(t-\tau)d\tau + \int_0^t c_{9,7}(\tau)\dot{x}_S(t-\tau)d\tau \\
&+\int_0^t \left(m + a_{9,9}\right)(\tau)\ddot{z}_S(t-\tau)d\tau + \int_0^t c_{9,9}(\tau)\dot{z}_S(t-\tau)d\tau + k_{9,9}z_S(t) \\
&+\int_0^t a_{9,11}(\tau)\ddot{\theta}_S(t-\tau)d\tau + \int_0^t c_{9,11}(\tau)\dot{\theta}_S(t-\tau)d\tau \\
&+\int_0^t d_{9,9}(\tau)\left[\dot{z}_S(t-\tau) - \dot{w}(t-\tau)\right]\left|\dot{z}_S(t-\tau) - \dot{w}(t-\tau)\right|d\tau \\
&+\int_0^t r_{9,9}(\tau)z_S(t-\tau)\left|z_S(t-\tau)\right|d\tau \\
&= F_z(t)
\end{aligned} \tag{4.42}$$

Figure 4.30 shows the spectral densities of the mathematical input ship heave and the mathematical output ship heave force, [0.05Hz, 0.25Hz] remains the frequency range of interest. It can be seen that the quantities related to the -45 degree heading are much larger because the ship is exposed to the incident wave, for this reason both the input and the output for this heading are well excited in the wave frequencies. The 45 degree heading where the ship is partly shielded has the lowest energy concentration.

The goodness-of-fit of the initial models were plotted in Figure 4.31. Overall they are quite satisfying, especially the one for the -45 degree heading. Different combinations of nonlinear terms were tested and it turns out that the quadratic mooring line forces are once again important, especially for the 0 degree and the -45 degree headings as can be seen in Figure 4.32. They can provide up to 20% of the total coherence for certain frequencies. In the 45 degree case, the mooring line forces provide smaller additional coherence. However the ship roll motion, when taken into account, can add 25% coherence around the resonance frequency. Normally the ship roll motion is not coupled with the ship heave motion considering the geometrical form of the ship. But the

coherence function states clearly the important influence of the roll motion on the heave motion. Since in the 45 degree configuration the ship is largely exposed to the incident wave, its motions are more important compared to those observed in the other configurations. These relatively large motions can cause green water on the deck whose impact may lead to an asymmetry of the ship motion and consequently makes the ship heave / roll cross-coupling important. On the other hand, a milder excitation in the other headings does not present the risk of green water and thus keep the heave motion independent from the roll motion. The individual contribution of each input for the three heading configurations can be found in Figure 4.33, 4.34 and 4.35.

Including the quadratic mooring line forces, the final equation of motion of the 0 degree and -45 degree headings is:

$$
\begin{aligned}
&\int_0^t a_{9,5}(\tau)\ddot{\theta}_B(t-\tau)d\tau + \int_0^t c_{9,5}(\tau)\dot{\theta}_B(t-\tau)d\tau \\
&+\int_0^t \left(m + a_{9,9}\right)(\tau)\ddot{z}_S(t-\tau)d\tau + \int_0^t c_{9,9}(\tau)\dot{z}_S(t-\tau)d\tau + k_{9,9}z_S(t) \\
&+\int_0^t a_{9,11}(\tau)\ddot{\theta}_S(t-\tau)d\tau + \int_0^t c_{9,11}(\tau)\dot{\theta}_S(t-\tau)d\tau \\
&+\int_0^t d_{9,9}(\tau)\left[\dot{z}_S(t-\tau) - \dot{w}(t-\tau)\right]\left|\dot{z}_S(t-\tau) - \dot{w}(t-\tau)\right|d\tau \\
&+\int_0^t r_{9,9}(\tau)z_S(t-\tau)\left|z_S(t-\tau)\right|d\tau \\
&+\int_0^t l_{B1}(\tau)BL1(t-\tau)\left|BL1(t-\tau)\right|d\tau + \int_0^t l_{B2}(\tau)BL2(t-\tau)\left|BL2(t-\tau)\right|d\tau \\
&+\int_0^t l_{S1}(\tau)SL1(t-\tau)\left|SL1(t-\tau)\right|d\tau + \int_0^t l_{S2}(\tau)SL2(t-\tau)\left|SL2(t-\tau)\right|d\tau \\
&= F_z(t)
\end{aligned}
\tag{4.43}
$$

(a)

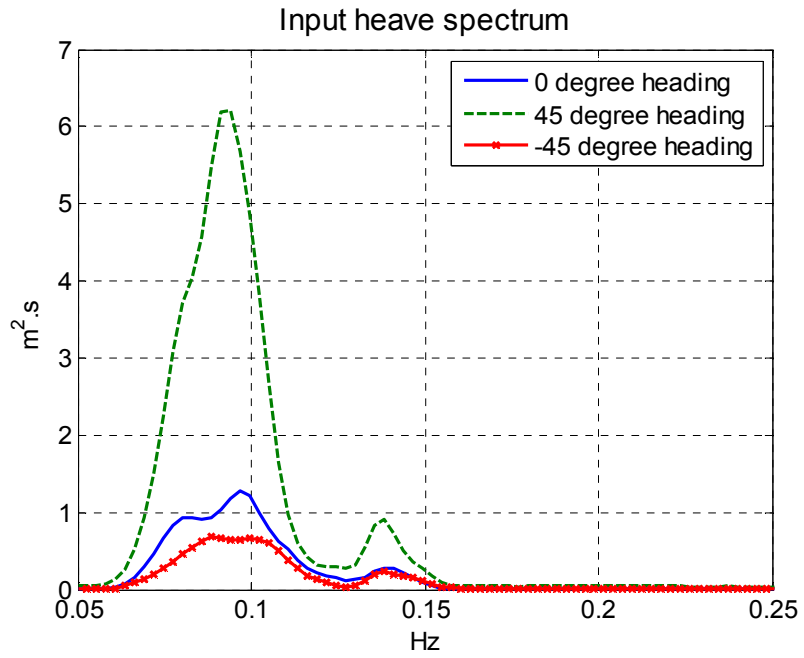

(b)

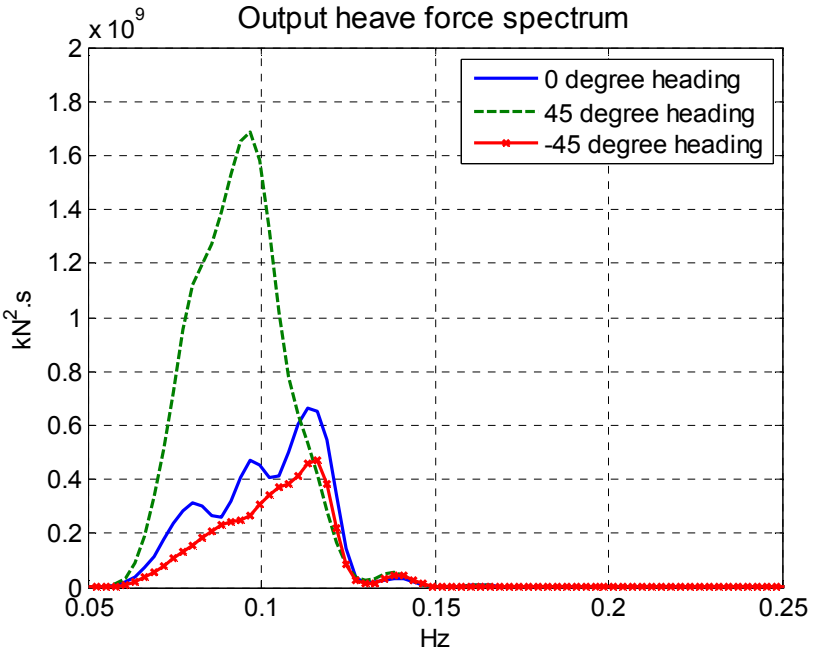

Figure 4.27 Auto-spectral densities of (a) the input ship heave $z_S(t)$, and (b) the output ship heave force $F_z(t)$, in head and quartering seas.

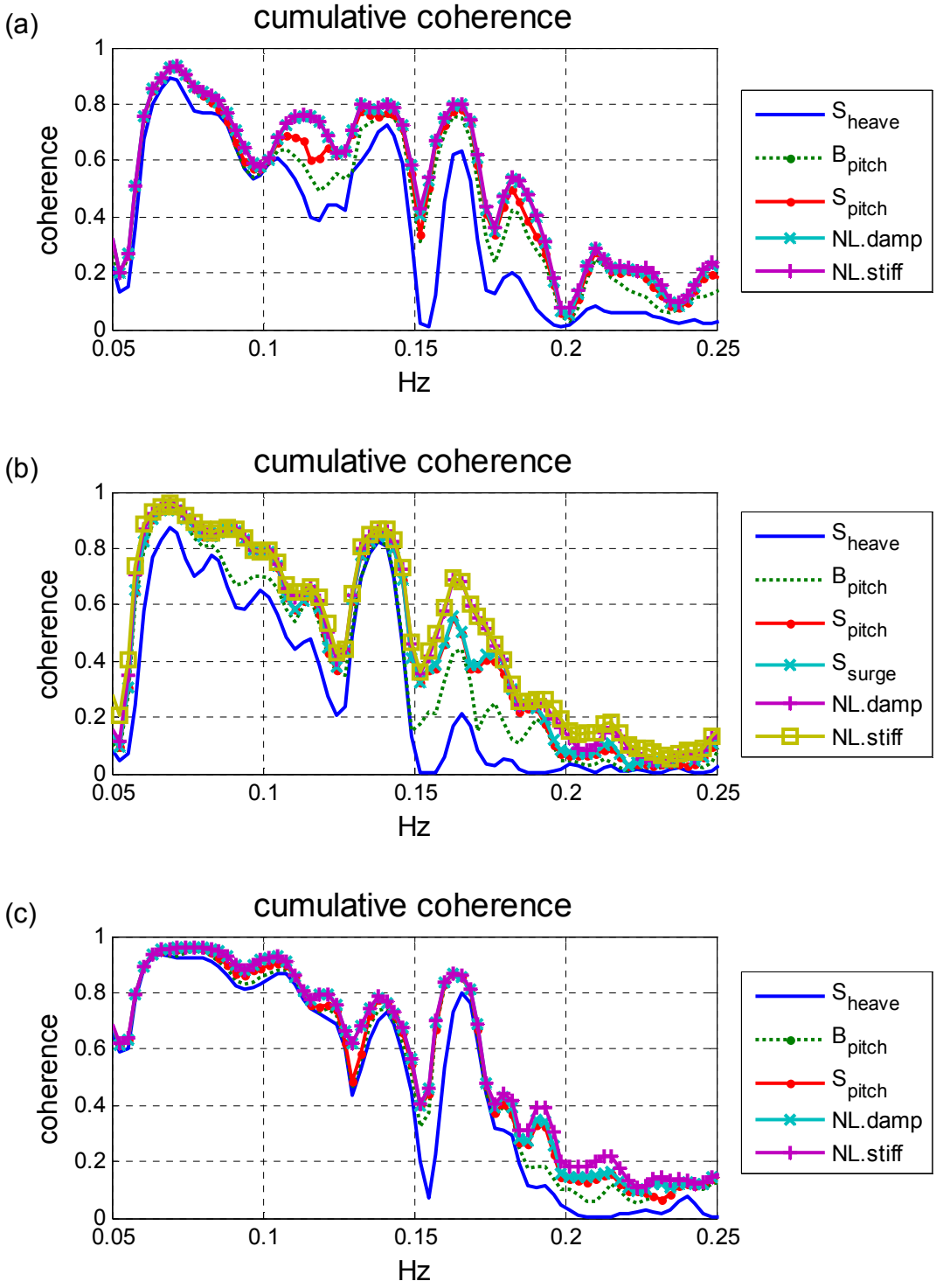

Figure 4.28 Goodness-of-fit of the initial model, ship heave case, in (a) 0˚ heading, (b) 45˚ heading, and (c) -45˚ heading.

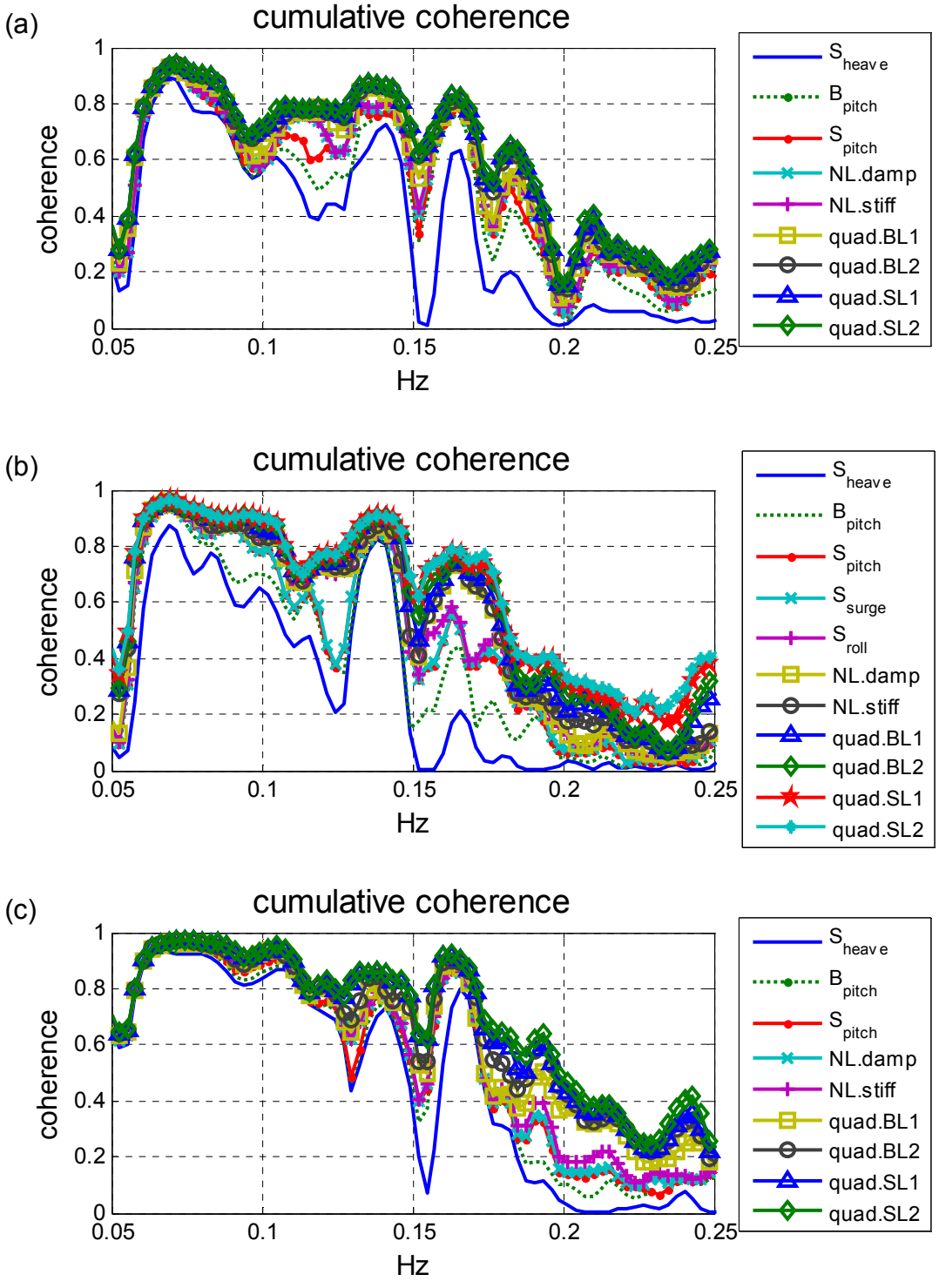

Figure 4.29 Goodness-of-fit of the final model, ship heave case, in (a) 0˚ heading, (b) 45˚ heading, and (c) -45˚ heading.

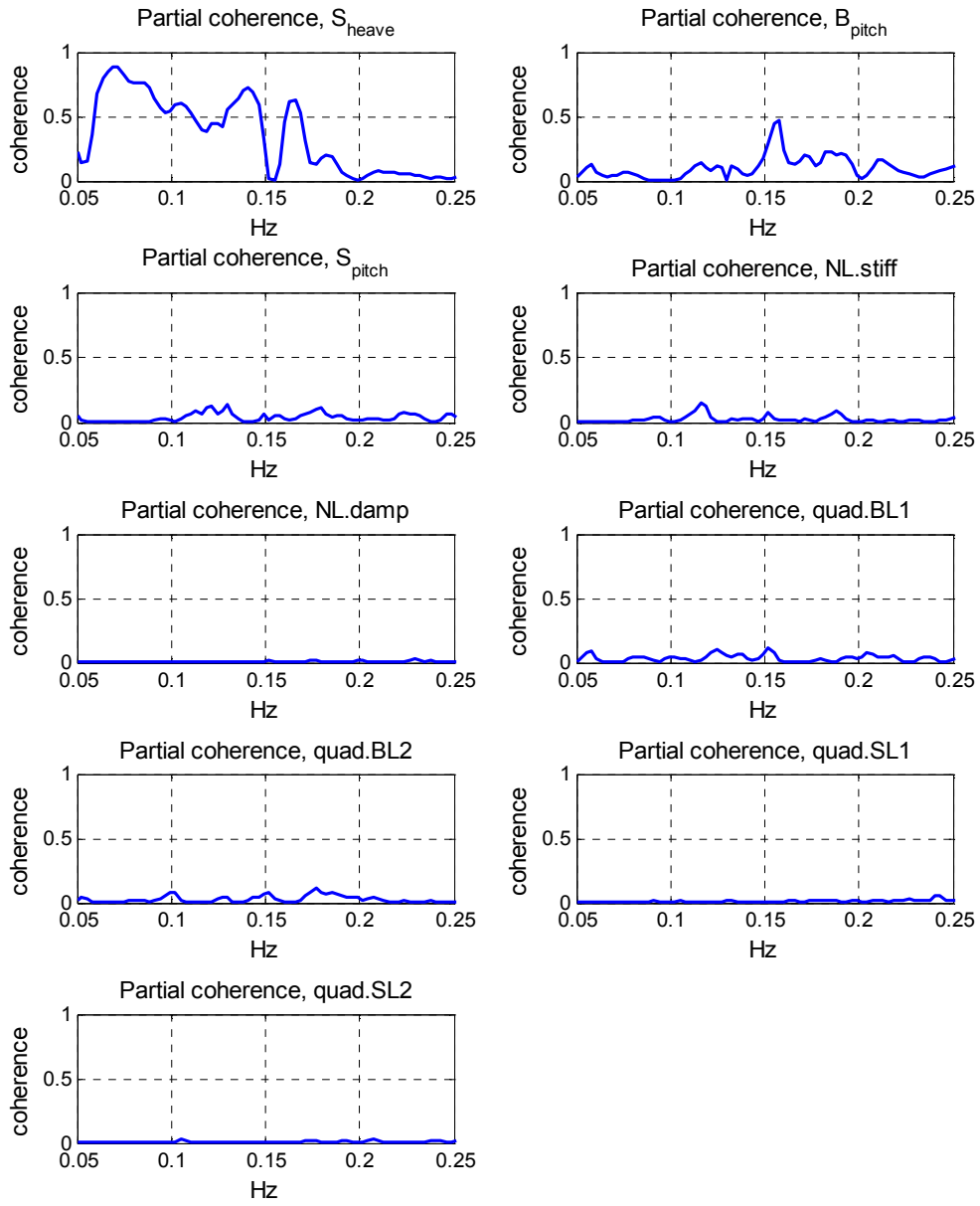

Figure 4.30 Partial coherence functions of the inputs, ship heave case, 0˚ heading.

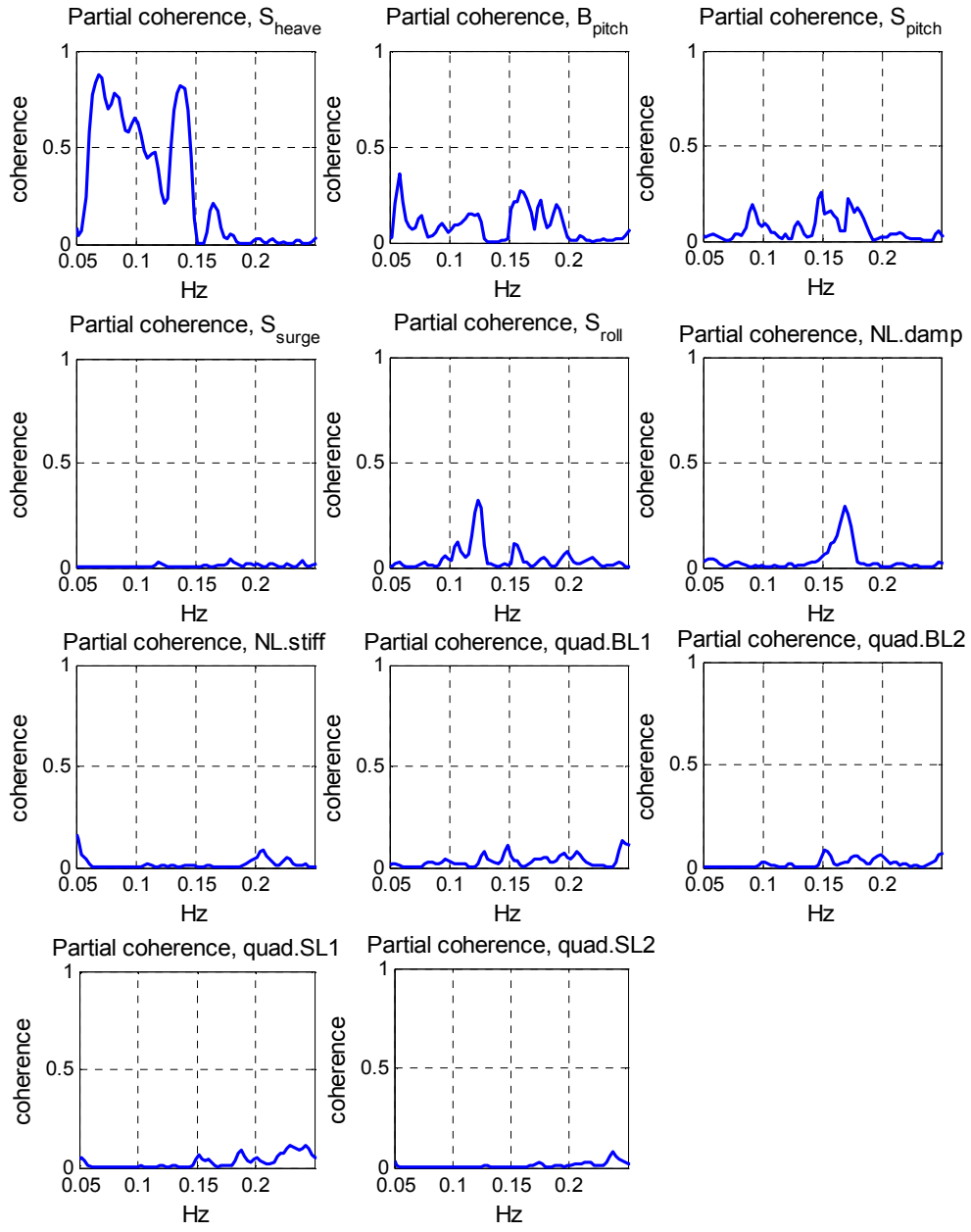

Figure 4.31 Partial coherence functions of the inputs, ship heave case, 45˚ heading.

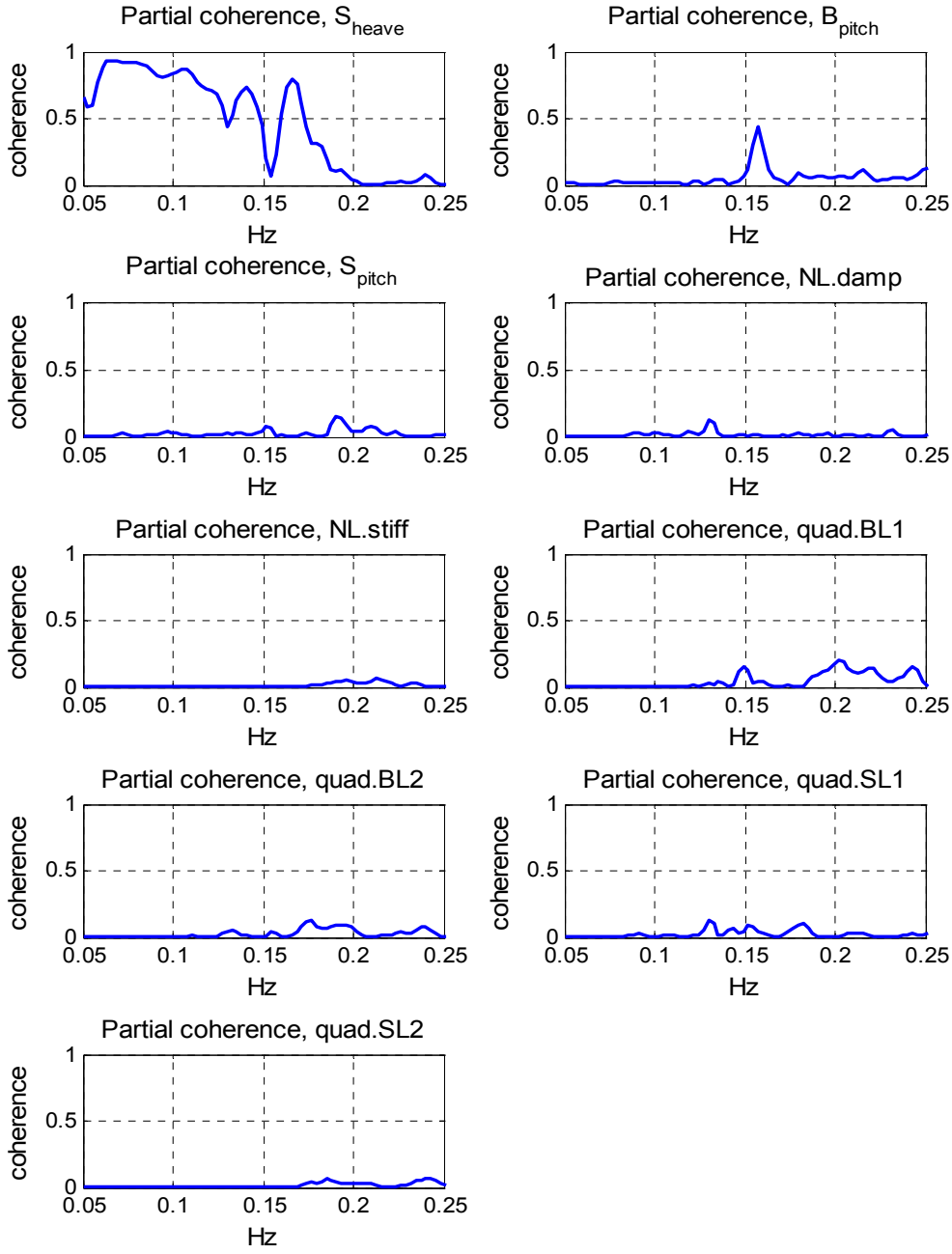

Figure 4.32 Partial coherence functions of the inputs, ship heave case, -45˚ heading.

Whereas the equation of motion for the 45 degree heading configuration is:

$$\begin{aligned}
&\int_0^t a_{9,5}(\tau)\ddot{\theta}_B(t-\tau)d\tau + \int_0^t c_{9,5}(\tau)\dot{\theta}_B(t-\tau)d\tau \\
&+\int_0^t a_{9,7}(\tau)\ddot{x}_S(t-\tau)d\tau + \int_0^t c_{9,7}(\tau)\dot{x}_S(t-\tau)d\tau \\
&+\int_0^t \left(m+a_{9,9}\right)(\tau)\ddot{z}_S(t-\tau)d\tau + \int_0^t c_{9,9}(\tau)\dot{z}_S(t-\tau)d\tau + k_{9,9}z_S(t) \\
&+\int_0^t a_{9,10}(\tau)\ddot{\phi}_S(t-\tau)d\tau + \int_0^t c_{9,10}(\tau)\dot{\phi}_S(t-\tau)d\tau \\
&+\int_0^t a_{9,11}(\tau)\ddot{\theta}_S(t-\tau)d\tau + \int_0^t c_{9,11}(\tau)\dot{\theta}_S(t-\tau)d\tau \\
&+\int_0^t d_{9,9}(\tau)\left[\dot{z}_S(t-\tau)-\dot{w}(t-\tau)\right]\left|\dot{z}_S(t-\tau)-\dot{w}(t-\tau)\right|d\tau \\
&+\int_0^t r_{9,9}(\tau)z_S(t-\tau)\left|z_S(t-\tau)\right|d\tau \\
&+\int_0^t l_{B1}(\tau)BL1(t-\tau)\left|BL1(t-\tau)\right|d\tau + \int_0^t l_{B2}(\tau)BL2(t-\tau)\left|BL2(t-\tau)\right|d\tau \\
&+\int_0^t l_{S1}(\tau)SL1(t-\tau)\left|SL1(t-\tau)\right|d\tau + \int_0^t l_{S2}(\tau)SL2(t-\tau)\left|SL2(t-\tau)\right|d\tau \\
&=F_z(t)
\end{aligned} \tag{4.44}$$

Note that although both the ship roll and the ship surge motions are only important for the 45 degree heading in this example, the reasons of their presence are different. The ship roll as explained is caused by the green water and it should have been otherwise independent from the ship heave motion. The ship surge motion is however coupled with the ship heave motion by geometry, it is only present in the 45 degree case because its interaction effect is deemed to be negligible for the other two headings.

The R-MISO identification procedure is the same as the one described in sections 4.2.1 and 4.22 and the hydrodynamic parameters were estimated. The coefficient directly identified using the R-MISO method is the virtual mass coefficient $m+a_{9,9}$. In this case the virtual mass involves directly the mass of the ship unlike in the previous cases where moments of inertia were involved. The mass can be calculated based on the displaced volume, it is roughly estimated to be 30500 ton. This allows the direct display of the

added mass coefficient $a_{9,9}$ in Figure 4.36 which makes it easier to compare this value with the other added mass coefficients. The curves of $a_{9,9}$ are similar for the three configurations, with the one for the -45 degree heading slightly smaller. The diagonal linear damping coefficient $c_{9,9}$ is shown in Figure 4.37, the damping is higher in the -45 degree heading near the resonance frequencies but they all eventually converge towards zero for higher frequencies. No important negative values are observed for either the added mass or the linear damping coefficients.

The cross-coupling added mass and linear damping coefficients are plotted in respectively Figures 4.38 and 4.39. The ship heave / ship surge and the ship heave / ship roll interactions are only studied for the 45 degree heading. The coefficients $a_{9,5}$ and $c_{9,5}$ are quite small and oscillates around zero for the -45 degree shielding configuration, showing that the pitch motion of the exposed barge has a small influence on the heave motion of the shielded ship. The other added mass coefficients all have tendency to decrease (or increase if most negative) converge toward zero. The cross-coupling damping term $c_{9,11}$ is most important in the head seas because the ship pitch motion is more excited in this configuration.

The nonlinear damping coefficient, the nonlinear stiffness coefficient and the quadratic mooring line force coefficient are shown in Figures 4.40, 4.41 and 4.42. It seems that these values are higher in the head seas, probably because the gap wave effect is the most pronounced in that configuration.

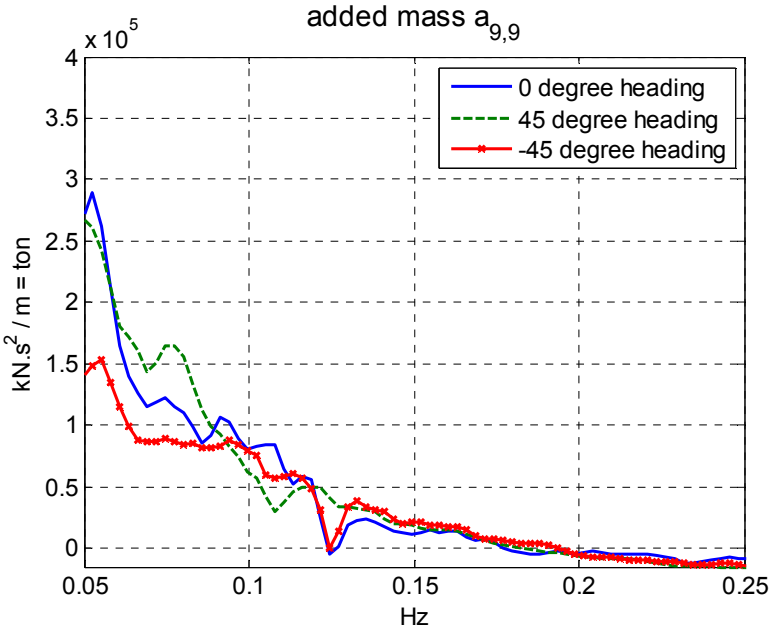

Figure 4.33 Added mass coefficient $a_{9,9}(f)$, ship heave case, head and quartering seas.

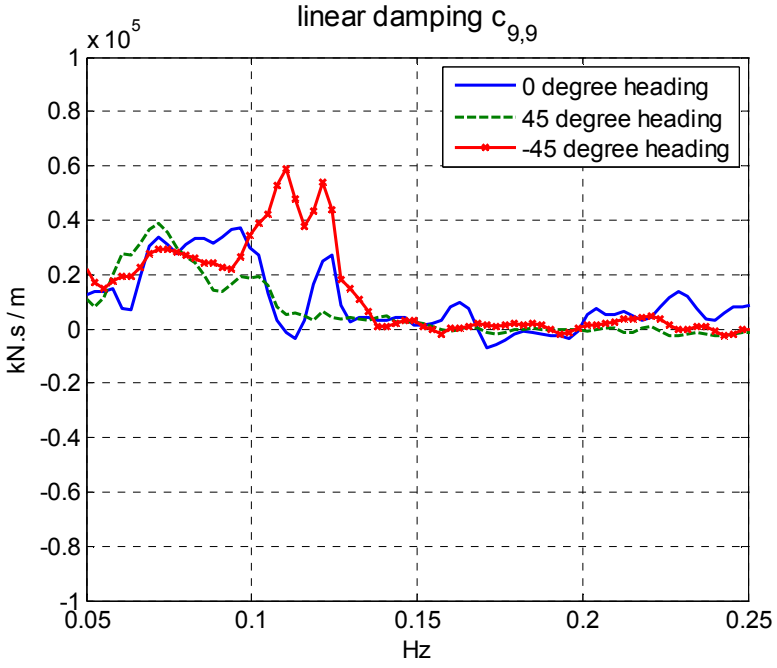

Figure 4.34 Linear damping coefficient $c_{9,9}(f)$, ship heave case, head and quartering seas.

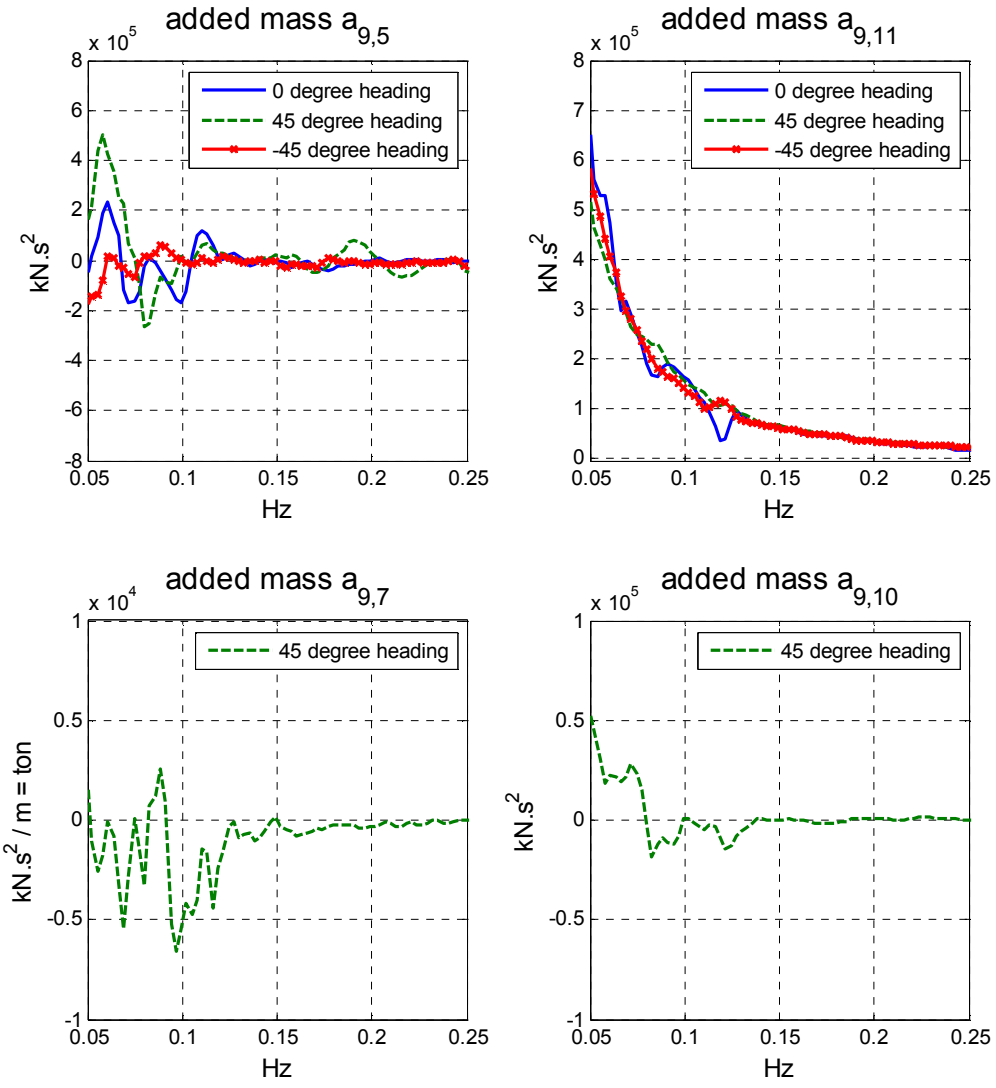

Figure 4.35 Added mass coefficients of the cross coupling terms, ship heave case, head and quartering seas.

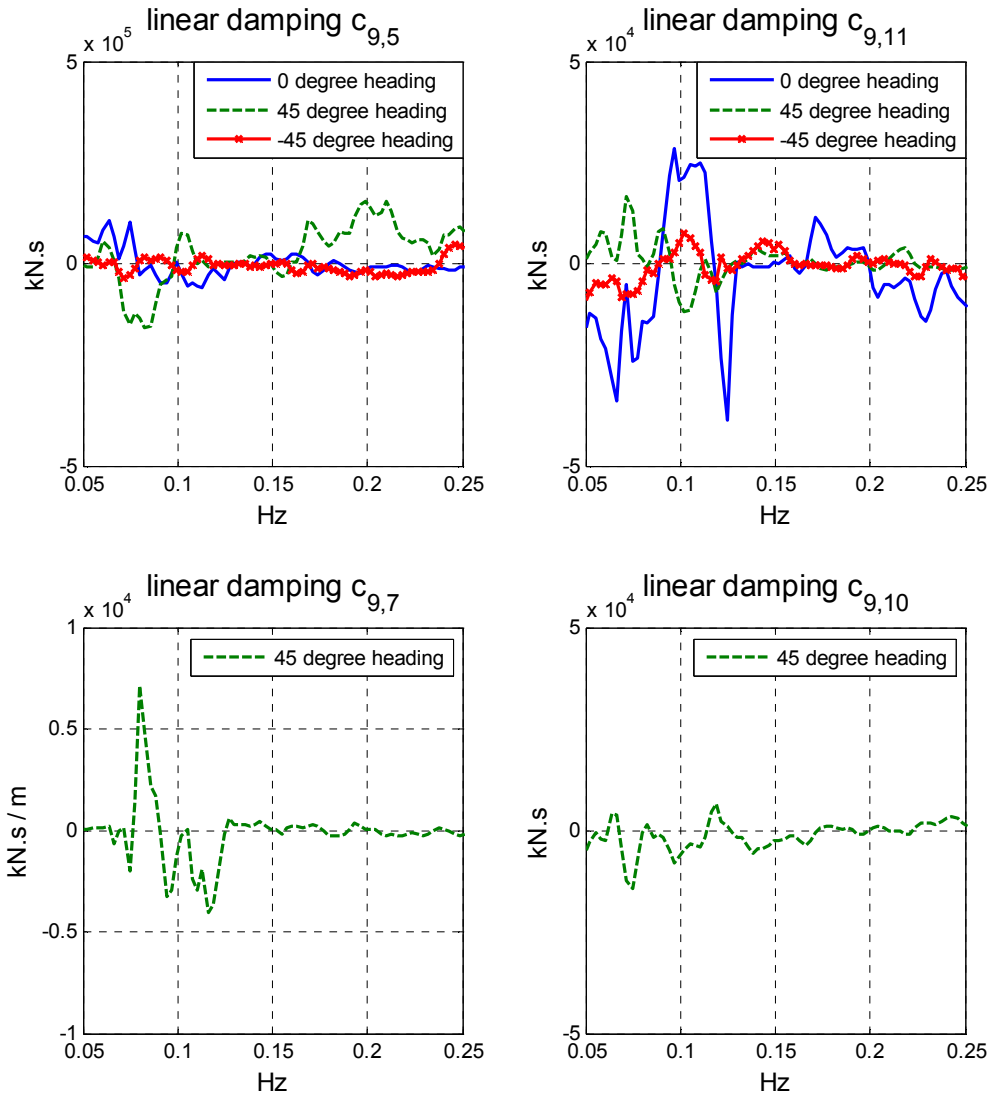

Figure 4.36 Linear damping coefficients of the cross coupling terms, ship heave case, head and quartering seas.

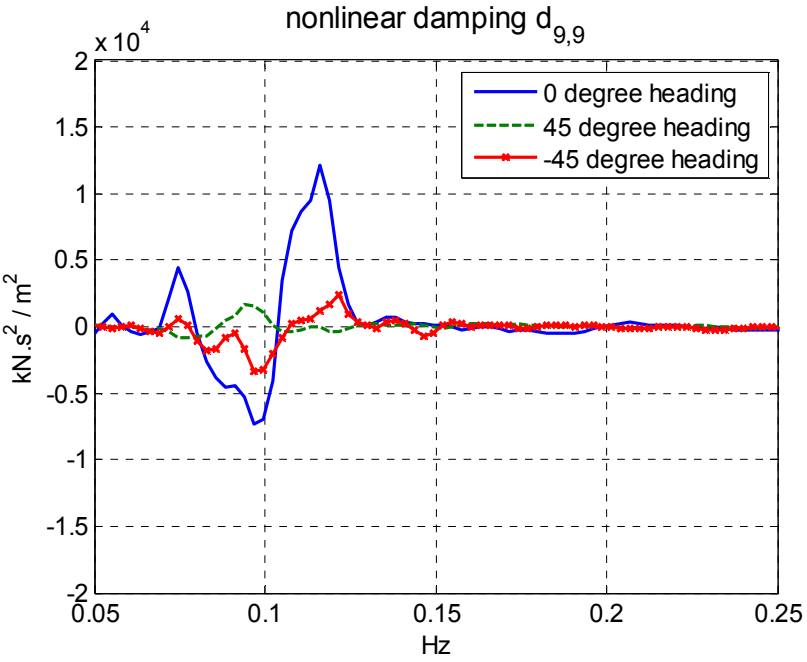

Figure 4.37 Nonlinear damping coefficient, ship heave case, head and quartering seas.

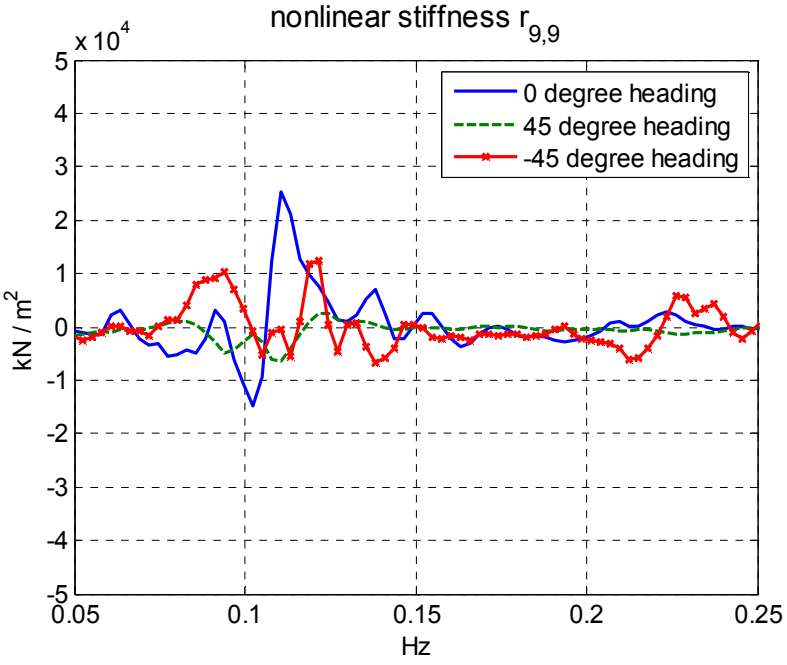

Figure 4.38 Nonlinear stiffness coefficient, ship heave case, head and quartering seas.

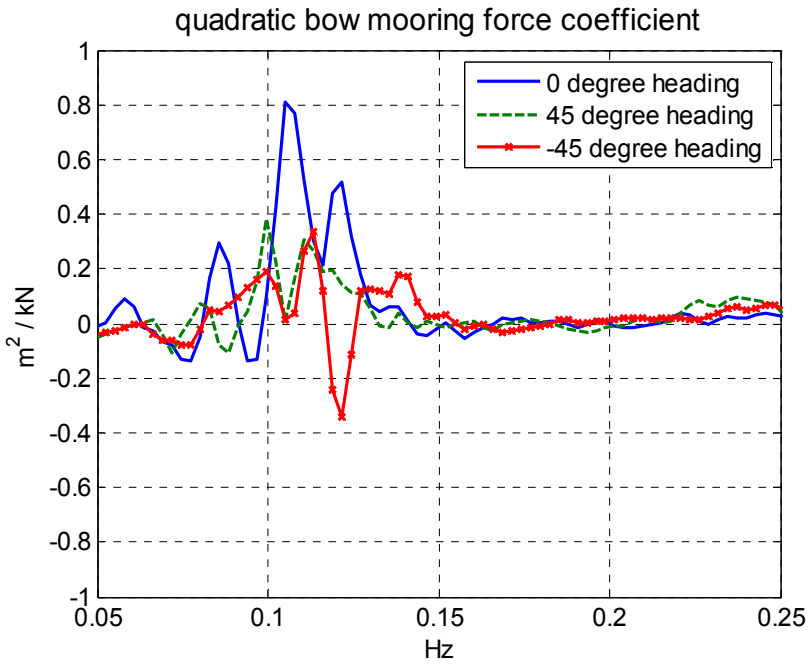

Figure 4.39 Quadratic mooring line force coefficients, ship heave case, head and quartering seas.

5. SUMMARY AND CONCLUSION

The response behavior of a two-body hydrodynamic problem was studied in detail for the case of a ship moored to a fixed barge that was subject to random sea conditions for three different headings. Previously used for single body systems, the R-MISO method was extended in this research study to address this specific class of two-body systems. The ship was equipped with tanks that could be filled with liquid to specified levels. A statistical analysis was initially performed to provide an overview of the general response behavior of the system and to detect the possible nonlinearities that might present. This two-body hydrodynamic problem was formulated using an integro-differential equation approach to develop the equations of motion. The formulation was quite general in that it allowed for the inclusion of linear and nonlinear terms that might be postulated to significantly influence the physical behavior of either vessel. The Reverse Multi-Input / Single Output (R-MISO) system identification method was then applied to estimate the detailed information about the frequency dependent hydrodynamic parameters. In the R-MISO method, the roles of the physical input and outputs in the mathematical model are reversed in order to eliminate the feedback terms usually associated with nonlinear systems.

The various time series were characterized using statistical parameters, spectral densities and linear coherence functions, with the objective of gaining insight into the general nature of the linear and nonlinear response behavior of this ship and barge system. The orientation of the physical models was varied with respect to the incident random waves and was intended to explore the effects of wave conditions in the gap between the two vessels and shielding effects by the barge. The model headings included head seas and two quartering sea conditions (45 and -45 degrees). In addition, the effects of 80% and 10% fill levels in the ship-board tanks were introduced in the model test program and were included to provide some preliminary data on the effects on ship motion

characteristics. It was observed that indeed have the fluid level in the ship tanks did have an effect on the ship motion response behavior. The motion amplitude of the ship with 10% fill level was larger compared to that of the 80% fill level and was attributed to the smaller ship draft and the increased sensitivity to the incoming waves. This influence of the fluid level was also observed to vary depending on whether the ship was shielded or on the weather-side. In quartering seas the shielding effect provided by the barge on the lee side ship is only observed to be important when the tanks are at the 10% fill level. For all the configurations considered in this study, it was confirmed that the surge motion was highly correlated with the mooring line forces, and that the fender forces are strongly influenced by the roll motion although this relationship was clearly more nonlinear in nature.

One of its main advantages of the R-MISO methodology is the ability to sort out relevant and irrelevant linear and nonlinear terms through the determination of their contribution and magnitude. This is accomplished first, through the inspection of the partial and cumulative coherence functions of the proposed equations of motion, and secondly by observing the resulting frequency dependent coefficients over a relevant energetic frequency range. For the single barge configuration it was shown that the equation of motion, which included commonly used nonlinear terms, worked quite well and this provided a base case for later comparisons. Further, when the ship was moored to the barge the inclusion of the nonlinearities terms related to the mooring and fender forces was shown to provide a better description of the system. The research study was focused upon three case studies that examined the barge pitch, ship roll and ship heave motions. Consistent with the observations made form the initial investigation of the data using statistical analysis, the mooring line forces had an impact on the pitch motion through its coupling with the surge motion, whereas the fender forces impact was more evident in the study of the roll motions. It was observed that the large roll motions measured in head seas was related to the pumping mode of the waves trapped between the two vessels. This was manifested in the R-MISO results as negative added-mass and

damping coefficients. The frequency dependent parameters were observed to vary somewhat depending on the heading conditions. In the configuration where the ship was exposed to head seas, the R-MISO analysis confirmed the video observation that green water was present on the ship. This R-MISO method results provided insight into the related interactions between the ship roll and the ship heave motions that would not have been quantified using video findings alone.

During the application of the R-MISO method to the ship and barge two-body system, several challenges specific to two-body problems were encountered. First, considerably more data preparation is required. More specifically, quantities such as mooring line and fender forces play an important role in influencing the two-body motion behavior and in order to include these force components in the analysis, it is necessary to decompose these time series as detailed in Appendix D. Further, the geometry of the vessels and the cross-coupling effects between the motions significantly influence the level of complexity of the problem. It is time consuming to compute all the cross-coupling terms, of which, unfortunately, many are not physically important. Often some of these terms can be neglected by recognizing geometric symmetries. For the remaining terms, this study introduced the use of total energy of the different motion interactions to determine the dominant terms. The objective was to simplify the problem and consequently reduce the computation load while conserving the accuracy of the model. The energy was computed using the zero-th moment of the cross-spectral densities. It was specifically demonstrated how one could select a threshold value below which the cross-coupling effects can be considered to be negligible. The appropriate threshold value for the experimental data used in this study was determined through sensitivity tests, meaning that the final cumulative coherence of the equation of motion remains relatively undisturbed when the presumably negligible cross-coupling terms are removed. A non-dimensional threshold value would be preferable since the different units of the zero-th moments can make the comparison difficult. The issue of interpreting the frequency dependant values was also was also discussed because the

hydrodynamic and mechanical interactions that exist between two-bodies lead to frequency dependant values that can be quite different from a single body case. For instance in the for this two-body system, negative parameters were observed due to the gap wave pumping motions, and parameter dependence on vessel heading.

To validate the R-MISO results, the parameter values estimated were substituted back into the equation of motion and the mathematical outputs were reconstituted. Compared with the measured data for the two body configuration, the matching is quite good in terms of periodicity but a discrepancy in amplitudes of the forces and moments was observed. Overall these comparisons appear to be somewhat less accurate than in the single body case. The errors were believed to be the result of several factors that included possible nonlinearities that were overlooked in the model assembly, measurement inaccuracies during model testing, values that had to be estimated such as the linear stiffness coefficients and finally various manipulations of the data including the differentiation and the decomposition of the time series.

The current study was an important step in the development of the R-MISO method for the study of more general multi-body problems. Although the model study was for a realistic system the approximation that the barge was fixed provided a useful simplification to this vey complex hydrodynamic problem. If the barge were itself moored or replaced by a second ship more complicated interactions could be expected but the R_MISO methodology could be applied. It was demonstrated that an initial statistical analysis of the measured time series does provide information that helps one to choose the nonlinear terms that should be included in the equations of motion. Finally, in order to isolate the suspected sources of error and lead to a better understanding of the strengths and limitations of this methodology numerical studies should be pursued.

REFERENCES

Bendat, JS (1990). *Nonlinear System Analysis and Identification from Random Data*, Wiley-Interscience Publication, John Wiley & Sons, Inc, New York, USA.

Bendat, JS (1998). *Nonlinear Systems Techniques and Applications*, Wiley-Interscience Publication, John Wiley & Sons, Inc., New York, USA.

Bendat, JS, Piersol, AG (1982). "Spectral Analysis of Nonlinear Systems Involving Square-Law Operations," *J of Sound and Vibration*, Vol 81, pp 199-213.

Bendat, JS, Palo, PA, Coppolino, RN (1992). "A General Identification Technique for Nonlinear Differential Equations of Motion," *Probabilistic Engineering Mechanics*, Vol 7, pp 43-61.

Bendat, JS, Piersol, AG (1993). *Engineering Applications of Correlation and Spectral Analysis*, Wiley-Interscience Publication, John Wiley & Sons, Inc., New York, USA.

Bendat, JS, Coppolino, RN, Palo, PA (1995). "Identification of Physical Parameters with Memory in Non-linear Systems," *Int J Non-linear Mechanics*, Vol 30, No 6, pp 841-860.

Buchner, B, Van Dijk, AWV, De Wilde, J (2001). "Numerical Multiple-Body Simulations of Side-by-Side Mooring to an FPSO," *Proc. 11th Int Offshore and Polar Eng Conference*, Stavanger, Norway, ISOPE, Vol I, pp 343-353.

Cheng, J, Falzarano, JM (2003). "System Identification of Nonlinear Coupled Ship / Offshore Platform Dynamics in Beam Seas," *Proc 22nd Offshore Mechanics and Arctic Engineering Conf*, Cancun, Mexico, OMAE, Paper No 2003-37336.

Clauss, GF, Jacobsen, K (2005). "Multi-body Systems in Waves – Impact of Hydrodynamic Coupling on Motions," *Proc 12th International Congress of the International Maritime Association of the Mediterranean*, Lisbon, Portugal, IMAM.

Faltinsen, OM (1990). *Sea Loads on Ships and Offshore Structures*, Cambridge University Press, Cambridge, UK.

Falzarano, JM, Cheng, J, Rodrigues, W (2004). "Transit Draft Heave and Pitch Motion Analysis of the Mobile Offshore Base (MOB) Using Reverse MI/SO Techniques," *J of Offshore Mechanics and Arctic Eng*, Vol 126, pp 16-25.

Fournier, JR, Naciri, M, Chen, XB (2006). "Hydrodynamics of Two Side-by-Side Vessels Experiments and Numerical Simulations," *Proc. 16th Int Offshore and Polar Eng Conference*, San Francisco, USA, ISOPE, Vol I, pp 158-165.

Haddara, MR, Xu, J (1998). "On the Identification of Ship Coupled Heave-Pitch Motions Using Neural Networks," *Ocean Engineering*, Vol 26, No.5, pp 381-400.

Huijsmans, RHM, Pinkster, JA, de Wilde, JJ (2001). "Diffraction and Radiation of Waves Around Side-by-Side Moored Vessels," *Proc. 11th Int Offshore and Polar Eng Conference*, Stavanger, Norway, ISOPE, Vol I, pp 406-412.

Imai, H, Yun, CB, Maruyama, O, Shinozuka, M (1989). "Fundamentals of System Identification in Structural Dynamics," *Probabilistic Engineering Mechanics*, Vol 4, No 4, pp 162-173.

Koo, BJ, Kim, MH (2005). "Hydrodynamic Interactions and Relative Motions of Two Floating Platforms with Mooring Lines in Side-by-Side Offloading Operation," *Applied Ocean Research*, Vol 27, pp 292-310.

Lee, SJ, Kim, MH (2008). "The Effects of Tank Sloshing on the Coupled Responses of LNG Vessel and Floating Terminal," *Proc. 18th Int Offshore and Polar Eng Conference*, Vancouver, Canada, ISOPE, Vol III, pp 179-183.

Liagre, PF (2002). *Investigation of Nonlinear System Identification Techniques*, Ph.D. dissertation, Zachry Department of Civil Engineering, Texas A&M University, College Station, USA.

Liagre, PF, Niedzwecki, JM (2003). "Estimating Nonlinear Coupled Frequency-Dependent Parameters in Offshore Engineering," *Applied Ocean Research*, Vol 25, pp 1-19.

Naciri, M, Waals, O, De Wilde, J (2007). "Time Domain Simulations of Side-by-Side Moored Vessels Lessons Learnt from a Benchmark Test," *Proc 26th Int Conf on Offshore Mechanics and Arctic Engineering*, San Diego, USA, OMAE, Paper No 2007-29756.

Narayanan, S, Yim, SCS (2000). "Nonlinear Model Evaluation via System Identification of a Moored Structural System," *Proc. 10th Int Offshore and Polar Eng Conference*, Seattle, USA, ISOPE, Vol III, pp 402-409.

Niedzwecki, JM, Liagre, PF (2003). "System Identification of Distributed-Parameter Marine Riser Models," *Ocean Engineering*, Vol 30, pp 1387-1415.

Niedzwecki, JM (2007). Final report for Advanced Technology Program (ATP), Texas A&M University, College Station, USA.

Ohkusu, M (1976). "Ship Motions in Vicinity of a Structure," *Proc of Int Conf on Behavior of Offshore Structure*, Trondheim, Norway, BOSS, Vol I, pp 284-306.

Rice, HJ, Fitzpatrick, JA (1988). "A Generalised Technique for Spectral Analysis for Non-linear Systems," *Mechanical Systems and Signal Processing*, Vol 2, No.2, pp195-207.

Rice, HJ, Fitzpatrick, JA (1991a). "The Measurement of Nonlinear Damping in Single-Degree-of-Freedom Systems," *J of Vibration and Acoustics*, Vol 113, pp 132-140.

Rice, HJ, Fitzpatrick, JA (1991b). "A Procedure for the Identification of Linear and Non-linear Multi-Degree-of-Freedom Systems," *J of Sound and Vibration*, Vol 149, No.3, pp 397-411.

Rodrigues, W, Falzarano, J (2001). "Transit Draft Heave Motion Analysis of the Mobile Offshore Base (MOB) Using Reverse MI/SO Techniques," *Proc. 11th Int Offshore and Polar Eng Conference*, Stavanger, Norway, ISOPE, Vol I, pp 256-263.

Selvam, RP, Bhattacharyya, SK (2001). "Parameter Identification of a Compliant Nonlinear SDOF System in Random Ocean Waves by Reverse MISO Method," *Ocean Engineering*, Vol 28, pp 1199-1223.

Selvam, RP, Bhattacharyya, SK (2006). "System Identification of a Coupled Two DOF Moored Floating Body in Random Ocean Waves," *Ocean Engineering*, Vol 28, pp 1199-1223.

Taylor, ER, Zietsman, J (1982). "Hydrodynamic loading on multi-component bodies," *Proc of the 3rd Int Conf on Behavior of Offshore Structure*, Cambridge, MA, USA, BOSS, pp 424-443.

Teigen, P, Niedzwecki, JM (1999). "A Computational Study of Wave Effects Related to Side-by-Side LNG Offloading," *Proc. 9th Int Offshore and Polar Eng Conference*, Brest, France, ISOPE, Vol I, pp 347-354.

Teigen, P, Niedzwecki, JM (2006). "A Computational Study of Wave Effects Related to Side-by-Side LNG Offloading," *Proc. 16th Int Offshore and Polar Eng Conference*, San Francisco, USA, ISOPE, Vol I, pp 238-247.

Van der Valk, C, Watson, A (2005). "Mooring of LNG carriers to a weathervaning floater – side-by-side or stern-to-bow," *Proc. Offshore Technology Conference*, Houston, USA, OTC, Paper No 17154.

Van Oortemerssen, G (1981). "Some hydrodynamic aspects of multi-body systems," *Proc of Int Symposium on Hydrodynamics in Ocean Engineering*, Trondheim, Norway, Vol II, pp 725-744.

Varadarajan, NP, Nagarajaiah, S (2008). "Nonlinear System Identification of Offshore Floating Structures," *Proc 27th Int Conf on Offshore Mechanics and Arctic Engineering*, Estoril, Portugal, OMAE, Paper No 2008-57161.

Xie, C, Niedzwecki, JM, Teigen, P (2008a). "Coupled Mini-TLP Barge Response in Random Seas," *Int J of Offshore and Polar Engineering*, Vol 18, No 2, pp 112-119.

Xie, C, Niedzwecki, JM, Teigen, P (2008b). "Hydrodynamic Interaction in a Coupled Ship / Barge System and its Effects on the Mooring Line and Fender Forces," *Proc. 18th Int Offshore and Polar Eng Conference*, Vancouver, Canada, ISOPE, Vol III, pp 330-334.

Yoon, HK, Rhee, KP (2003). "Identification of Hydrodynamic Coefficients in Ship Maneuvering Equations of Motion by Estimation-Before-Modeling Technique," *Ocean Engineering*, Vol 30, pp 2379-2404.

Yun, CB, Shinozuka, M (1980). "Identification of Nonlinear Structural Dynamic Systems," *J of Structure Mechanics,* Vol 8, pp 187–203.

APPENDIX A. CALCULATION OF THE ROTATIONS BASED ON THE DISPLACEMENT DATA

Rigid barge and ship were studied in the present investigation. Due to their important length in the longitudinal direction, some pitch and yaw motions were inevitably observed and needed to be taken into account for the accuracy of the study conducted here. Note that the roll motion can be neglected because it is very small as mentioned in Section 2. For those rigid bodies, only acceleration was measured by accelerometers installed at different locations on board of the barge and the ship. To find the values of the pitch and yaw motions, the acceleration data were integrated twice to recover the displacement data. From the displacement at different locations on the vessel it was then possible to calculate the rotations using trigonometry.

The integration of the acceleration data was performed in frequency domain. Matlab fast Fourier transform (fft) command was used to transform the original time series to frequency domain expression for the integration and the inverse fast Fourier transform (ifft) command was used to convert the data back to time domain representation. For each of the vessels, displacements at four different locations were thus obtained and were used to calculate the pitch and yaw motions. The detailed procedure is listed bellow.

A.1. Rotations of the barge

Figure A.1 shows the location of the accelerometers installed on the barge and the intermediary points A and B which will be used for the calculation. Vertical accelerations were measured at all the points whereas the tangential accelerations were only measured at point 1 and 2.

The pitch motion $\theta(t)$ can be obtained from the vertical displacement information at point A knowing that the center of gravity is fixed. The pitch angle is positive when the displacement at point A is positive according to the polarity indicated in Figure A.2.

$$Z_A = \frac{1}{2}(Z_3 + Z_4) \tag{A.1}$$

$$\theta(t) = \arcsin\left(\frac{Z_A}{\Delta}\right) \times \frac{180}{\pi} \tag{A.2}$$

With

Z_i the vertical displacement at point i.

$\Delta = AO' = BO' = 28.29\,m$

The yaw motion $\psi(t)$ can be approximated by using the radius r of the circle formed by the accelerometers and the tangential displacement d_1 or d_2 as shown by Figure A.3:

$$\psi(t) = \arctan\left(\frac{d_1}{r}\right) \times \frac{180}{\pi} \tag{A.3}$$

With

d_1 = tangential displacement at accelerometer 1

$r = \sqrt{2 \times 28.29^2} \approx 40\,m$

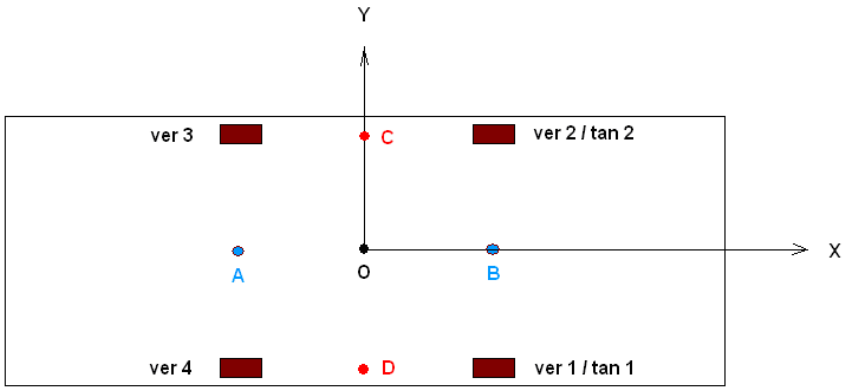

Figure A.1. Position of the accelerometers and the intermediary points on the barge

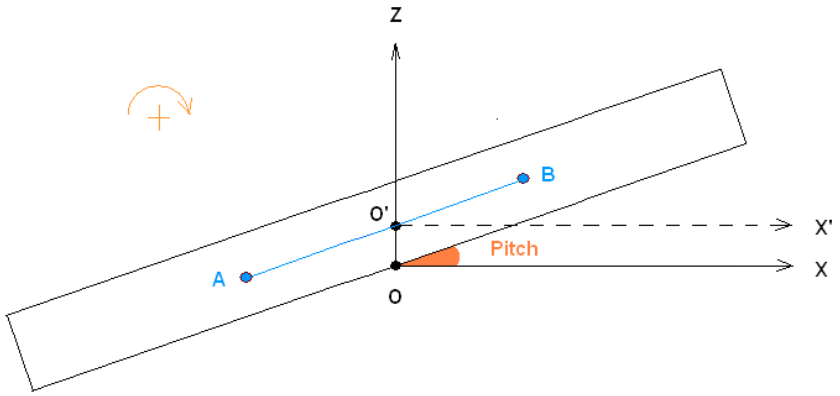

Figure A.2. Pitch angle

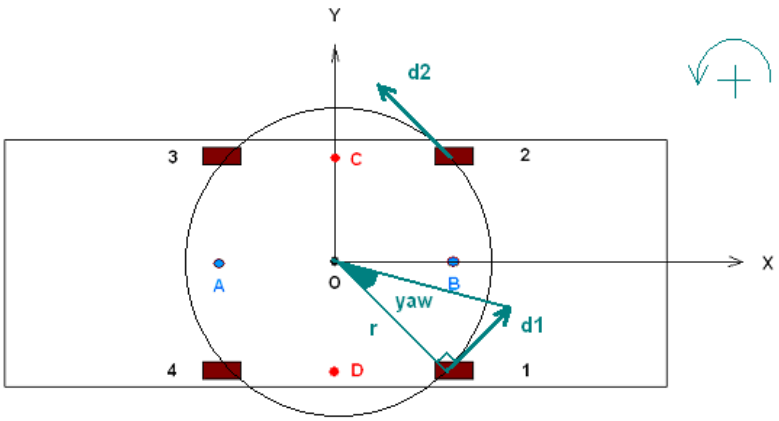

Figure A.3. Yaw angle

A.2. Rotations of the ship

Figure A.4 indicates the locations of the accelerometers on the ship. The port side and starboard side accelerometers located near the stern of the ship measures only vertical accelerations. The one along the centerline near the stern measures only the acceleration in the y-direction, whereas the accelerometer near the bow measures the accelerations in all the three directions.

The vertical displacements measured by the accelerometers located at the bow and stern of the ship along the centerline were used to calculate the pitch angles $\theta(t)$ (Figure A.5). The pitch angle is positive when the displacement at the stern is positive.

$$\theta(t) = \arcsin\left(\frac{Z_s}{L}\right) \times \frac{180}{\pi} \tag{A.4}$$

With

Z_s the vertical displacement at the bow

L = distance between O' and the bow accelerator = 32.55 m

With respect to Figure A.6, The yaw angle $\psi(t)$ is calculated by using the following equation:

$$\psi(t) = 2 \times \arcsin\left(\frac{\left|\sqrt{X_b{}^2 + Y_b{}^2}\right|}{2L}\right) \times \frac{180}{\pi} \tag{A.5}$$

With X_b and Y_b respectively the displacements in x and y direction at the bow.

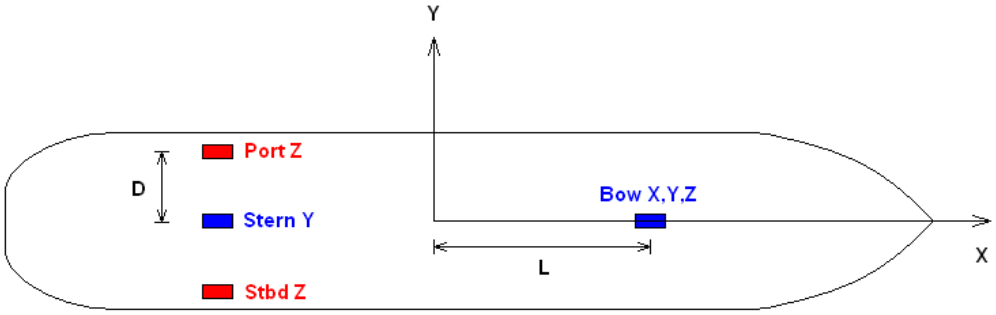

Figure A.4. Position of the accelerometers on the ship

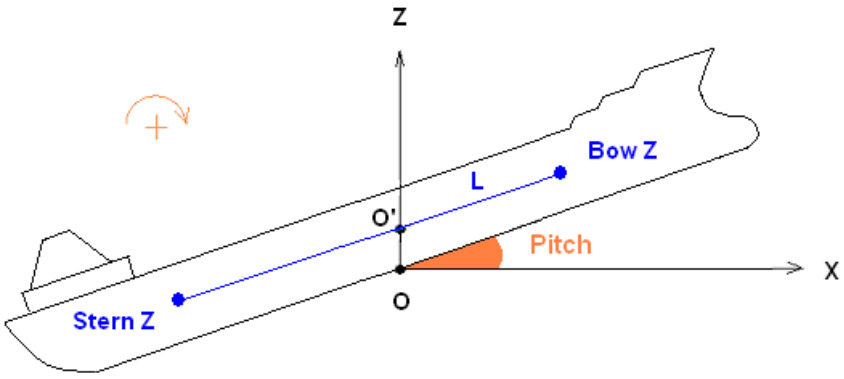

Figure A.5. Pitch angle

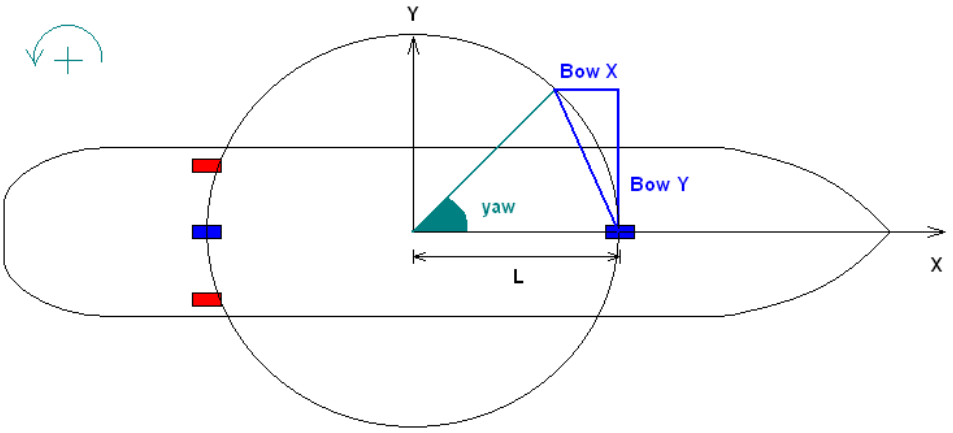

Figure A.6. Yaw angle

APPENDIX B. VALIDATION OF MATLAB PROGRAM

The Matlab program written for the system identification calculation consists of five consecutive functions.

```
%%%%%%%%%%%%%%%%%%%%%%%%%%%%%%%%%%%%%%%%%%%%%%%%%%%%

function [data_0mean, M] = zero_mean (data)

% Step 1. Calculate the 0 mean data to prepare for the spectral density
computation.

% data = matrix consists of the n inputs and the 1 output (n+1 columns)
% data_0mean = zero mean input and output vectors
% M = number of inputs + output

mat_dim = size(data);
N = mat_dim(1);                    % length of each vector
M = mat_dim(2);                    % number of inputs + output

for i = 1:M
    data_0mean (:, i)= data(:, i) - mean(data(:,i));
end



%%%%%%%%%%%%%%%%%%%%%%%%%%%%%%%%%%%%%%%%%%%%%%%%%%%%

function [S_uc, f] = uncondition_S (data_0mean, M, nfft, noverlap,
nwin, Fs)

% Step 2. Calculate the initial (unconditionned) spectral densities.

% nfft = number of FFT
% noverlap = number of overlapping
% nwin = window
% Fs = sampling frequency = 1/time lag
% S_uc = unconditionned spectral densities

% S(i,j,f,k) = auto- and cross-spectral densities, with i,j = 1, ... M
% f = 0, ... Fs/2,  frequency vector
% k = degree of conditioning (k = 1 means original spectral densities,
% k = 2 means that the influence of input #1 is removed, etc.)
```

```
for i = 1:M
    for j = 1:M
        [S_uc(i,j,:,1), f] = cpsd(data_0mean(:,i), data_0mean(:,j),
nwin, noverlap, nfft, Fs);
    end;
end;



%%%%%%%%%%%%%%%%%%%%%%%%%%%%%%%%%%%%%%%%%%%%%%%%%%%%

function [S, L] = condition_SL (S_uc, M, f)

% Step 3. Calculate the conditioned (uncorrelated) spectral densities
and the conditioned transfer functions.

% S = conditionned spectral densities
% L = conditionned transfer functions

S = zeros(M,M,length(f),M-1);

for i = 1:M
    for j = 1:M
        S(i,j,:,1) = S_uc(i,j,:,1);
    end
end

for k = 1:M-1
    for i = k+1:M
        for j = k+1:M

            L(k,j,:) = S(k,j,:,k)./S(k,k,:,k);

            if i == j
                S(i,j,:,k+1) = S(i,j,:,k) -
(abs(L(k,j,:)).^2).*S(k,k,:,k);
            else
                S(i,j,:,k+1) = S(i,j,:,k) - L(k,j,:).*S(i,k,:,k);
            end

        end
    end
end
```

```
%%%%%%%%%%%%%%%%%%%%%%%%%%%%%%%%%%%%%%%%%%%%%%%%%%%%%%%%

function [A] = original_A (M, L, f)

% Step 4. Calculate the original transfer functions A

% A = the original transfer functions

H(M-1,M,:) = L(M-1,M,:);

for i = M-2 : -1 : 1
    A = zeros(1,1,length(f));
    for j = i+1 : M-1
        A = A + L(i,j,:).*H(j,M,:);
    end
    H(i,M,:) = L(i,M,:) - A;
end


%%%%%%%%%%%%%%%%%%%%%%%%%%%%%%%%%%%%%%%%%%%%%%%%%%%%%%%%


function [OCF, CCF, Noise] = goodness (S, M, f, le)

% Step 5. Calculate the goodness of fit of the model.

% OCF = ordinary coherence function
% CCF = cumulative coherence function
% Noise = extraneous noise

% le = length(f)

for i = 1:M-1
    OCF(i,M,:) = abs(S(i,M,:,i)).^2./(S(i,i,:,i).*S(M,M,:,1));
    if i==1
        CCF(1,M,:) = OCF(1,M,:);
    else
        CCF(i,M,:) = CCF(i-1,M,:) + OCF(i,M,:);
    end
end

Noise = (1-CCF_final).* S(M,M,:,1);
```

This program was validated by being applied to the case study of a single degree of freedom (SDOF) linear system published by Bendat (1990). The differential equation is as followed:

$$m\ddot{u} + c\dot{u} + ku = F \tag{B.1}$$

With

m = mass = 1.0

c = linear damping coefficient = 3.77

k = linear stiffness coefficient = 355.3

The dynamic response displacement output data $u(t)$ was a randomly generated Gaussian distributed time series. The corresponding excitation forces $F(t)$ were obtained using the given values of system parameters and is low-pass filtered with a sharp cutoff at 10 Hz.

In the case study, Bendat estimated the magnitude as well as the phase of the reverse dynamic frequency response function of the system. Figures B1 and B2 compare these published results with the simulated result using the Matlab program developed for the current research work. The similarity between the published and the simulated results validate the Matlab program. Note that the dip observed in the magnitude plot occurs near the resonance frequency:

$$f_n = \frac{1}{2\pi}\sqrt{\frac{k}{m}} = 3.0\ Hz \tag{B.2}$$

(a)

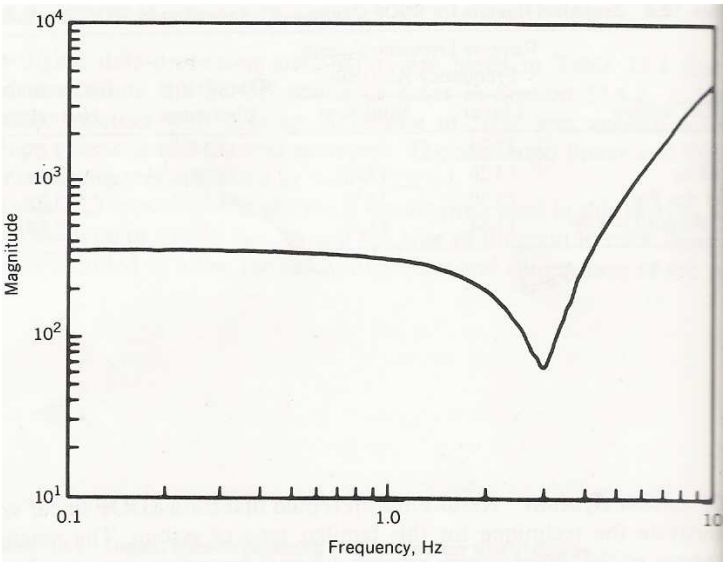

(b)

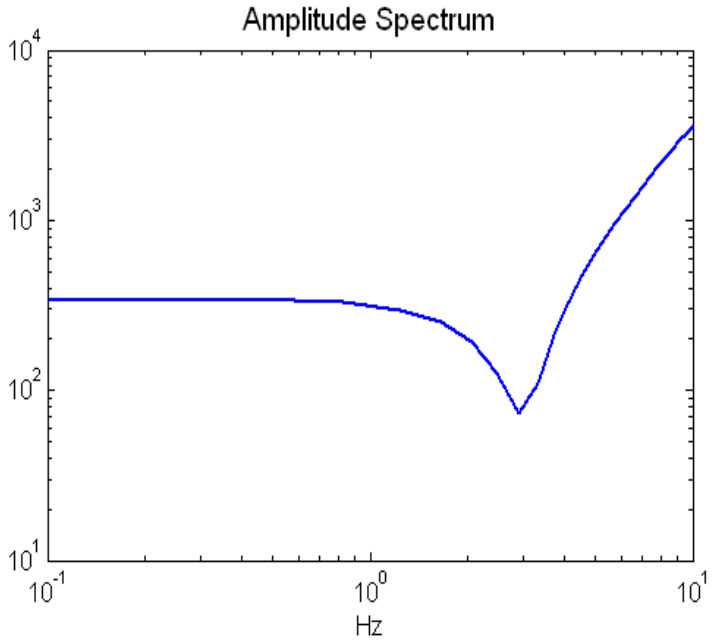

Figure B1. Comparison between (a) the published response function magnitude (Bendat, 1990) and (b) the simulated response function magnitude.

(a)

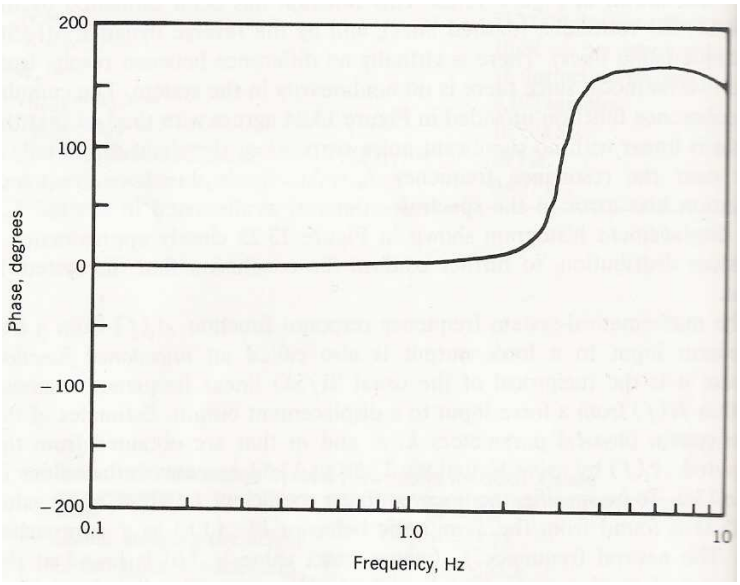

(b)

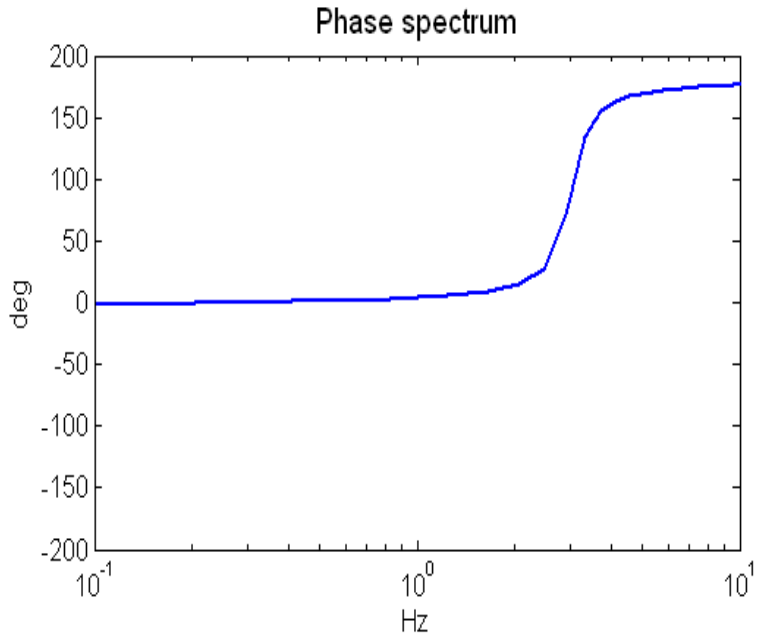

Figure B2. Comparison between (a) the published response function phase (Bendat, 1990) and (b) the simulated response function phase.

APPENDIX C. COMPUTATION OF LINEAR STIFFNESS COEFFICIENTS

In this section, the constant linear stiffness coefficients are estimated for both barge and ship to solve the problem of partitioning the identified results.

In section 3.2 and 3.3 it was stated that the general equation of motion of a floating body is:

$$(M+a)\ddot{x}(t)+c\dot{x}(t)+kx(t)+dD(t)+rR(t)=y(t) \tag{C.1}$$

With the mathematical inputs in the R-MISO method being the motion time series $x(t)$, the nonlinear hydrodynamic damping force term $D(t)$ and the nonlinear restoring force term $R(t)$. The mathematical output is the excitation force $y(t)$. And $(M+a)$, c, k, d, and r are the parameters to be identified.

The Fourier transform of Equation C.1 relates each of the inputs to the output.

$$A_1(f)X_1(f)+A_2(f)X_2(f)+A_3(f)X_3(f)=Y(f) \tag{C.2}$$

With A_i being the transfer functions:

$$A_1(f)=k(f)+j(2\pi f)c(f)-(2\pi f)^2(M+a)(f) \tag{C.3}$$

$$A_2(f)=d(f) \tag{C.4}$$

$$A_3(f)=r(f) \tag{C.5}$$

When the transfer functions are identified, no ambiguity exists as to the values of the nonlinear damping coefficient d and the nonlinear stiffness coefficient r, as well as that of the linear damping coefficient c. However, the linear stiffness coefficient k and the virtual mass $(M+a)$, being both included in the real part of the same transfer function A_1 as shown in Equation C.3, can not be distinguished without any additional information.

An initial attempt was made to use an additional input which is the time series of the motion acceleration. This manipulation would divide the transfer function in Equation C.3 into two transfer functions, each containing only one parameter in their real part. However, this method encountered a major obstacle due to the high correlation between the motion input data and the additional motion acceleration input data. R-MISO method does not work well when the two inputs data are too correlated because the conditioning procedure will leave one input data virtually useless.

Instead of processing the input data to reduce the correlation between them as suggested by Liagre (2002), it was decided to estimate the linear stiffness coefficients of the vessels based on their geometrical shape.

C.1. Linear stiffness coefficient of the barge

The barge is a $60\text{m}\times160\text{m}$ rectangular as indicated in Figure C.1. The calculation of the linear stiffness is much simplified due to its symmetrical shape. The only non-zero coefficient for the barge is the one related to the pitch motion. By definition (Faltinsen, 1990):

$$k_{55} = \rho g V\left(z_B - z_G\right) + \rho g \iint_{A_{WP}} x^2 ds \tag{C.6}$$

With

A_{WP} = waterplane area

V = displaced volume of water

z_B = z-coordinate of the center of buoyancy

z_G = z-coordinate of the center of gravity

ρ = density of seawater

The center of buoyancy is simply the center of the displaced volume, whereas the center of gravity is approximated at 10m from the keel based on available information. The moment of inertia about y-axis $\iint_{A_{WP}} x^2 ds$ for a rectangular can be easily calculated using the well-known equation:

$$I_y = \iint_{A_{WP}} x^2 ds = \frac{b^3 h}{12} \tag{C.7}$$

With b = 160m and h =60m.

Based on these values, the linear stiffness k_{55} of the barge was estimated to be 202700 MN.m. It is observed that the second term at the right-hand side of the Equation C.6, which contains $\iint_{A_{WP}} x^2 ds$, is significantly dominant due to the large waterplane area of the barge. Thus the calculated k_{55} remains quite accurate despite the use of an approximate value for the center of gravity.

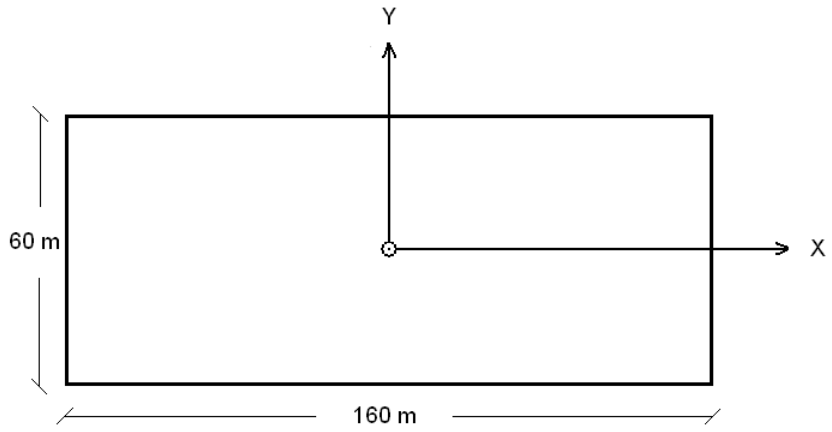

Figure C.1 Waterplane of the barge

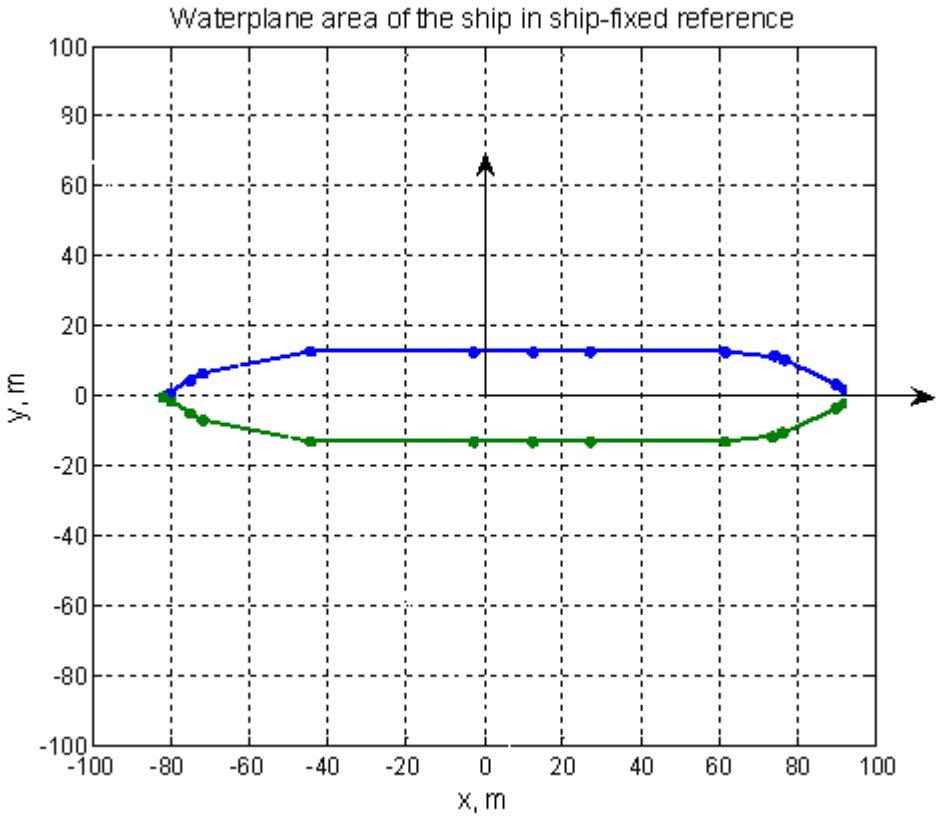

Figure C.2 Waterplane of the ship based on ship survey data

C.2. Linear stiffness of the ship

All the 6 degrees of freedom of the moored ship are to be considered. With the x-z plane as a symmetry plane for the submerged volume, the non-zero coefficients for the ship are by definition (Faltinsen, 1990):

$$k_{33} = \rho g A_{WP} \tag{C.8}$$

$$k_{35} = k_{53} = -\rho g \iint_{A_{WP}} x ds \tag{C.9}$$

$$k_{44} = \rho g V \left(z_B - z_G \right) + \rho g \iint_{A_{WP}} y^2 ds \tag{C.10}$$

$$k_{55} = \rho g V \left(z_B - z_G \right) + \rho g \iint_{A_{WP}} x^2 ds \tag{C.11}$$

The shape of the waterplane area of the ship was estimated from the available ship survey data. The draft of the ship in the 80% filled case is 8.26m, in order to have enough survey points to plot the waterplane all survey points having a z-axis value between 8m and 8.5m were used. Figure C.2 is the plot showing the waterplane area, symmetrical along the longitudinal, in the ship-fixed reference system based on a total of 26 survey points. Based on these survey results, the waterplane area A_{WP} is estimated to be 3857 m^2.

The moment of inertia about y-axis is by definition:

$$I_y = \iint_{A_{WP}} x^2 ds = \int_{-87.1}^{87.1} x^2 \left(y_1 - y_2 \right) dx = 2 \int_{-87.1}^{87.1} x^2 y_1 dx \tag{C.12}$$

The equations $y(x)$ can be approximated by dividing the waterplane area into five linear sections along the x-axis as shown in Figure C.3. The plot is not proportional for reason of visual clarity. The equations of each section are as followed, with $y_1(x)$ describing the portion of the perimeter having positive y and $y_2(x)$ the symmetrical part with negative y:

Section 1: $y_1(x) = 0.677(x + 87.1)$ $\quad y_2(x) = -0.677(x + 87.1)$ (C.13)

Section 2: $y_1(x) = 6.7 + 0.223(x + 77.2)$ $\quad y_2(x) = -6.7 - 0.223(x + 77.2)$ (C.14)

Section 3: $y_1(x) = 12.9$ $\quad y_2(x) = -12.9$ (C.15)

Section 4: $y_1(x) = 12.9 - 0.155(x - 56.4)$ $\quad y_2(x) = -12.9 + 0.155(x - 56.4)$ (C.16)

Section 5: $y_1(x) = 10.6 - 0.667(x - 71.2)$ $\quad y_2(x) = -10.6 + 0.667(x - 71.2)$ (C.17)

With these equations, I_y is approximated to be 7527070 m^4.

Similarly, the moment of inertia about x-axis is by definition:

$$I_x = \iint_{A_{WP}} y^2 ds = \int_{-12.9}^{12.9} y^2 (x_1 - x_2)\, dy \tag{C.18}$$

It can be obtained by dividing the waterplane area into linear sections along the y-axis as shown in Figure C.4. However, six sections are needed because the ship does not have a fore and aft symmetry.

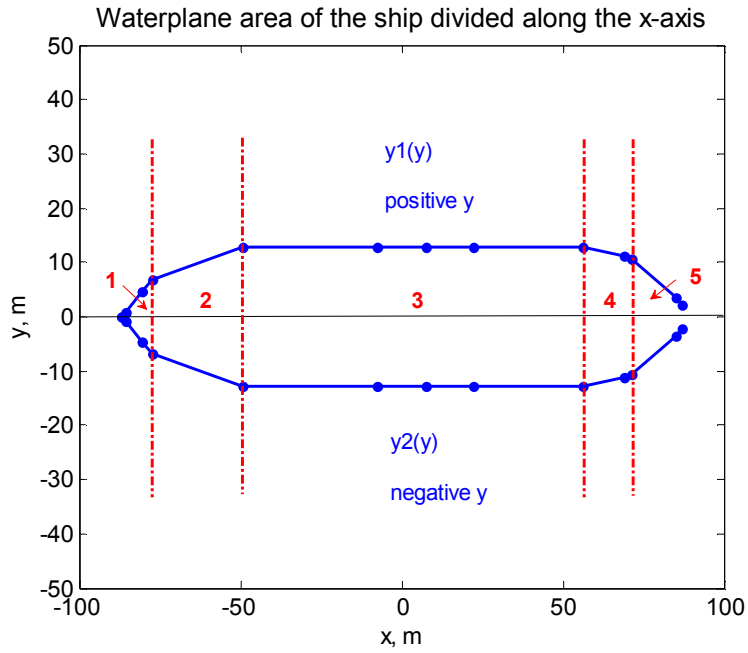

Figure C.3 Division of the waterplane for the calculation of the moment of inertia I_y

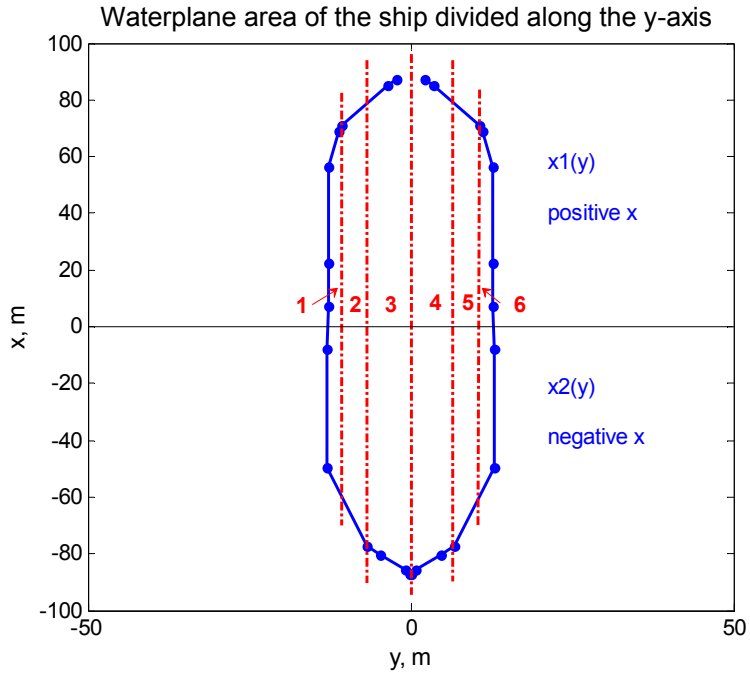

Figure C.4 Division of the waterplane for the calculation of the moment of inertia I_x

The equations of each section are as followed, with $x_1(y)$ describing the portion of the perimeter having positive y and $x_2(y)$ the symmetrical part with negative y:

Section 1: $x_1(y) = -49.4 - 4.484(y + 12.9)$ $\quad x_2(y) = 56.4 + 6.435(y + 12.9)$ (C.19)

Section 2: $x_1(y) = -49.4 - 4.484(y + 12.9)$ $\quad x_2(y) = 71.2 + 1.5(y + 10.6)$ (C.20)

Section 3: $x_1(y) = -77.2 - 1.478(y + 6.7)$ $\quad x_2(y) = 71.2 + 1.5(y + 10.6)$ (C.21)

Section 4: $x_1(y) = -87.1 + 1.478y$ $\quad x_2 = 87.1 - 1.5y$ (C.22)

Section 5: $x_1(y) = -77.2 + 4.484(y - 6.7)$ $\quad x_2 = 87.1 - 1.5y$ (C.23)

Section 6: $x_1(y) = -77.2 + 4.484(y - 6.7)$ $\quad x_2(y) = 71.2 - 6.435(y - 10.6)$ (C.24)

With these equations, I_x is approximated to be 190410 m^4.

From the available information, the center of buyancy of the 80% filled ship is about 4.7m and the center of gravity is about 7m above the keel. The displacement is about 31000 m^3.

Insert these calculated values into Equations C.8 – C.11, the linear stiffness coefficients of the ship can be computed:

$$k_{33} = \rho g A_{WP} = 38858774 \text{ N/m} \approx 38.9 \text{ MN/m} \quad \text{(C.25)}$$

$$k_{35} = k_{53} = -\rho g \iint_{A_{WP}} x ds = 55603208\text{N} \approx 55.6\text{MN} \tag{C.26}$$

$$k_{44} = \rho g V \left(z_B - z_G\right) + \rho g \iint_{A_{WP}} y^2 ds = 2636694228\ \text{N.m} \approx 2637\ \text{MN.m} \tag{C.27}$$

$$k_{55} = \rho g V \left(z_B - z_G\right) + \rho g \iint_{A_{WP}} x^2 ds = 76552589962\ \text{N.m} \approx 76553\ \text{MN.m} \tag{C.28}$$

Similar to the case of the barge, the parts containing moments of inertia in Equations C.21 and C.22 are more dominant compared to the parts containing the $\left(z_B - z_G\right)$, showing that the approximate estimation of the center of gravity and center of buoyancy does not have a large impact on the final result of the linear stiffness coefficient.

APPENDIX D. FORCE DECOMPOSITION

The use of the R-MISO method requires the knowledge of the total force decomposed into six degrees of freedom. In the coupled barge and ship configuration, the equation of motion should include the mooring line force and the fender force exerted on the vessels. However, the experimental data only provides values of inline mooring line and fender forces. To decompose them into the forces and moments corresponding to the six degrees of freedom, it is essential to know the relative position of the two vessels thus the inclination of the mooring lines and fenders.

Both the barge-fixed and ship-fixed reference systems used during the data measuring is centered at the vessel's keel / center / midship as a result of the different draft levels considered. In the current study, only the 80% filled ship case is concerned because this is the only configuration that enough information is available for an R-MISO analysis. In this configuration, the draft of the barge is 15m and that of the ship is 8.26m.

The position of the attach points of the mooring lines and fenders in both x-z and x-y planes are indicated in Figures D.1 and D.2 for respectively the barge and the ship. The four points on the barge are the attach points for the four mooring lines and the two points on the ship corresponds each to the attach point of a pair of mooring lines and a rigid fender at fore and aft locations (see Figure 2.1). Note that since the fenders were modeled as rigid rods fixed on the ship having roller contact with the barge, there is no fender attach points on the barge. However, the inclination of the rigid rods can be calculated without problem when the attach points on the ship are known.

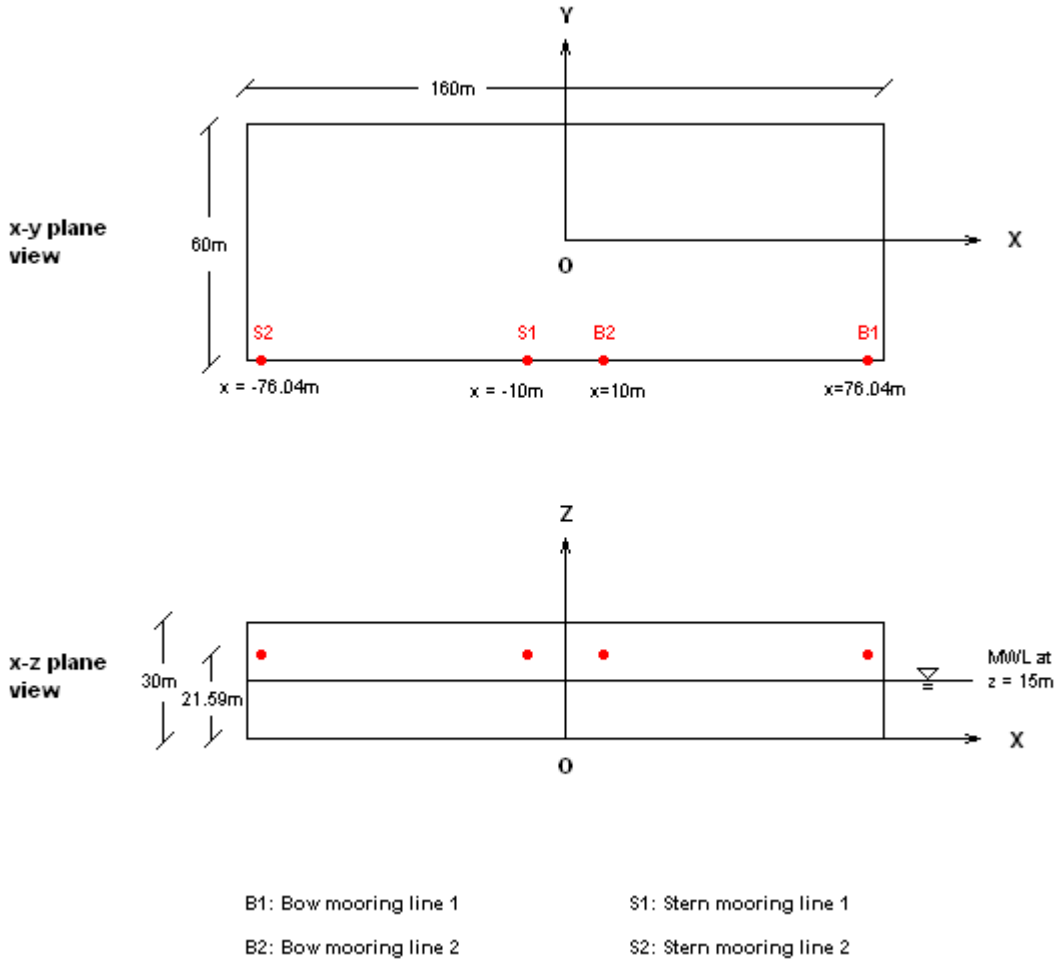

Figure D.1 x-y plane and x-z plane views of the mooring line attach points on the barge.

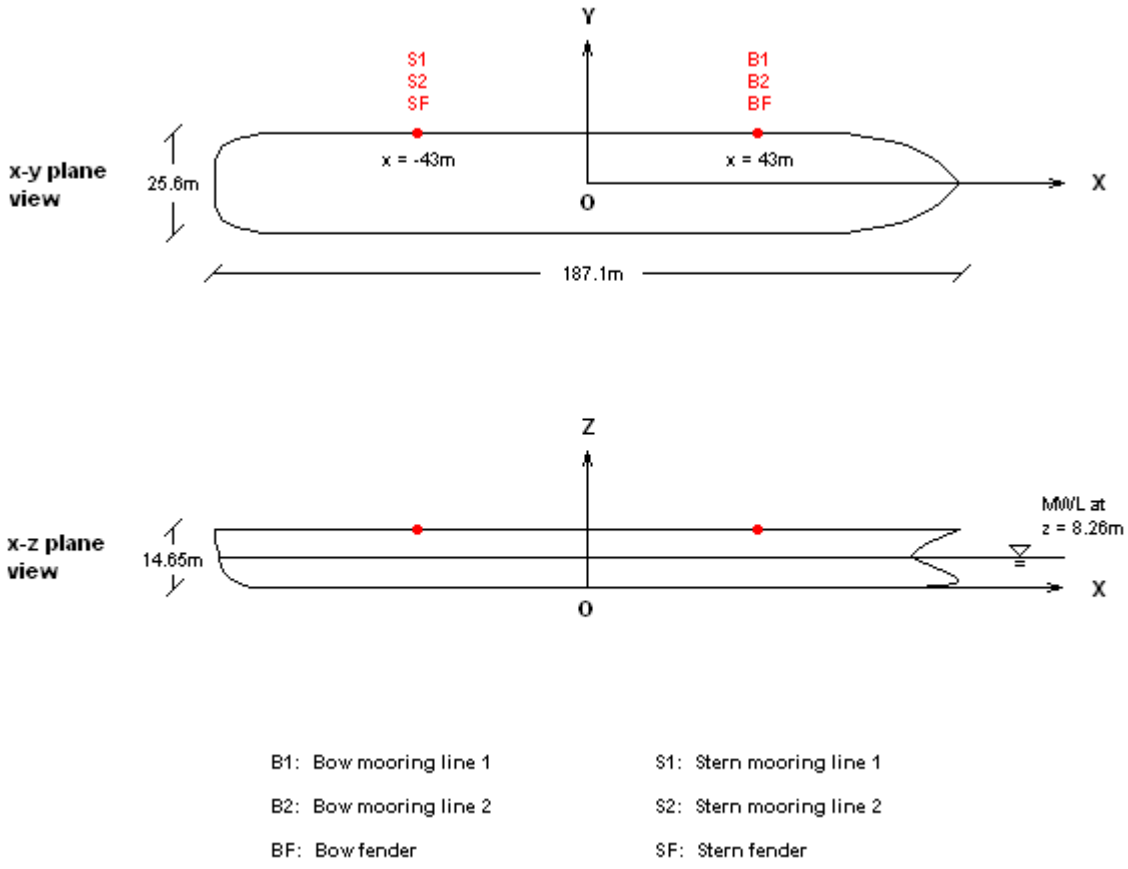

Figure D.2 x-y plane and x-z plane views of the mooring line and fender attach points on the ship.

As explained in Section 2, the surge, sway, heave motions of the barge can be neglected because the barge is fixed at its center. Table D.1 is a reproduction of Table 2.2 showing the standard deviations of the rotations of two vessels in the 80% filled configuration. Compared to the rotation motions of the ship, it can be concluded that only the pitch motion of the barge is large enough to be kept for the calculation of the relative position of the two vessels.

The time series of the barge roll as well as those of the 6 DOF motions of the ship are known. Using trigonometry, it is possible to calculate the position of the mooring line and fender attach points at every moment. These positions give the inclinations of the mooring line and fender rod that are needed for the decomposition of the inline forces and moments.

D.1 Final position of the attach points in the initial barge-fixed reference system

The only motion involved is the barge pitch motion $\theta(t)$ and the center of the barge-fixed reference system is keel / center / midship. Figure D.3 shows the initial position of a pair of attach points M_0 and N_0 equal-distant from the z-axis. They can be either the pair of bow mooring line 1 (B1) and stern mooring line 2 (S2) or the pair of bow mooring line 2 (B2) and stern mooring line 1 (S1), the calculation procedure is the same.

Let

$$\alpha = \arctan\left|\frac{x_{M_0}}{z_{M_0}}\right| \tag{D.1}$$

$$\beta = \arctan\left|\frac{z_{N_0}}{x_{N_0}}\right| \tag{D.2}$$

	80%, 0°	80%, -45°	80%, 45°
Barge roll	0.005	0.01	0.01
Ship roll	0.47	0.39	1.11
Barge pitch	0.10	0.18	0.09
Ship pitch	0.36	0.48	0.86
Barge yaw	0.03	0.05	0.04
Ship yaw	0.21	0.18	0.31

Table D.1 Comparison between the standard deviations of the barge and ship rotation motions (unit: degree)

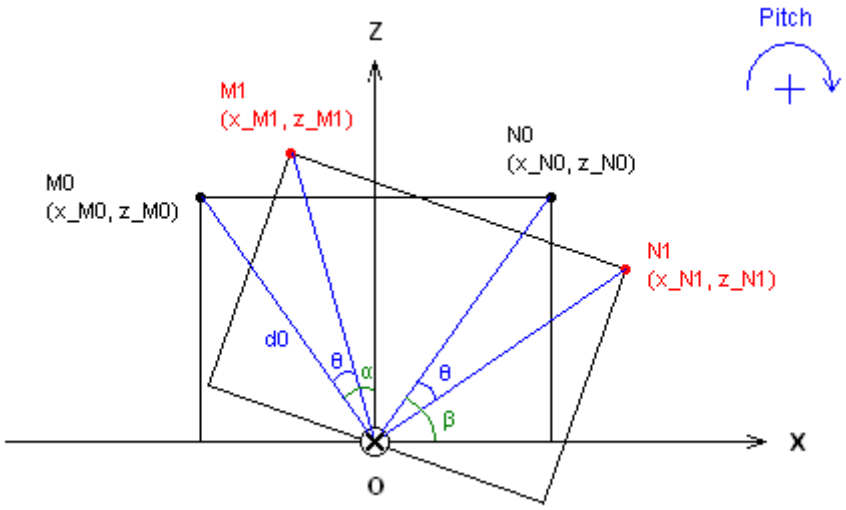

Figure D.3 Position of the attach point on barge before and after pitch rotation. View looking into the starboard side of the ship.

$$d_0 = \sqrt{x_{M_0}^2 + z_{M_0}^2} \tag{D.2}$$

Then the x and z coordinates of the attach point M after the pitch rotation are:

$$x_{M_1} = \text{sign}\left(x_{M_0}\right) d_0 \sin\left|\alpha - \theta\right| \tag{D.3}$$

$$z_{M_1} = \text{sign}\left(z_{M_0}\right) d_0 \cos\left|\alpha - \theta\right| \tag{D.4}$$

These equations work regardless the sign of the pitch motion. The sign of the coordinates does not change because the rotation is small. Note that $\sin\left|\alpha - \theta\right|$ and $\cos\left|\alpha - \theta\right|$ are always positive because $0 < \left|\alpha - \theta\right| < \frac{\pi}{2}$.

Similarly, the x and z coordinates of the attach point N after the pitch rotation are:

$$x_{N_1} = \text{sign}\left(x_{N_0}\right) d_0 \cos\left|\beta - \theta\right| \tag{D.5}$$

$$z_{N_1} = \text{sign}\left(z_{N_0}\right) d_0 \sin\left|\beta - \theta\right| \tag{D.6}$$

The y coordinates remain the same because the pitch rotation does not change these values.

D.2 Final position of the attach points in the initial ship-fixed reference system

In the case of the ship, one needs to take into account the motions in all the six degrees of freedom. The surge, sway and heave motions were measured with respect to the initial ship-fixed reference, thus these values can be added directly to the initial x, y and z coordinates of the attach points. To have a consistent notation with the barge case, let these new coordinates after the translations be x_0, y_0 and z_0.

The Equations D.3 – D.6 are valid for the ship pitch motion, they give x_1, y_1 and z_1 which are the coordinates of the attach points after the pitch motion. These values are used in turn as departure values for the calculation of positions after the roll motion $\phi(t)$. Figure D.4 show the positions of the attach points after the pitch rotation (M_1 and N_1) and those after both the pitch and roll rotations (M_2 and N_2). On this figure, the origin of the reference system becomes higher than the keel at the ship bow due to a positive pitch motion (for illustration purpose), the opposite occurs if the pitch is negative. M_2 and N_2 are in the same quadrant of the y-z plane, their equations will be the same. Only M_1 and M_2 were shown in Figure D.4 for the illustration of the method.

Let

$$\gamma = \arctan\left|\frac{y_{M_1}}{z_{M_1}}\right| \tag{D.7}$$

$$d_1 = \sqrt{y_{M_1}^2 + z_{M_1}^2} \tag{D.8}$$

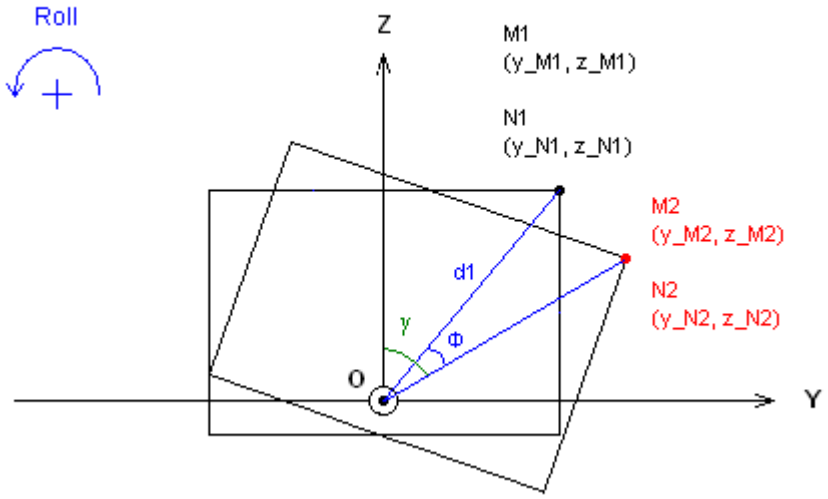

Figure D.4 Position of the attach point on ship before and after roll rotation, in addition to pitch motion. View looking into the bow of the ship.

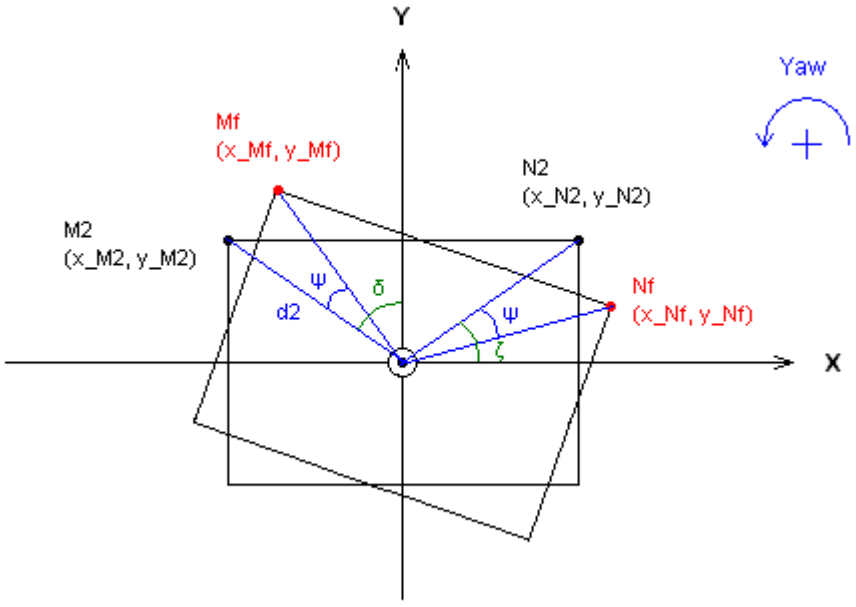

Figure D.5 Position of the attach point on ship before and after yaw rotation, in addition to pitch and roll motions. View from the top of the ship.

Then the y and z coordinates of the attach point M after the pitch and roll rotations are:

$$y_{M_2} = \text{sign}\left(y_{M_1}\right) d_1 \sin\left|\gamma - \phi\right| \tag{D.9}$$

$$z_{M_2} = \text{sign}\left(z_{M_1}\right) d_1 \cos\left|\gamma - \phi\right| \tag{D.10}$$

The y and z coordinates of the attach point N after the pitch and roll rotations are:

$$y_{N_2} = \text{sign}\left(y_{N_1}\right) d_1 \sin\left|\gamma - \phi\right| \tag{D.11}$$

$$z_{N_2} = \text{sign}\left(z_{N_1}\right) d_1 \cos\left|\gamma - \phi\right| \tag{D.12}$$

Again, these equations work regardless the sign of the pitch and roll motions. The x coordinates remain the same because the roll rotation does not change these values.

Finally, when the yaw motion $\psi(t)$ is taken into account, the previous positions M_2 and N_2 become the final positions M_f and N_f as shown in Figure D.5.

Let

$$\delta = \arctan\left|\frac{x_{M_2}}{y_{M_2}}\right| \tag{D.13}$$

$$\zeta = \arctan\left|\frac{y_{N_2}}{x_{N_2}}\right| \tag{D.14}$$

$$d_2 = \sqrt{x_{M_2}^2 + y_{M_2}^2} \tag{D.15}$$

Then the x and y coordinates of the attach point M after the pitch, roll and yaw rotations are:

$$x_{M_f} = \text{sign}\left(x_{M_2}\right) d_2 \sin\left|\delta - \psi\right| \tag{D.16}$$

$$y_{M_f} = \text{sign}\left(y_{M_2}\right) d_2 \cos\left|\delta - \psi\right| \tag{D.17}$$

Similarly, the x and y coordinates of the attach point N after the pitch, roll and yaw rotations are:

$$x_{N_f} = \text{sign}\left(x_{N_2}\right) d_2 \cos\left|\zeta - \psi\right| \tag{D.18}$$

$$y_{N_f} = \text{sign}\left(y_{N_2}\right) d_2 \sin\left|\zeta - \psi\right| \tag{D.19}$$

The z coordinates remain the same because the yaw rotation does not change these values.

Note that the above calculation is valid assuming the order in which the rotations were calculated is not important considering that the rotations are small.

D.3 Relative position between the barge and the ship

In order to calculate the relative position, a common reference system needs to be used, for instance the initial barge-fixed reference system. In such reference, the attach points on the two vessels have the initial coordinates indicated in Figure D.6.

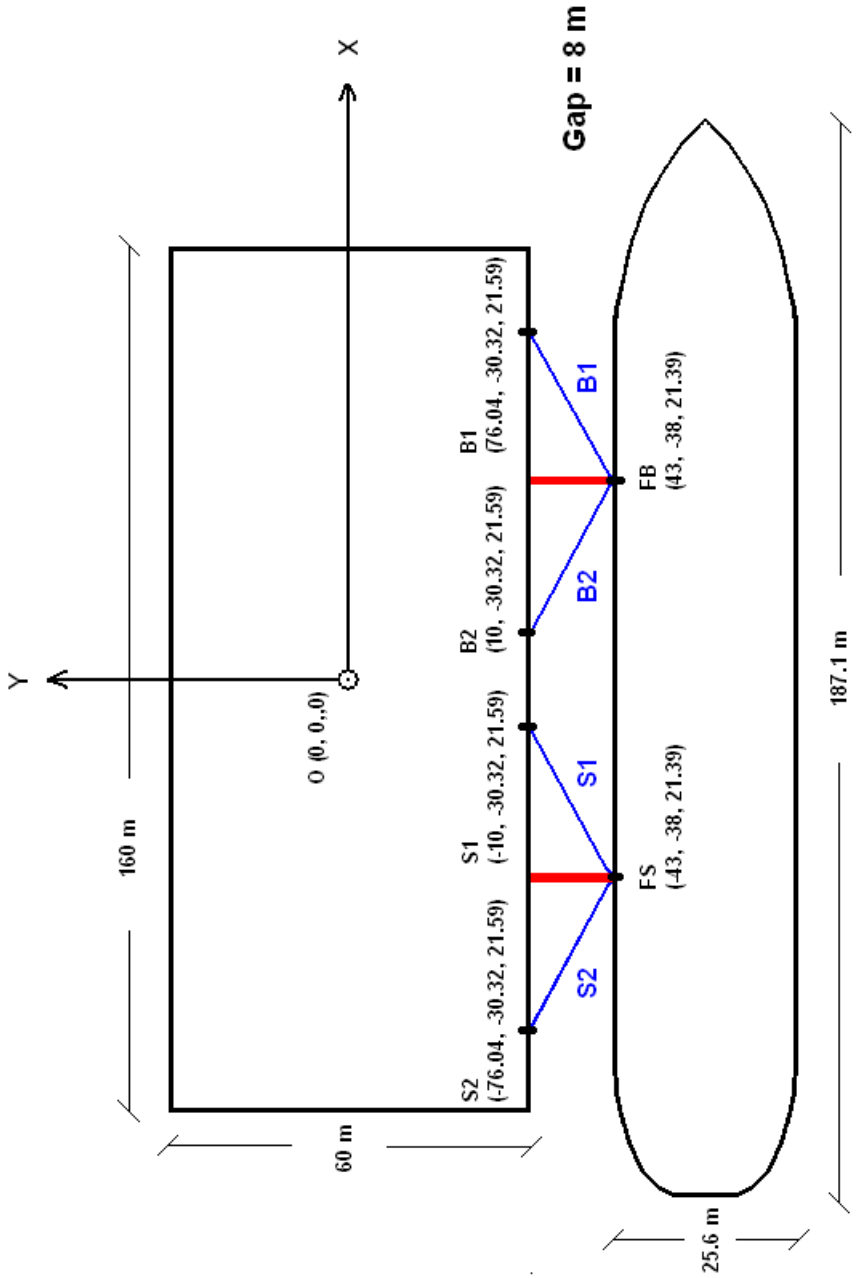

Figure D.6 Initial position of the attach points in the initial barge-fixed reference system.

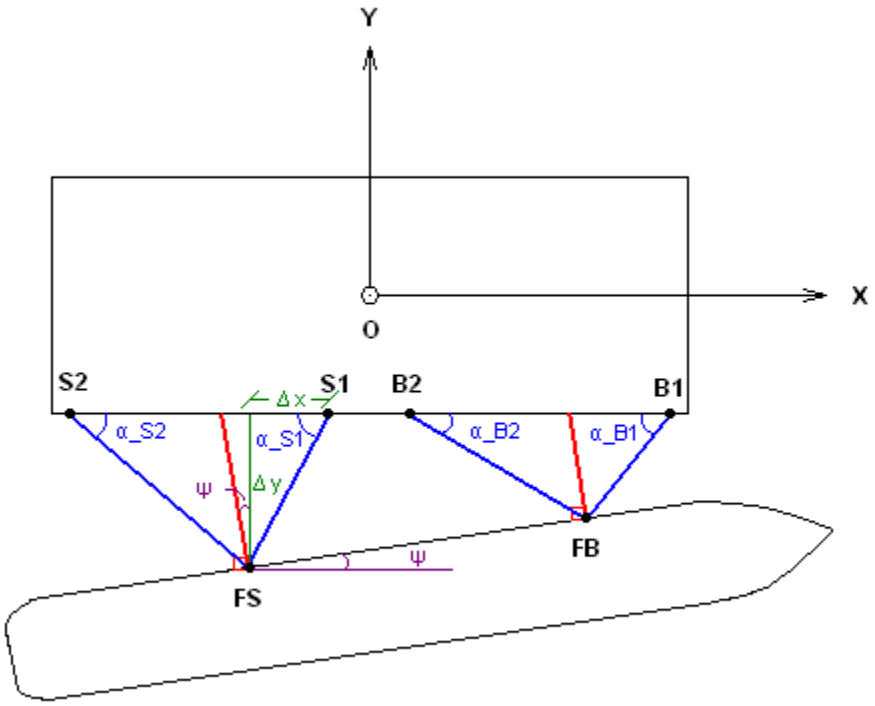

Figure D.7 Angles of decomposition in the x-y plane.

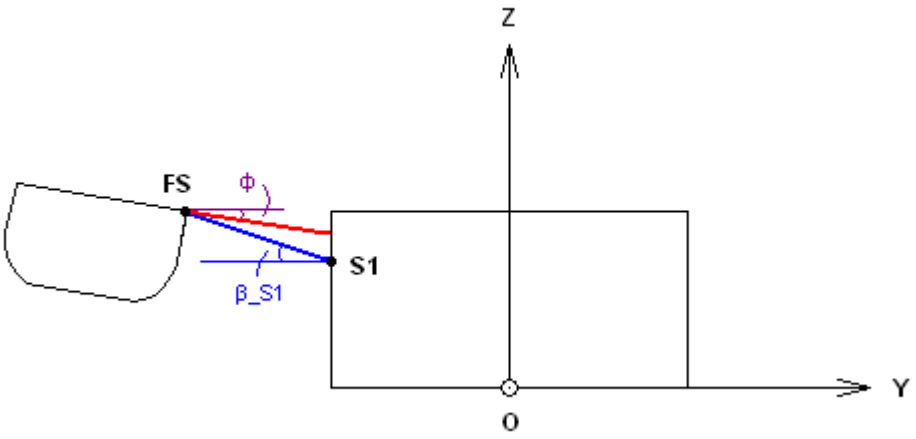

Figure D.8 Angles of decomposition in the y-z plane.

Figure D.7 shows the angles α_{S2}, α_{B2}, α_{S1} and α_{S2} needed for the decomposition of the inline mooring line forces in the x-y plane. Take the example of α_{S1}, it is calculated using the following formula:

$$\alpha_{S1} = \arctan\left|\frac{\Delta y}{\Delta x}\right| = \arctan\left|\frac{y_{FS} - y_{S1}}{x_{FS} - x_{S1}}\right| \tag{D.20}$$

Absolute values of the angles were used because the measured inline forces already have already taken into account the polarity (positive values for tensions and negative values for compressions).

Continuing the example of the stern mooring line #1, its forces in x and y directions are:

$$F_{S1\_x} = F_{S1}\cos\alpha_{S1} \tag{D.21}$$

$$F_{S1\_y} = F_{S1}\sin\alpha_{S1} \tag{D.22}$$

Note that $\cos\alpha_{S1}$ and $\sin\alpha_{S1}$ are always positive because $0 < \alpha_{S1} < \frac{\pi}{2}$.

The fenders were modeled as rigid rods fixed on the ship, in-line with the transversal axis of the ship. Since they do not have fixed contact points on the barge, the inclination of the fenders is calculated solely base on the motion of the ship. In the x-y plane, the yaw angle $\psi(t)$ of the ship is used for the force decomposition:

$$F_{FS\_x} = F_{FS}\left|\sin\psi\right| \tag{D.23}$$

$$F_{FS\_y} = F_{FS}\left|\cos\psi\right| \tag{D.24}$$

Figure D.8 shows the angle β necessary for the decomposition of the forces in y-z plane. Again take the example of the stern mooring line #1, the angle β_{S1} is calculated using the following formula:

$$\beta_{S1} = \arctan\left|\frac{\Delta z}{\Delta y}\right| = \arctan\left|\frac{z_{FS} - z_{S1}}{y_{FS} - y_{S1}}\right| \tag{D.25}$$

The mooring line force in the z-direction is:

$$F_{S1\_z} = F_{S1} \sin\beta_{S1} \tag{D.26}$$

The fender force is decomposed in the y-z plane using the ship roll angle $\phi(t)$:

$$F_{FS\_z} = F_{FS} \left|\sin\phi\right| \tag{D.27}$$

In the equation of motion used for the parameter identification of the two-body system (Equation 4.2), only resultant forces are needed for the mooring line force and fender force.

The resultant mooring line force in all the three axis is expressed as:

$$F_{l\_z} = F_{B1\_z} + F_{B2\_z} + F_{S1\_z} + F_{S2\_z} \tag{D.28}$$

$$F_{l\_y} = F_{B1\_y} + F_{B2\_y} + F_{S1\_y} + F_{S2\_y} \tag{D.29}$$

$$F_{l\_z} = F_{B1\_z} + F_{B2\_z} + F_{S1\_z} + F_{S2\_z} \tag{D.30}$$

The corresponding moments are calculated using Equation D.31:

$$\begin{pmatrix} M_x \\ M_y \\ M_z \end{pmatrix} = \begin{pmatrix} r_x \\ r_y \\ r_z \end{pmatrix} \times \begin{pmatrix} F_x \\ F_y \\ F_z \end{pmatrix} \tag{D.31}$$

That is:

$$M_x = r_y F_z - r_z F_y \tag{D.32}$$

$$M_y = r_z F_x - r_x F_z \tag{D.33}$$

$$M_z = r_x F_y - r_y F_x \tag{D.34}$$

With M being the moment of the resultant force, F the force vector and r the distance between the resultant force vector and the axis of rotation. In the case of the moments with respect to the barge axis for example, $r_x = 0\,\text{m}$, $r_y = -30.32\,\text{m}$, $r_z = 21.59\,\text{m}$.

VITA

Name	Chen Xie
Address	SOFEC, Inc 14741 Yorktown Plaza Drive Houston, TX77040 USA
Email Address	chen.xie@sofec.com
Education	Engineer Degree (French equivalent of B.S. and M.S. degrees), Building Engineering, Ecole Spéciale des Travaux Publics, 2004. M.S., Ocean Engineering, Texas A&M University, 2005. PhD, Ocean Engineering, TexasA&M University, 2009.